University of Alberta

Mechanical Response of Microspring Thin Films

by

Mary Wai Ming Seto

A thesis submitted to the Faculty of Graduate Studies and Research in partial fulfillment of the requirements for the degree of Doctor of Philosophy

Department of Electrical and Computer Engineering

Edmonton, Alberta, Canada

Fall 2004

Library and Archives Canada

Published Heritage Branch

395 Wellington Street
Ottawa ON K1A 0N4
Canada

Bibliothèque et Archives Canada

Direction du Patrimoine de l'édition

395, rue Wellington
Ottawa ON K1A 0N4
Canada

Your file Votre référence
ISBN: 0-612-96016-1
Our file Notre référence
ISBN: 0-612-96016-1

The author has granted a non-exclusive license allowing the Library and Archives Canada to reproduce, loan, distribute or sell copies of this thesis in microform, paper or electronic formats.

L'auteur a accordé une licence non exclusive permettant à la Bibliothèque et Archives Canada de reproduire, prêter, distribuer ou vendre des copies de cette thèse sous la forme de microfiche/film, de reproduction sur papier ou sur format électronique.

The author retains ownership of the copyright in this thesis. Neither the thesis nor substantial extracts from it may be printed or otherwise reproduced without the author's permission.

L'auteur conserve la propriété du droit d'auteur qui protège cette thèse. Ni la thèse ni des extraits substantiels de celle-ci ne doivent être imprimés ou aturement reproduits sans son autorisation.

In compliance with the Canadian Privacy Act some supporting forms may have been removed from this thesis.

Conformément à la loi canadienne sur la protection de la vie privée, quelques formulaires secondaires ont été enlevés de cette thèse.

While these forms may be included in the document page count, their removal does not represent any loss of content from the thesis.

Bien que ces formulaires aient inclus dans la pagination, il n'y aura aucun contenu manquant.

Canada

TABLE OF CONTENTS

Chapter 1 – Introduction and Scope of Thesis 1

1.1 Introduction 1

1.2 Scope 2

Chapter 2 – Thin Film Growth Mechanisms and the GLAD Technique 5

2.1 Historical Aspects of Porous Film Growth 5

2.2 Columnar Film Growth 6

2.2.1 Diffusion 6

2.3 Oblique Film Growth 8

2.3.1 Deposition Angle and Porosity 9

2.4 Glancing Angle Deposition 11

2.4.1 Effect of Substrate Motion 12

2.4.2 Advanced Control and Other Microstructures 13

2.4.3 Film Thickness Variation 14

2.5 Other GLAD Applications 16

2.5.1 Optical Applications 16

2.5.2 Sensing Applications 18

2.5.3 Periodic Structures 18

2.5.4 Thin Film Simulation 19

2.5.5 Summary 20

2.6 References 21

Chapter 3 – Fabrication of Films for Testing 25

3.1 Introduction 25

3.2 Physical Vapour Deposition Processes 25

3.2.1 Thermal and Electron Beam Evaporation 26

3.2.2 Sputtering 27

3.3 Fabrication of Microspring Thin Films 28

3.3.1 Microspring Geometries 30
3.3.2 Other Microspring Materials 31
3.3.3 Capped Microsprings 32
3.4 Fabrication of Inclined Microcantilevers 33
3.4.1 Ordered Arrays Versus Random Films 34
3.5 Growth of Piezoelectric Films: Dense and Porous 37
3.6 Other Characterization 39
3.6.1 Metallization Layers 39
3.6.2 X-Ray Diffraction and Transmission Electron Microscopy 40
3.6.3 Humidity Sensing 41
3.6.4 Substrate Temperature Considerations 42
3.7 References 49

Chapter 4 – Main Results: Mechanical Characterization of Microsprings and Microcantilevers 53
4.1 Introduction 53
4.2 Theoretical Springs 53
4.2.1 Spring Constants 53
4.2.2 Vibrational Frequencies 56
4.3 Cantilever Theory 57
4.4 Nanoindentation 57
4.4.1 Effect of Force Loading Curves 62
4.5 Nanoindentation of Standard Films and Substrates 62
4.6 Nanoindentation of Capped Films 63
4.6.1 Film Details 63
4.6.2 Nanoindentation Details 64
4.6.3 Force Displacement Results For Capped Film Nanoindentations 64
4.6.4 Effect of High and Low forces 66
4.6.5 Comparison Between Experimental and Theoretical Data 68
4.6.6 Discussion of Results 69
4.7 Nanoindentation of Uncapped Films 70
4.7.1 Experimental Details 70
4.7.2 Nanoindentation Tip Selection 70

4.7.3 Nanoindentation Results for Uncapped Microsprings 72
4.7.4 Effect of Different Materials 73
4.8 Nanoindentation of Microcantilever Arrays 75
4.8.1 Microcantilever Array Details 75
4.8.2 Comparison of Experimental and Theoretical Results 76
4.9 Finite Element Analysis 78
4.9.1 ANSYS Study 79
4.9.2 Recent ALGOR Results 80
4.10 References 82

Chapter 5 – Potential Resonator Application 87
5.1 Motivation 87
5.2 Estimated Resonant Frequencies 87
5.2.1 Axial Frequency Calculation 88
5.3 Testing Methods: Electrostatic Actuation 89
5.3.1 Fabrication of Optimal Microspring Geometries 91
5.3.2 Estimated Deflections 92
5.4 Hysitron Acoustic Emission Testing 95
5.5 Atomic Force Microscopy 95
5.6 Laser Excitation with Piezoelectric Detection 97
5.6.1 Laser Excitation with Interferometric Detection 99
5.7 Network Analyzer Investigations with Lateral Oscillations 99
5.8 References 103

Chapter 6 – Film Growth on Mesas: A Potential New Application 105
6.1 Introduction 105
6.2 Mesa and Line Fabrication 105
6.3 Experiment and Results for Slanted Post Film Growth 107
6.4 Experiment and Results for Helical Film Growth 110
6.4.1 Capping Layer Growth over Walled Structures 112
6.5 Discussion of Applications 113
6.6 References 113

Chapter 7 – Conclusions and Suggestions for Future Research 117

7.1 Conclusions: Mechanical Response of GLAD Films 117

7.1.1 Electrode Metallization Layer Development 117

7.1.2 Frequency Determination 118

7.1.3 Key Areas for Improvement 118

7.2 Suggestions for Future Research: Materials Optimization 118

7.2.1 Microstructure Parameter Optimization 119

7.2.2 Measurement Improvements of Parameters for Theoretical Predictions 119

7.2.3 Porosity Enhancement with Patterned Substrates 120

7.2.4 Future Prognosis 120

LIST OF TABLES

Table 3.1: Geometrical parameters of a set of microspring films tested. 30

Table 4.1: Comparison of experimental and theoretical results for helical and dense SiO films with capping layers taken from a spherical 100 μm radius of curvature tip. 68

Table 4.2: Comparison of experimental and theoretical areal stiffness values for various thin film samples. 74

Table 4.3: Geometrical parameters of the microcantilever array tested. 77

Table 4.4: Comparison of measured deflections from nanoindentation experiments of microsprings with ANSYS modeled microsprings (at right). 79

Table 4.5: Comparison of microspring stiffness values (N/m) from Ancker's equation, symmetric and non-symmetric BC's and experimental nanoindentation results. 80

Table 5.1: Calculations of estimated resonant frequencies for various microspring types. 88

Table 5.2: Estimated microspring deflections for electrostatically induced deflection in microsprings with the geometrical parameters as those listed in Table 3.1. 94

Table 5.3: Estimated lateral spring constants and frequencies. 100

LIST OF FIGURES

Figure 2.1: PVD deposition of a dense, columnar thin film. 7

Figure 2.2: Early stages of shadowing occurring from the arrival of oblique vapour flux at high deposition angles (α). 8

Figure 2.3: Schematic illustration showing the effects of limited adatom diffusion and enhanced shadowing. 9

Figure 2.4: Increasing film porosity with increasing deposition angle (α). The film shown at top right is a dense ZnO film grown at normal incidence, while the film below it is a SiO film grown at $\alpha = 85°$. 10

Figure 2.5: GLAD apparatus showing the flexible range of substrate movement. 11

Figure 2.6: Some basic GLAD microstructures such as ZrO_2 chevrons (a), SiO helices (b), and SiO_2 post structures (c). 13

Figure 2.7: Capping layer evolution due to reduction of angle α and increase in ϕ. 14

Figure 2.8: Schematic showing the minimal lateral spread of the substrate as seen by the source. 15

Figure 2.9: SEM images of a Ti film at the centre (a) and edge (b) of the substrate showing a slight thickness variation of ~205 nm (<10% of the total film thickness). 16

Figure 2.10: A tetragonal square spiral GLAD film (with side view inset) having potential applications as a photonic band gap material. 17

Figure 2.11: A periodic film of SiO posts deposited onto a photoresist array. 19

Figure 3.1: Schematic illustration of the growth of a 3-turn microspring. 28

Figure 3.2: Examples of uncapped SiO microspring films of similar thickness with the last film having an unsuitable auger-like shape. 29

Figure 3.3: Examples of uncapped SiO microspring films with the same pitch and varying numbers of turns. 31

Figure 3.4: Ti and Cr microsprings fabricated with electron beam evaporation. 32

Figure 3.5: Capped SiO microspring and microcantilever films. 33

Figure 3.6: Schematic illustration of the growth of slanted posts. 34

Figure 3.7: Periodicity in the film is imposed by the addition of a patterned layer having seed elements to control where columnar film growth begins. 35

Figure 3.8: Embossed polymeric array (a) with periodic Ni slanted films (b and c), a random SiO slanted post film on plain Si (d), and an array of SiO posts on patterned photoresist (e). 36

Figure 3.9: Sputtered ZnO films with a) dense microstructure, b) attempted "helical" microstructure, and c) pulsed laser deposited ZnO. 37

Figure 3.10: Porous helical $LiNbO_x$ (at left) and ZnS_x (at right) films. 39

Figure 3.11: An approximately 75 nm thick Al metallization layer showing a high degree of roughness in comparison to an Au layer of similar thickness. 39

Figure 3.12: Nodular growths in SiO films that were subsequently formed on the Al coated substrates. 40

Figure 3.13: Bright field TEM image (a) and diffraction pattern (b) of a Cr microspring from the film pictured in Figure 3.4. 41

Figure 3.14: A SiO film showing significant columnar broadening. 42

Figure 3.15: An RTD circuit employing a 4 wire configuration utilizing a current source to allow the voltage across the device to be measured and converted to temperature. 43

Figure 3.16: Temperature vs. time plot for an 85° deposition of SiO inside a thermal evaporation chamber. 44

Figure 3.17: For evaporated films, radiative heat transfer can be a cause of increased substrate temperatures. 46

Figure 3.18: Predicted Temperature-Time response for a substrate under a power flux of 10 mW/cm^2 and neglecting heat loss due to conduction. 48

Figure 4.1: Schematic diagram of a spring illustrating geometrical parameters. 54

Figure 4.2: Schematic illustration of a microspring thin film. 55

Figure 4.3: Axial compression for the spring at left and lateral bending for the spring at right. 56

Figure 4.4: Schematic diagram of a cantilever illustrating geometrical parameters. 57

Figure 4.5: Internal schematic of the Hysitron Trioboscope transducer. 58

Figure 4.6: Images of the Triboscope Nanoindenter and Atomic Force Microscope. 59

Figure 4.7: A typical force displacement curve for a spherical indenter. 59

Figure 4.8: Schematic illustration of a cono-spherical nanoindentation tip displacing a microspring film. 60

Figure 4.9: A SEM image of a cono-spherical nanoindenter tip with 1 micron radius of curvature. 61

Figure 4.10: Typical force loading curves with (a) load-hold-unload, (b) load-unload, (c), load-partial unload-load-partial unload-load-unload, and (d) load-hold-sinusoidal loading-unload sequences. 62

Figure 4.11: Nanoindentation curves of a glass slide in (a), a silicon substrate in (b). 63

Figure 4.12: Force versus displacement nanoindentation results for capped microspring films. For the SiO film pictured in (c), two loading curves (shown inset) were used to generate the displacement curves in (a) and (b). 65

Figure 4.13: Effects of indentations made with large forces. The displacement curve in (a) was generated from indentations made in the SiO film shown below in the two SEM pictures. High force indentations caused the capping layers to fracture twice as shown in (b), and an overlay of the nanoindenter tip in (c) shows the depth it penetrated into film when each of the fractures occurred. 67

Figure 4.14: SEM image of a SiO microspring film showing nodular defects. 71

Figure 4.15: Force versus displacement results showing: (a) the results of three low force indentations carried out successively at the same site for a 2-turn microspring (b) the trend in the curves for various microspring geometries. 72

Figure 4.16: Displacements comparisons for the Ni slanted post array. 76

Figure 4.17: Force-displacement curve of Ni microcantilever and plastic seed layer combination 77

Figure 5.1: Interferometric detection of an electrostatically actuated microspring film 90

Figure 5.2: A microspring film showing significant bifurcation in an attempt to increase the coil radius (a), and a film with smaller coil radius and less columnar broadening (b). Note the difference in scale bars between the two images. 91

Figure 5.3: Theoretical deflection for a 2 μm thick, 2-turn helical microspring ($\kappa = 4$) with varying columnar thickness (d) and varying coil radius (R). The optimal geometry for maximum deflection consists of small d and large R. 92

Figure 5.4: Top electrode pattern after masking the capping layer. 93

Figure 5.5: Schematic of AFM tip used to oscillate a single microspring. 96

Figure 5.6: Schematic of the knife edge technique. 97

Figure 5.7: Recorded waveform from a PVDF film positioned approximately 8-10 mm away from the point of a laser pulse excitation. The large initial spike seen at the left indicates the moment the laser was triggered, and the smaller sinusoid seen at the right is the recorded sound wave. 98

Figure 5.8: Displacement-time waves for plain Si in (a) and for a 4 turn microspring film on Si in (b) after laser excitation. 99

Figure 5.9: Schematic of the microsprings grown on the CTM crystals and the lateral mode of oscillation they produced. 101

Figure 5.10: A network analyzer plot showing the absorption characteristics (ratio of reflected to transmitted power) of the CTM crystal over a frequency span of 5 kHz. A clear peak is shown at the resonance of the CTM crystal (~5.9 MHz). 101

Figure 6.1: Scanning Electron Microscope (SEM) images of bare silicon mesas (2.5 × 2.5 μm in (a) and 7 × 7 μm faces in (b)) upon which subsequent films were grown. 106

Figure 6.2: Various sizes of bare silicon lines on silicon which were later deposited on to form channels that contained unique structures having sealed side walls and top faces. 107

Figure 6.3: Areal view of three arrays of mesas with GLAD-fabricated porous thin film grown on top (a). The thin film microstructures resembled slanted posts, and were grown by an oblique angle deposition, with the arrow indicating the direction of the vapour flux. One of the largest sized mesas is shown inset. A close up view of the second largest sized mesas is shown in (b). 108

Figure 6.4: Distinct shadowing is evident between the silicon mesas. Dense regions of film growth along the vertical Si sidewalls occurred for those facing the direction of arriving flux, while the top faces contained a porous film. 109

Figure 6.5: Schematic illustration of the perceived substrate and perceived incidence angles as seen by the vapour flux as it encountered the sides and top faces of the mesas. 110

Figure 6.6: The helically microstructured film deposition resulted in solid perimeters encircling each mesa. Surface debris is believed to have caused the irregularities seen on a few of the mesas. 111

Figure 6.7: Areal view of a microchamber showing the porous centre (with close up shown inset) contained by a solid border. 111

Figure 6.8: Capped microchambers completely enclosed by encapsulation walls along all side and top faces. 112

Figure 6.9: Cross sectional images of capped helical films grown on silicon lines to form enclosed microchannels. 113

LIST OF SYMBOLS AND ABBREVIATIONS

α	Vapour incidence angle (angle between the substrate normal and direction of incident flux
α	Pitch angle (the rise angle that a spring has with respect the ground plane)
AFM	Atomic force microscope
β	Columnar inclination angle
BC	Boundary conditions
BOE	Buffered oxide etch
c	Heat capacity
CTM	Crystal thickness monitor
d	Column diameter (the diameter of a column's cross-section)
D	Diffusion coefficient
δ	Seed separation (distance between the seed elements in a patterned array)
ΔH_c	Heat of condensation (of deposited atoms arriving at the substrate)
d_o	Molecular diameter
Δx	Deflection of a spring or cantilever
ε	Emissivity
E	Emitted energy flux
E	Young's Modulus
E_D	Activation energy for diffusion
E_k	Kinetic energy of evaporated atoms
E_r	Reduced Young's Modulus
ε_o	Permittivity constant
E_p	Plasma energy of sputtered atoms
f	Axial resonant frequency for a spring
ϕ	Azimuthal rotation of the substrate
F	Applied force
FEA	Finite element analysis
f_L	Lateral resonant frequency
G	Shear Modulus
h	Film thickness
I	Mass moment of inertia
i	Number of microstructures
ICP RIE	Inductively coupled plasma reactive ion etcher
k	Axial spring constant
k	Boltzmann constant

κ	dielectric constant
k_L	Lateral spring constant
λ	Mean free path
L	Radiant energy loss from the substrate
M	Bending moment
MEMS	Microelectromechanical systems
n	Number of turns in a spring
ν	Poisson's ratio
P	Incident power flux at the substrate
P	Load
p	Vacuum pressure inside a deposition chamber
PBG	Photonic band gap
PVDF	Polyvinylidene fluoride (a piezoelectric film)
R	Coil radius
ρ	Density
r	Deposition rate
R	Universal gas constant
RTD	Resistance temperature device
σ	Stefan-Boltzmann constant
S	Stiffness
SAW	Surface acoustic wave
SPM	Scanning probe microscopy
t	Seed thickness (the height of the seed element in a periodic array)
T/T_m	Ratio of substrate temperature to melting temperature of the source material
V	Voltage
Ω	Atomic volume for condensate at the substrate

ACKNOWLEDGEMENTS

During my years as a graduate student, I had the opportunity to work with a remarkable group of people who I would like to thank for a great experience.

Many thanks go first and foremost to my supervisor Michael Brett, whose influence and avid enthusiasm were key to inspiring my interest in this field. I am truly indebted to the exceptional learning experience that I received working under his knowledgeable guidance.

Thanks must go to the GLAD gang that I worked with – I really could not have asked for a better research group. To Kevin, Jeremy, Doug, Albert, Ken, Brian, Scott, Mike, Greg, Martin, Barb, Peter, Jim, James, Andy, Anastasia, Ben, and last but not least Karin: best wishes to you all and thanks for the memories.

I also wish to acknowledge Glen Fitzpatrick and the members of my examining committee, Drs. Dew, McMullin, Eadie, Johnston, and Filanovsky for their reading of my thesis and their valuable suggestions for improvements.

The extraordinary SEM images seen throughout this thesis are due to talent of George Braybrook, whose skill in capturing the perfect thin film images are extolled with much appreciation.

To my twin sister Margaret, thanks for all the chats, telephone calls, and visits, and for being such an upbeat and cheery spirit.

Thank you Mom and Dad for your love and support throughout these years, for inspiring me to strive for higher aspirations and to succeed in achieving them.

Most importantly, I would like to thank Keith for being immeasurably thoughtful, loving, and kindhearted. You always lent a kind ear when I needed it, encouraged me during the difficult days, and never failed to make me smile just when I needed it. Thank you for being there throughout it all.

CHAPTER 1
INTRODUCTION AND SCOPE OF DISSERTATION

1.1 Introduction

It would be difficult today to find an educated person who has never encountered the concept of thin films. They are the infinitesimal components of many current technologies, and will become the foundation of many more in the century to come. As blocks of marble were to the cathedrals of old, these films – often less than a micron thick – will serve as the building stones of new technologies, as their capabilities and functions improve. Already, thin films are essential in countless modern technologies, from optical coatings to the integrated circuits and displays of our computers and personal electronics, and their optimization drives continuing research. This enabling technology and its applications are therefore an important area of study, as they will grow increasingly attractive as the miniaturization trend continues into the 21st century. The immediate goal of such study is to fabricate thin films with properties that can be tuned to the needs at hand and those to come.

Microstructured thin films grown using the Glancing Angle Deposition (GLAD) technique may be able to offer solutions and keys to achieve many of these needs. These unique films offer broad possibilities for developments in diverse fields, encompassing the mechanical, optical, biological, chemical, electrical, and magnetic domains. Unlike conventional two-dimensional thin films, these extraordinary films can be envisioned as microscopic arrays of posts, helices and zigzags, and can be designed in a variety of other configurations as well. GLAD-fabricated films may have potential in the creation of entirely new types of devices. However, the fascinating and unusual properties of these types of films must first be well characterized in order to understand them and how they would function under various conditions.

1.2 Scope

This thesis examines the mechanical response of GLAD-fabricated microstructures, toward development of devices which use GLAD geometry and characteristics in their mechanical behavior. Thin films of microsprings and microcantilevers are the configurations of interest, with some of their properties studied for the first time here. By varying the test elements (microstructure morphology, dimensions, material, and substrate conditions), the effect of each of these factors on film properties is examined. Nanoindentation testing, a method that involves the application of small forces with a specialized tip while monitoring the displacement in the film, is used to characterize the mechanical response of these films. Force-displacement plots generated from the indentations are expected to show the influence that different materials and microstructure type (microspring or microcantilever) have on film stiffness. Variations in microspring morphology are also expected to reveal trends in film stiffness. Comparisons between classic spring theory and experimentally derived data will indicate if the macroscopic formulae can be used to predict the behavior of structures orders of magnitude smaller.

Microsprings and microcantilevers are just some of the unique microstructures in thin films fabricated with the Glancing Angle Deposition (GLAD) technique, but they demonstrate its usefulness directly. Similar structures can be found in other microelectromechanical systems (MEMS) and devices, but these require an extensive number of fabrication and processing steps to achieve the complex configurations found in the multi-layered structures they employ. The GLAD technique, however, enables these columnar structures to be fabricated in a single, elegant process. The fundamental characterization and study of GLAD-fabricated microsprings is therefore required, if these unique structures are to be applied to existing MEMS applications, or to the creation of future devices.

In the following chapter, Chapter Two, a brief prelude is given on the GLAD technique and on the thin film growth mechanisms that dominate film evolution under glancing angle conditions. This provides some of the necessary background to explain

how film growth (and in particular for this work, microstructure geometry) is affected by differing deposition conditions and parameters.

The third chapter showcases the different types of films that were fabricated for testing. Microstructures included configurations of microsprings and microcantilevers grown on smooth surfaces and substrates with pre-patterned arrays. The importance of the substrate conditions, particularly with respect to previously deposited layers, show the effect that defects may have on subsequently deposited films. One testing configuration involved the fabrication of electrode layers framing the microstructured film, and a direct application that followed from this structure is described. Other films were fabricated with piezoelectric materials, which contain the ability to change their dimensions when subject to an electrical field or, conversely, to produce electrical signals when mechanically deformed. A discussion of the difficult growth of these films with details of the difficulties encountered is included. The crystalline nature of these films was explored with x-ray diffraction (XRD) and transmission electron microscopy (TEM), and results are included here. Finally, the effect of temperature during film growth was studied and is discussed in this chapter.

Chapter Four contains the crux of this work, encompassing the primary mechanical results from the testing of the films. The theory behind the formulae, which were used in the comparisons between theory and experiment, is explained. The nanoindentation procedure which was used to study the nanomechanical properties of the films is described and results from the testing of several different types of films are shown. These results are discussed and reveal the effects of variations in microstructure and geometry. The use of a finite element modeling program (ANSYS) to model the film behavior is also briefly explored, and some initial results from the modeling of the microspring films with another finite element analysis program (ALGOR) are given.

The fifth chapter focuses on a specific subset of interest, involving the determination of the films' resonant frequencies. This is an interesting part of the present work, as the resonant frequencies are also strongly affected by microstructure geometry. Several methods that were used to explore the resonance in these films are discussed and show

the complicating factors and challenges involved with frequency measurements. Although no clear cut approach exists, suggested improvements to the films are given, which could make the determination of resonance frequencies less problematic.

Chapter Six involves some intriguing films that were grown on raised mesas for ease of performing the nanoindentations. A unique edge effect was found to occur in these films, which suggests itself strongly for novel applications outside the scope of this work. Results with these films displayed their potential for use in fields such as microfluidic, biochemical, catalytic, or microreactor applications.

The resulting conclusions and suggested directions for future exploration are presented in the final chapter. Mechanical characterization of microspring and microcantilever thin films has indeed produced some interesting and valuable results, which will provide useful guidelines for further thin film research in this area. Device development using these principles is a strong possibility for future students, and – having now baselined the properties studied – future work in directly changing specific properties is made feasible. Methods for such tuning are discussed, like a critical discussion of chisel selection in the aforementioned age of stone. And as those masons did in their day, so do we imagine structures not yet built – structures of understanding, for which our present work is but a founding-stone.

CHAPTER 2
THIN FILM GROWTH MECHANISMS AND THE GLAD TECHNIQUE

2.1 Historical Aspect of Porous Thin Films

Thin films have conventionally been grown as dense, planar layers and have been utilized in a variety of fields including tribology, microelectronics, photonics, chemical, biomedical and others. The emergence of nanotechnology has led to research in more exotic porous or nanostructured thin films. While porous thin films can come in a number of forms like sol gels[1], colloids[2], ceramics[3,4], and columnar microstructures, the latter form will be considered in greater detail, being the focus of this work. In addition to taking many physical forms, porous thin films can be fabricated from a variety of different materials, with a number of different deposition methods existing to produce films that can have widely varying characteristics and properties.

Many earlier studies on the growth of porous thin films are available[5-9], and amongst these one of the earliest was by Holland[10], who investigated films deposited at extremely oblique incidence angles before 1953. In 1959, Young and Kowal[11] used substrate rotation to grow films for optical experiments, while Motohira and Taga[12] produced films with columnar structures in 1989 whose growth direction was affected by abrupt changes in incidence angles. With a few exceptions, most of the work was generally constrained to depositions grown at incidence angles of $\alpha \leq 70°$ (where α defines the angle between the source and substrate normal) and not at the higher extremes. It was not until the early 1990's that Robbie and Brett began the exploration and fabrication of highly porous thin films grown at oblique angles of incidence greater than 80°. The nature of these columnar films was found to be strongly affected by the growth mechanisms and conditions under which the films were fabricated[13]. Further details on the growth of these films are discussed shortly in this chapter.

2.2 Columnar Film Growth

The deposition of materials in vacuum environments is used extensively to produce thin films, often using some form of physical vapour deposition (PVD). This encompasses techniques like sputtering[14] and evaporation[15,16], both of which produce a vapour of the source material that travels towards and coats the desired substrates. While other deposition methods like chemical vapour deposition (CVD)[17] exist, discussion will be limited to films deposited by PVD techniques.

Most PVD thin films are grown such that the vapour flux arrives at normal incidence ($\alpha = 0°$) to the substrate plane. Upon reaching the substrate, the flux, which is in atomistic form, condenses onto the substrate at random nucleation sites. Since the depositions typically occur under high vacuum conditions, the vapour flux arrives in a collimated fashion, traveling in straight lines from the source to the substrate. The nuclei grow until they reach a critical size, after which they begin to coalesce with each other to form larger islands. Further deposition then causes the joining of these islands, creating holes and channels in a nearly continuous film, until these too are filled and a dense film results[18,19]. The films produced in this manner are made up of closely packed, columnar microstructures[20].

Virtually all parameters of the thin film deposition process can have considerable effects on film microstructure and properties[21-24]. Vacuum pressure, ambient gas during deposition, substrate temperature, material melting temperature, mobility of the material (diffusion), energy of the atomistic vapour (dependent on the deposition method), chamber cleanliness (presence of contaminants), geometry of the source and substrate, arrival rate of flux, and substrate type (surface features) for example, all have important influences on the development of the film structure and its properties in the initial and final stages.

2.2.1 Diffusion

While there are many factors that can play a part in affecting the microstructure of the film, the ratio of substrate to material melting temperature (T/T_m) and vacuum pressure

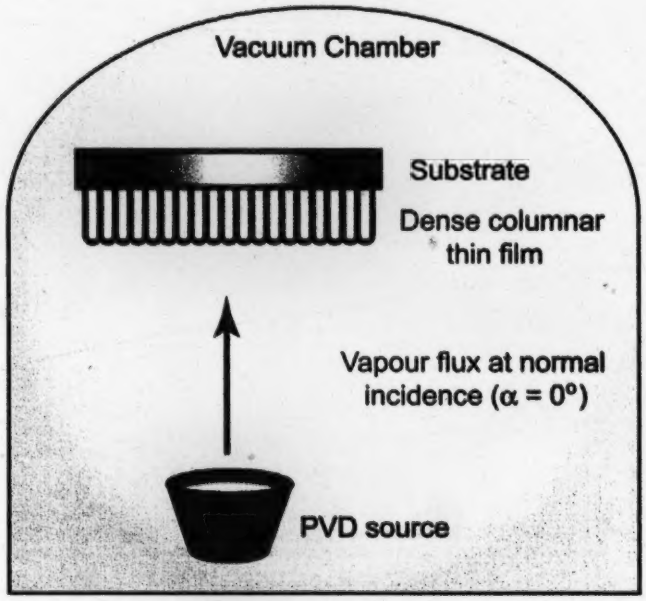

Figure 2.1: PVD deposition of a dense, columnar thin film.

are among some of the key influences. Structure zone models can be used to describe films grown under various temperature and pressure conditions[25,26]. Even at normal incidence, atomic shadowing effects[27,28] can also dominate local surface diffusion processes, resulting in films that are lower in density (by ~80%) than bulk films.

Since diffusion is a thermal process, increased temperatures can cause an increase in the diffusion of adatoms at the substrate according to the Arrhenius relation[23]:

$$D = D_o e^{\frac{-E_D}{RT}} \qquad (2.1)$$

where D is the diffusion coefficient, D_o is a constant, E_D is the activation energy for diffusion, R is universal gas constant = 8.31 J/mol K, and T is the temperature. Causes of increased temperature can come from intentional substrate heating, condensation energy, and radiant heat from the source. These sources will be discussed further in the next chapter.

When atoms first strike the substrate, they can either be immediately deflected from the surface, remain at the surface for a short period of time before re-evaporating, or adhere to the substrate and still travel over a short distance. In the final case, increases in adatom mobility can cause a decrease in film porosity and texture, as the migrating adatoms finally settle into sites of minimal energy[29,30]. This causes the columnar features to become less evident with increasing density of the film[31]. If the energy of the atoms is high enough or if high enough temperatures are reached, bulk diffusion and recrystallization of the film may even occur.

2.3 Oblique Film Growth

When the geometry of the source with respect to the substrate is altered, such that the vapour flux arrives at an oblique angle to the substrate plane, some interesting changes to the film morphology occur. Many obliquely deposited thin films are found to be

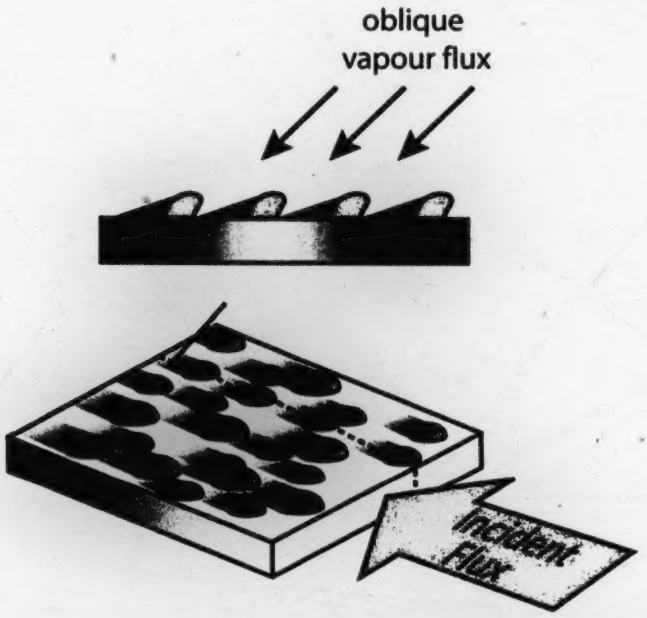

Figure 2.2: Early stages of shadowing occurring from the arrival of oblique vapour flux at high deposition angles (α).

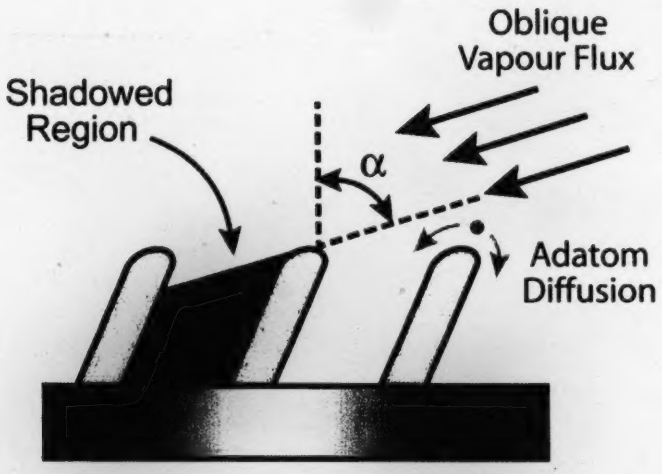

Figure 2.3: Schematic illustration showing the effects of limited adatom diffusion and enhanced shadowing.

anisotropic within the substrate plane, due to the formation of microstructures that incline towards the vapour source during the deposition[22,32-38]. During the initial stages of growth when nuclei reach a critical size, the orientation of these nuclei with respect to each other and to the incident flux (due to the line of sight arrival from the source) is such that shadowing of areas on the substrate behind these nuclei occurs. Preferential growth occurring on the nuclei eventually results in the accentuation of these features, which produces a film with distinct columnar features. Enhanced shadowing is the dominant growth process, especially under conditions of highly oblique incidence angle ($\alpha > 80^{o}$). Low substrate temperatures can limit the adatom diffusion and prevent the filling of the voided regions, also encouraging formation of individual structures.

2.3.1 Deposition Angle and Porosity

As the incidence angle is increased, the spacing of the columns also increases due to the increase in the shadowed regions. The porosity of a thin film is considerably affected by the angle of deposition[39]. With increasing deposition angles (α), comes increasing

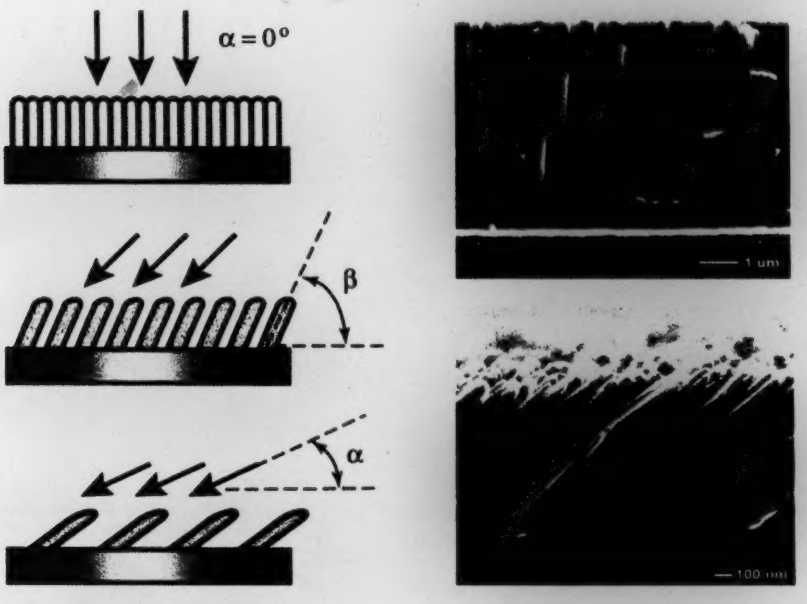

Figure 2.4: Increasing film porosity with increasing deposition angle (α). The film shown at top right is a dense ZnO film grown at normal incidence, while the film below it is a SiO film grown at α = 85°.

film porosity accordingly. For films deposited at 85 degrees, the porosity was found to be approximately 25 % that of a bulk film, depending on the deposition conditions[40].

The microstructures are inclined towards the direction of arriving flux at a column angle β which is dependent on and less than α. Columnar angle inclination tends to increase as deposition angles are increased, but can be dependent on the type of material, system base pressure, and source to substrate separation chosen as well. An earlier study by Nieuwenhuizen and Haanstra regarding thin film deposition angles and their connection with columnar inclination angles was empirically derived in 1966[41]. The relationship between α and β can generally be described according to an empirical tangent rule[42,43]:

$$\tan\beta = \frac{1}{2}\tan\alpha \qquad (2.2)$$

particularly for low angles ($\alpha \leq 60°$), while for higher angles, an expression derived by Tait[44] matched experimental results more closely:

$$\beta = \alpha - \arcsin\left[\frac{1}{2}(1-\cos\alpha)\right] \qquad (2.3)$$

In general, the column angle depends on the incident deposition angle to some degree, and to other important factors such as deposition material.

2.4 Glancing Angle Deposition

The Glancing Angle Deposition (GLAD) technique[45-50], developed by Kevin Robbie and Michael Brett in 1994, allows new forms of microstructured thin films to be grown. This technique takes advantage of certain growth mechanisms, namely enhanced

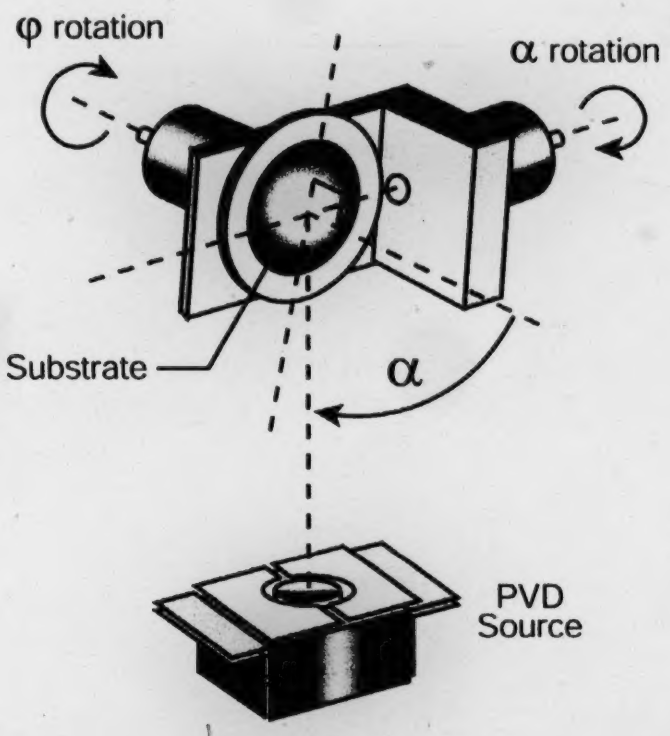

Figure 2.5: GLAD apparatus showing the flexible range of substrate movement.

shadowing and limited diffusion, to produce these unique thin films. Instead of orienting the substrate at a normal angle to the source, it is angled at a highly oblique (or glancing) angle as the name of the technique implies. The extreme oblique incidence in combination with substrate motion enables tailoring of porous thin film microstructures. By precisely varying the incident flux angle (α) and the rotation (ϕ) of the substrate, numerous thin film morphologies can be engineered with nanometer scale control. Most GLAD fabricated films are grown at deposition angles between 80° and 90°, with 85° typically used due to the good balance between film porosity and microstructure that can be achieved.

2.4.1 Effect of Substrate Motion

During the deposition of a film, motion of the substrate can be utilized to allow the growing columns to be engineered with a variety of possible morphologies[51-54]. The GLAD technique utilizes two computer controlled stepper motors to vary the motion of the substrate during deposition. Rotation occurs about an axis perpendicular to the plane of the substrate, and the incident flux angle can be modified by tilting about an axis parallel to the plane of the substrate. Labview[55] control software enables the motion of the stepper motors to be precisely controlled during the course of the deposition and allows various configuration parameters to be defined. Along with the deposition rate given by a quartz crystal thickness monitor, these parameters are utilized in determining the movement of the substrate. Consequently, the growing columns of material can be shaped into a number of desired microstructures, which can include such configurations as helices, vertical and slanted posts, zigzags, square staircase structures, and many others.

Since the inclination of the microstructures has a tendency to lean towards the direction of the incident flux, this trait was utilized when forming each of the configurations shown in Figure 2.6. The chevron film was formed by periodically switching between opposite incidence angles such that the flux arrived alternately from the left and right to form each of the "zigs" and "zags". A slow rate of rotation ϕ with

Figure 2.6: Some basic GLAD microstructures such as ZrO_2 chevrons (a), SiO helices (b), and SiO_2 post structures (c).

respect to the deposition rate at a constant angle α was used to deposit the helical film, with the substrate making a desired number of rotations during the entire deposition to form helices having the same number of turns. By increasing the rate of rotation significantly, the resulting microstructures that are formed consist of vertical columnar posts. These films are essentially the same as helical films, but with high enough spin rates to produce small enough pitches so that each 'turn' of the helices is on the same size scale as the column thickness (therefore making them indistinguishable as they instead blend together to form solid vertical structures).

2.4.2 Advanced Control and Other Microstructures

Complex shapes require advanced control of the substrate motion to maintain porosity uniformity throughout the thickness of the film that is independent of the growth angle of the microstructures. Periodically bent nematic structures are one of such examples[56]. Other kinds of structures can also be readily achieved with advancements made to the control software, further demonstrating its microstructural control capabilities. The versatility of the GLAD technique allows for a variety of deposition methods to be used to fabricate these films. In addition to standard physical vapour deposition techniques like thermal and electron beam evaporation[56] and sputtering[57], laser ablation[58] is also possible, allowing for a wide range of materials to be deposited.

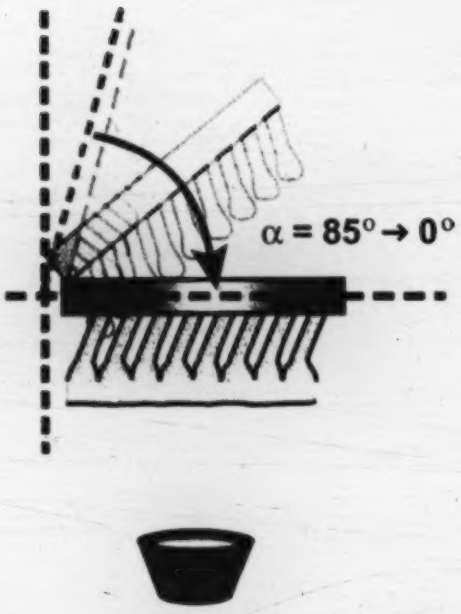

Figure 2.7: Capping layer evolution due to reduction of angle α and increase in ϕ.

Another interesting microstructure type can also be grown with the GLAD technique. Solid, dense layers can be evolved atop a porous GLAD film by reducing the incident flux angle at an exponential rate while rapidly rotating the substrate[56]. The decreasing deposition angle causes the film porosity to become reduced, with rotation of the substrate occurring to allow the film columns to thicken azimuthally. As the deposition angle is further reduced until the substrate is perpendicular to the direction of incident flux, the columns eventually meet and develop into a continuous layer. These layers serve to protect and encapsulate the porous GLAD film underneath, and can function as a base layer upon which further films could be grown, resulting in multilayered film structures (discussed further in Chapter 3).

2.4.3 Film Thickness Variation

The directionality of the evaporating atoms follows a cosine law[59], and depending on the size of the source and distance to the substrate, a variation of deposit thickness may

occur over the substrate. For films deposited with Glancing Angle Deposition, the substrate is inclined to a large degree, such that the effective spread of the substrate – as seen by the source – becomes greatly diminished, due to the high deposition angle. As a result, thickness variations between the center and edge of the substrate deviate by only a negligible amount (<10%). Any variations in thickness are also minimized by the large separation distance (typically 0.4 m) between the source and substrate.

Measurements of cross-sectional film thicknesses taken by Scanning Electron Microscope (SEM) images confirm this small variation. The three-inch diameter Silicon (Si) wafers used for the depositions were tilted at 85° to the source, and thus had a visible lateral span that was only a small fraction (7×10^{-3} m) of the total wafer diameter.

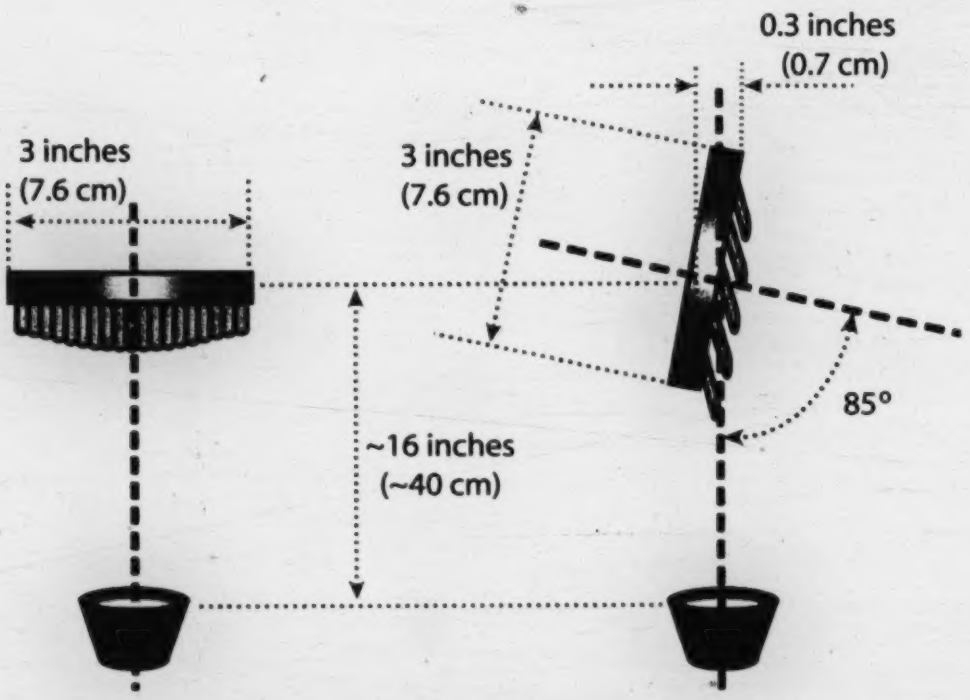

Figure 2.8: Schematic illustration showing the minimal lateral spread of the substrate as seen by the source.

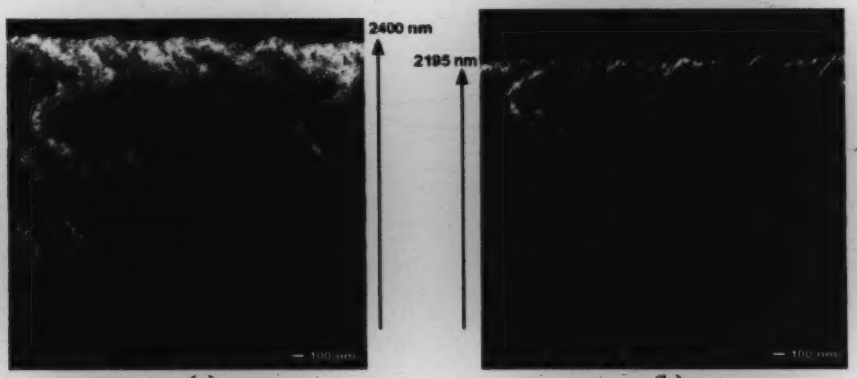

Figure 2.9: SEM images of a Ti film at the centre (a) and edge (b) of the substrate showing a slight thickness variation of ~205 nm (<10% of the total film thickness).

2.5 Other GLAD Applications

A number of research fields utilizing GLAD-fabricated thin films are being studied and areas of application range through optical, chemical, magnetic, biomedical, sensing, field emission, thermal barrier and other fields. Among these areas of interest, are devices that highlight the distinct structure of the films, and applications that exploit various film properties. The study of these specialized thin films continues to generate applications in several fields, and present research of microstructured, porous thin films is directed in areas such as those described briefly below.

2.5.1 Optical Applications

In the field of optics, the most recent work relating to applications of GLAD fabricated films involved their use for potential photonic band gap (PBG)[60] devices. Photonic band-gap crystals are periodic structures that exhibit the characteristics of a band-gap for light where propagation of electromagnetic (EM) waves within the frequency range of the band-gap is restricted[61]. These materials manipulate light through the introduction of lattice defects which allow the light to be constrained and guided. Use of a periodic square spiral microstructure was proposed by Toader and John, who

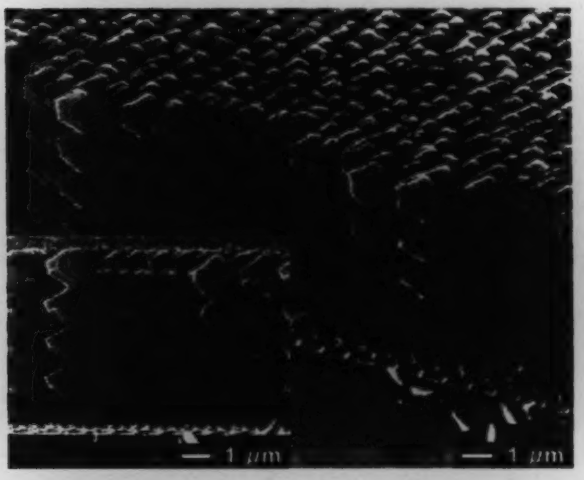

Figure 2.10: A tetragonal square spiral GLAD film (with side view inset) having potential applications as a photonic band gap material[62].

suggested that this configuration could exhibit a large three dimensional photonic band gap[62]. This morphology was fabricated with the GLAD technique by S. Kennedy, yielding the structures shown in the figure below[63]. Research in this area continues with the optimization of the microstructures and testing methods to bring potential application of these media in photonics and integrated optics.

GLAD thin films engaged in hybrid liquid crystal devices comprise another research area in the optics field. The demonstration of optical rotation in chiral films has been accomplished with studies measuring circularly polarized light transmission[64]. By incorporating liquid crystalline materials to these porous films, the resulting novel hybrid structures have shown promise for use in liquid crystal display technology. The helical GLAD film acts as an alignment or "backbone" structure for the liquid crystal (LC) material to orient itself, and greatly enhances the optical properties of the film. J. Sit demonstrated electrically induced switching in a display cell structure fabricated from chiral GLAD films embedded with liquid crystals that produced enhanced transmission differences between left and right circularly polarized light[65].

2.5.2 Sensing Applications

Due to the inherently high porosity of these films, their large surface area makes them suitable for use as sensing materials. Relative humidity sensing is only one of such applications. When GLAD structures were integrated into humidity sensing devices, extremely fast response times and wide dynamic response ranges were demonstrated in comparison to commercially available humidity sensors[66,67]. With the selection of appropriate columnar microstructures, the pore size distribution of the GLAD film could be varied to change the response characteristics of these sensors.

Other potential applications involve the use of these films in capacitive devices, devices capable of sensing various chemicals, or those that contain catalytic surfaces. An initial study in collaboration with Ford Research involved the evaluation of catalytic behaviour in porous GLAD platinum (Pt) films[68]. Porous, columnar titania (TiO_2) films are another catalytic medium that have been found to improve photocatalytic and photovoltaic efficiencies[69,70]. In the area of microfluidic systems, surface area enhancement of a microchannel produced an increase in surface area by two orders of magnitude after a GLAD film was deposited on it[71]. This could promote increased reactions with the fluids passing through it, or even serve as a filter for the separation of materials.

2.5.3 Periodic Structures

Periodic GLAD structures were made possible by the alteration of substrates prior to deposition. The films that were formed after deposition onto these tailored substrates have unique properties that showed a great deal of promise for uses in areas like the PBG work described above and other optical areas. An array of regularly spaced features could be prepared on a photoresist coated substrate using electron beam lithography. Hot embossing of plastics that become "micro-stamped" with the periodic features have also been achieved and used for subsequent depositions[72]. The usefulness of these pre-seeded substrates has been valuable for the creation of films where well-ordered microstructures are desired.

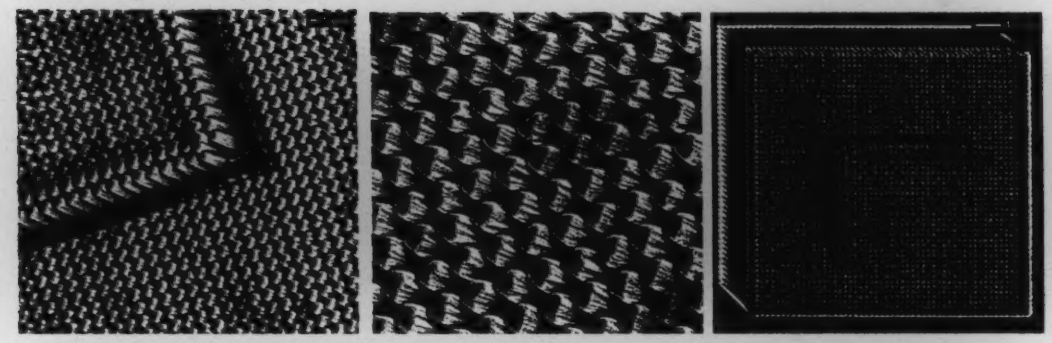

Figure 2.11: A periodic film of SiO posts deposited onto a photoresist array.

Regularly spaced features can be created in perforated (inverse) films as well[73]. Using a GLAD film as a template, photoresist or spin-on glass was added to fill the areas between the microstructures and later etched back slightly to reveal the tops of the GLAD microstructures. The perforated film was created when the GLAD film itself was etched away, leaving behind a porous medium having structured pores. These too could have filtration purposes, but more significantly, allow the growth of GLAD films with materials that are normally difficult to deposit with good microstructure formations. Copper is one of such materials that K. Harris was able to electroplate through the open pores of a perforated film to create a nearly identical film compared to the original after removal of the photoresist.

2.5.4 Thin Film Simulation

A three dimensional ballistic deposition simulator, *3D-FILMS*, reported by T. Smy has been developed for modelling thin film structures and depositions. The simulator can correctly reproduce aspects of column morphology, column growth competition and film density in GLAD films, revealing much about film evolution at all stages of growth. Fundamental growth studies of thin films done by D. Vick corroborate the predicted microstructures given by the simulator[74]. With the ability to accurately model real films, an investigation of properties such as porosity and material dependence effects could be

used to optimize the effects of process parameters on GLAD structures. The simulator could then enable new film designs to be tested and evaluated before actual fabrication.

2.5.5 Summary

These are just a few of the many areas being studied and developed by the GLAD research group. The extent of topics involving GLAD films is far too numerous to be described in great detail here. In summary, the flexibility of GLAD thin films makes their usefulness pertinent to an extensive range of current research domains.

2.6 References

[1] G. Piccaluga, Sol-Gel Preparation and Characterization of Metal-Silica and Metal Oxide-Silica Nanocomposites, Switzerland: Trans Tech Publications, 2000.

[2] S. Sakka, Sol-Gel Science and Technology: Topics in Fundamental Research and Applications, Boston: Kluwer Academic, 2002.

[3] S. Kondoh and Y. Iwamoto, J. Am. Ceram. Soc., **82** , 209 - 212 (1999).

[4] M.Yoshikai, M.Machida, K.Eguchi and H.Arai, Chemistry Letters, **11**, 1897 (1989).

[5] S. Lichter and J. Chen, Physical Review Letters, **56**, 1396 (1986).

[6] D.O. Smith, M.S. Cohen and G.P. Weiss, J. Appl. Phys., **31**, 1755 (1960).

[7] W. Metzdorf and H.E. Wiehl, Phys. Stat. Sol.,**17**, 285 (1966).

[8] M. J. Bloemer, T. L. Ferrell, M. C. Buncick, and R. J. Warmack, Phys. Rev. B., **37**, 8015 (1988).

[9] D. Le Bellac, G. A. Niklasson, C. G. Granqvist, Europhys. Lett., **32**, 155 (1995).

[10] L. Holland, J. Opt. Soc. Am., **43**, 376 (1953).

[11] N. O. Young and J. Kowal, Nature **183**, 104 (1959).

[12] T. Motohiro, Y.Taga, Appl. Opt., **28**, 2466 (1989).

[13] K. Robbie, L. J. Friedrich, S. K. Dew, T. Smy, and M. J. Brett, J. Vac. Sci. Technol. A, **13**, 1032 (1995).

[14] B. N. Chapman, Glow Discharge Processes, New York: Wiley, 1980.

[15] E. B. Graper, J. Vac. Sci. Technol., **8**, 333 (1971).

[16] R. Glang and L. I. Maisel, Handbook of Thin Film Technology, New York: McGraw-Hill, 1970.

[17] D. L. Smith, Thin Film Deposition: Principles and Practice, New York: McGraw-Hill, 1995.

[18] R. W. Vook, Int. Metals Rev., **27**, 209 (1982).

[19] D. W. Pashley, M.J. Stowell, J. Vac. Sci. Technol. **3**, 156 (1966)

[20] H. J. Leamy, G. H. Gilmer, A. G. Dirks, Current Topics in Materials Science, **6**, Amsterdam: North Holland Publishing Co., 1980.

[21] J. L. Vossen and W. Kern, Thin Film Processes, Academic Press: New York (1978).

[22] H. K. Pulker, Coatings on Glass, Elsevier Press: Amsterdam (1984).

[23] M. Ohring, The Materials Science of Thin Films, Academic Press: Boston (1992).

[24] J. F. O'Hanlon, A User's Guid to Vacuum Technology, Wiley Press: New York (1989).

[25] J. A. Thornton, Annu. Rev. Mater. Sci., **7**, 239 (1977).

[26] A. Movchan and A. V. Demchishin, Phys. Met. Metallog., **28**, 83 (1969).

[27] H. König and G. Helwig, Optik, **6**, 111 (1950).

[28] D. O. Smith, M. S. Cohen, and G. P. Weiss, J. Appl. Phys., **31**, 1755 (1960).

[29] J. E. Mahan, Physical Vapour Deposition of Thin Films, New York: Wiley, 2000.

[30] J. Venables, Introduction to surface and thin film processes, Cambridge: Cambridge University Press, 2000.

[31] D. K. Pandya, A. C. Rastogi, and K. L. Chopra, J. Appl. Phys., **46**, 2966 (1975).

[32] D. L. Smith, Thin-Film Deposition, Principles and Practice, McGraw-Hill, New York (1995).

[33] E. S. Machlin, Material Science in Microelectronics I, The Relationships between Thin Film Processing and Structure, New York: Giro Press, 1995.

[34] F. C. Matacotta, G. Ottaviani, Eds., Science and Technology of Thin Films, Singapore: World Scientific Pub., 1995.

[35] P. Meakin, P. Ramanlal, L. M. Sander, R. C. Ball, Phys. Rev. A, **34**, 5091 (1986).

[36] G. W. Mbise, G.A. Niklasson, C. G. Granqvist, J. Appl. Phys., **77**, 2816 (1995).

[37] Y. Takeda, T. Motohiro, T. Hioki, S. Noda, J. Vac. Sci. Technol. B, **16**, 7 (1998).

[38] P. Keblinski, A. Maritan, F. Toigo, J. R. Banavar, Phys. Rev. Lett. , **74**, 1783 (1995).

[39] H. van Kranenburg, and J. C. Lodder, Mater. Sci. Eng. R, **11**, 293 (1994).

[40] K. D. Harris, J. R. McBride, K. E. Nietering, M. J. Brett, Sensors and Materials, **13**, 225 (2001).

[41] J. M. Nieuwenhuizen and H. B. Haanstra, Philips Tech. Rev., **27**, 87 (1966).

[42] N. G. Nakhodkin and A. I. Shaldervan, Thin Solid Films, **10**, 109 (1972).

[43] A. G. Dirks and H. J. Leamy, Thin Solid Films, **47**, 219 (1977).

[44] R. N. Tait, T. Smy, and M. J. Brett, Thin Solid Films, **226**, 196 (1993).

[45] K. Robbie and M. J. Brett, J. Vac. Sci. Technol. A, **15**, 1460 (1997).

[46] K. Robbie, M. J. Brett, and A. Lakhtakia, Nature, **384**, 616 (1996).

[47] K. J. Robbie and M. J. Brett, "Method of depositing shadow sculpted thin films", U. S. Patent No. 5,866,204, issued February 2, 1999.

[48] K. J. Robbie and M. J. Brett, "Glancing angle deposition of thin films", U. S. Patent No. 6,206,065, issued March 27, 2001.

[49] K. J. Robbie and M. J. Brett, "Shadow sculpted thin films", U. S. Patent No. 6,248,422, issued June 15, 2001.

[50] K. J. Robbie and M. J. Brett, "Shadow sculpted thin films", Canadian Patent Application No. 2,182,452, 1996.

[51] K. Robbie, M. J. Brett, and A. Lakhtakia, J. Vac. Sci. Technol. A, **13**, 2991 (1995).

[52] A. Lakhtakia, R. Messier, M. J. Brett, and K. Robbie, Innovations in Materials Research, **1**, 165 (1996).

[53] K. D. Harris, D. Vick, E. J. Gonzalez, T. Smy, K. Robbie, and M. J. Brett, Surface and Coatings Technology, **138**, 185 (2001).

[54] S. R. Kennedy, M. J. Brett, O. Toader, and S. John, Nanoletters, **2**, 59 (2002).

[55] K. Robbie, J. C. Sit, and M. J. Brett, J. Vac. Sci. Technol. B, **16**, 1115 (1998).

[56] K. Robbie, C. Shafai and M. J. Brett, J. Mat. Res., **14**, 3158 (1999).

[57] J. C. Sit, D. Vick, K. Robbie, and M. J. Brett, J. Mat. Research, **14**, 1197 (1999).

[58] D. Vick, Y. Y. Tsui, M. J. Brett, R. Fedosejevs, Thin Solid Films, **350**, 49 (1999).

[59] L. I. Maissel and R. Glang, Handbook of Thin Film Technology, New York: McGraw-Hill, 1970.

[60] S. John, Phys. Rev. Lett., **53**, 2169 (1984).

[61] S. John, Phys. Rev. Lett., **58**, 2486 (1987).

[62] O. Toader and S. John, Science, **292**, 1133 (2001).

[63] S. R. Kennedy, M.J., Brett, O. Toader, and S. John, Nano Lett., **2**, 59 (2002).

[64] J. C. Sit, D. J. Broer and M. J. Brett, Adv. Mater., **12**(5), 371 (2000).

[65] J. C. Sit, D. J. Broer and M. J. Brett, Liquid Crystals, **27**(3), 387 (2000).

[66] A.T. Wu, M. Seto, and M.J. Brett, Sens. Mater, **11**, 493 (1999).

[67] A.T. Wu and M.J. Brett, Sens. Mater., **13**, 399 (2001).

[68] W. Qu and J. U. Meyer, Sensors and Actuators B, **40**, 175 (1997).

[69] L. B. Kriksunov and D. D. Macdonald, Sensors and Actuators B, **32**, 57 (1996).

[70] J. D. Canaday, A. K. Kuriakose, T. A. Wheat, A Ahmad, J. Gulens and B. W. Hildebrandt, Solid State Ionics, **35**, 165 (1989).

[71] K. D. Harris, M. J. Brett, T. J. Smy, C. Backhouse, J. Electrochem. Soc., **147**, 2002 (2000).

[72] B. Dick, J. C. Sit, M. J. Brett, I. M. N. Votte and C. W. M. Bastiaansen, Nano. Lett., **1**, 71, (2001).

[73] K. D. Harris, K. L. Westra and M. J. Brett, Electrochemical and Solid-State Letters, **4**(6), P. C39 (2001).

[74] D. Vick, B. Dick, S. Kennedy, T. Smy, and M. J.Brett, Mat. Res. Soc. Symp. Proc., **648**, P. 3.43.1 (2000).

CHAPTER 3
FABRICATION OF FILMS FOR TESTING

3.1 Introduction

The mechanical formats of interest for fabrication were helically shaped microstructures and microcantilevers. These structures could be compared with their macroscopic counterparts, whose behavior was expected to correlate analogously. A set of films of specific geometries and composition was grown with the GLAD technique to study various mechanical film properties and dependencies. These included porous, capped and uncapped microspring thin films, slanted posts, films on patterned arrays of photoresist and embossed plastic (compared to plain Si substrates), and also some standard dense films.

3.2 Physical Vapour Deposition Processes

A number of film growth methods incorporate physical vapour deposition. These deposition methods include evaporation (thermal and electron beam), sputtering, pulsed laser deposition, and many other techniques. Physical vapour deposition fundamentally involves the coating of desired substrates through the vaporization of material that is transferred on an atomic level. The major steps involved with PVD consist of the evaporation, transport, reaction (if any), and finally the deposition of the material onto the substrate[1]. In the first step, the material becomes transformed into molecular form and can be accomplished several ways by the evaporation techniques discussed in the next few sections. The transport of molecules and atoms towards the substrate can depend on factors such as vacuum pressure and chamber conditions. If a gas is introduced during deposition, the molecules and atoms could react with the gas to form new molecules. Upon reaching the substrate, further reactions could be undergone by the evaporant. All

of the films that were fabricated for mechanical testing were deposited with either thermal or electron beam evaporation or sputtering.

3.2.1 Thermal and Electron Beam Evaporation

In thermal evaporation, the source -- which consists of the material to be deposited -- is placed into an evaporation boat or crucible (typically composed of Tungsten or Molybdenum due to their high melting point temperatures), and a current is passed through to heat the material inside the boat until evaporation or sublimation occurs. The deposition chamber is evacuated to low pressures that range from 10^{-4} to 10^{-9} Torr for evaporation, with 10^{-6} Torr (7.6×10^{8} atm or 1.3×10^{-4} Pa) being a typical value. At these pressures, the average mean free path (λ) of the evaporated atoms can be calculated by combining the Maxwell-Boltzmann distribution function for molecular velocities[2] with the ideal gas equation[3] to yield:

$$\lambda = \frac{kT}{p\pi\sqrt{2}d_o^2} \qquad (3.1)$$

where k is the Boltzmann constant = 1.38×10^{-23} J/K, T is the temperature in Kelvin (~300K), p is the pressure in Pa, and d_o is the molecular diameter (typically ~3Å). This causes the mean free path to be on the order of a few metres, which when considering the dimensions of the deposition chamber, means that molecules collide only with the chamber walls and travel in straight lines towards the substrate. This property has significant effects, particularly with GLAD film fabrication, since collimated molecular paths from the source to the substrate are crucial for the porous, columnar microstructures to form and grow.

In electron beam evaporation, the deposition process is similar, with the exception of the heating process. A beam of electrons is created by passing electrons generated by a Tungsten cathode (accelerated by approximately 20 kV) through an opening in the anode. The beam is rastered over the evaporant of choice to cause heating and melting, and enables a greater range of materials to be deposited due to the higher melting point materials that can be accommodated. Movement and focusing of the electron beam is

controlled by a transverse magnetic field for 270° deflection of the beam so that the electrons strike the surface of the evaporant source.

3.2.2 Sputtering

The sputtering process is a deposition technique that involves the emission of small particles, much like its dictionary definition. Several methods of sputtering exist, including ion beam, magnetron, diode, triode, bias, asymmetric bipolar pulsed dc sputtering, high frequency (RF) glow discharge, and others[4-8]. An additional sputter variation incorporates long-throw/low–pressure sputtering (LTLP), which allows the formation of some GLAD microstructures[9]. On a fundamental level, the sputtering process essentially involves the bombardment of a target consisting of the material to be deposited with energetic particles. A heavy inert gas such as Argon (Ar) is introduced into the chamber and serves as the medium in which a discharge is initiated and sustained near the target, which becomes the cathode. Positive Ar ions in the discharge become accelerated towards the cathode plate and bombard it to cause sputtering. The momentum exchange of the particles with the target causes the ejection of material in atomic form. These neutral atoms then travel away from the target towards the substrate, which subsequently becomes coated. This process occurs inside a chamber that is under vacuum, but at pressures several orders of magnitude higher than that used in evaporation (typically 7×10^{-3} Torr = 1.1×10^{5} atm = 0.93 Pa). As a result, the paths of the sputtered atoms are greatly diverted and redirected due to the large number of collisions with other molecules and gases present inside the chamber. In the LTLP approach, pressures that are slightly lower than what is used in conventional sputtering are used (~1×10^{-3} Torr). The outcome of this reduced pressure is a larger mean free path that is on the order of several centimeters (compared to a few millimeters in the traditional case), and is sufficient to enable the shadowing effect to direct the formation of porous, aligned microstructures.

Other reactive gases may be introduced in addition to Ar (such as Oxygen or Nitrogen, for example) in reactive sputtering to produce compounds of oxides or nitrides. Because the addition of these gases may cause deposition pressures to be higher, the

mean free path of sputtered flux is lowered and atoms are scattered on route towards the substrate. Consequently, deposition rates can become reduced due to the diverted paths that the atoms take after collisions.

Magnetron sputtering[10] offers some advantages with regard to high deposition rates and area, low substrate heating, and was used for the films that required sputtering. This is a favoured sputter deposition method that involves the use of a magnetic field (with field strength ~300 Gauss) that causes electrons to be contained in a helical trajectory around magnetic field lines above the cathode. Because these electrons experience the Lorentz force in addition to the electric field force, they become trapped in the glow, and a large number of ions are produced by collisions with the electrons to result in higher sputter rates.

3.3 Fabrication of Microspring Thin Films

A compilation of microspring films was fabricated for testing. For each deposition, the substrate was inclined at an 85° angle of incidence with respect to the source. This

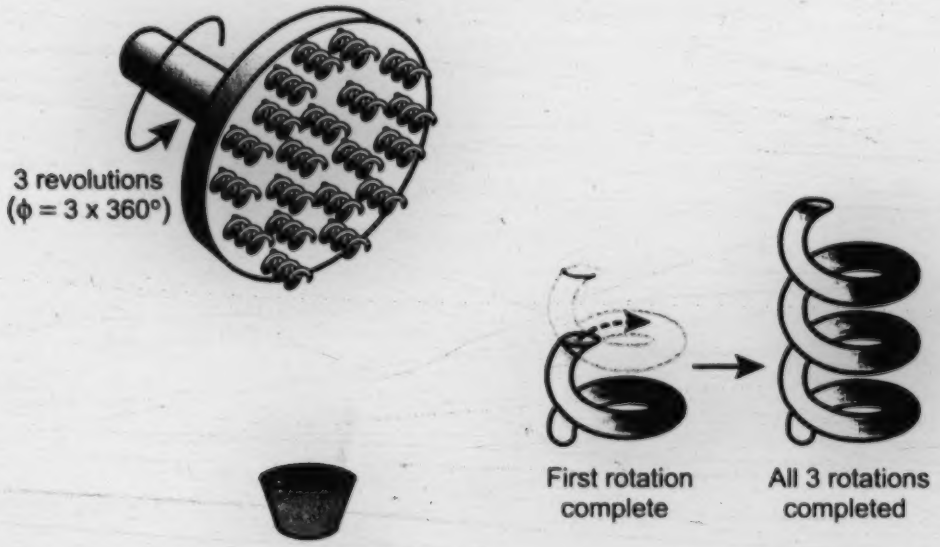

Figure 3.1: Schematic illustration of the growth of a 3-turn microspring.

angle was chosen in order to achieve a suitable compromise between reasonable deposition rates and low microspring densities. While maintaining this incidence angle, the substrate was rotated the desired number of times in coordination with the deposition rate to achieve selected microspring geometries. For most films, deposition rates varied between 10 – 20 Å/s.

To grow films of the same thickness with varying pitches (the height of a single turn), the speed of the rotation was increased or decreased accordingly over a set length of time. Films containing microsprings of identical pitch but with varying numbers of turns were grown by retaining the same rotation rate for a corresponding number of revolutions.

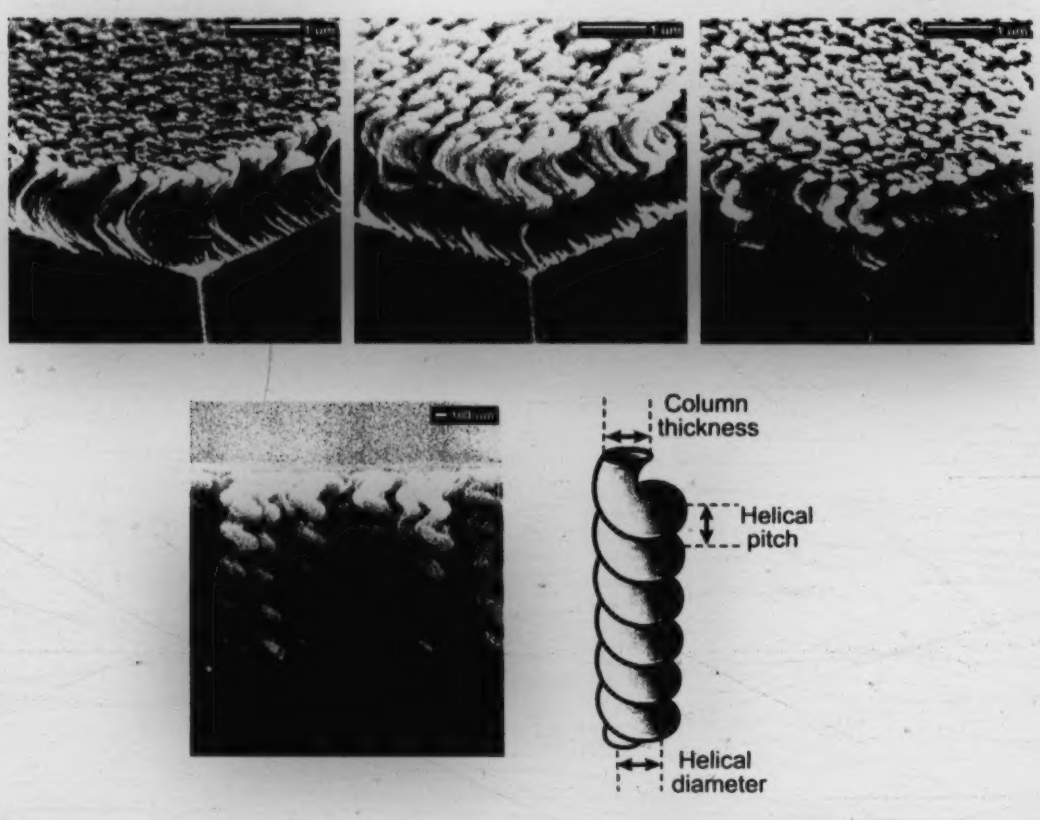

Figure 3.2: Examples of uncapped SiO microspring films of similar thickness with the last film having an unsuitable auger-like shape.

3.3.1 Microspring geometries

One, 2-, 3-, 4-, 6-, and 12-turn films of Silicon Monoxide (SiO) having the same film thickness were fabricated to study the effect of microspring geometry on spring constant. These films were grown in an evaporation chamber by thermal evaporation using a Drumheller sublimation source[11] situated approximately 0.4 m away from the substrate. Upon testing the films (discussed in the following chapter), it was found that the microsprings with higher numbers of turns were unsuitable due to the inappropriate shape that was taken on when fabricated. An auger-like appearance (with cross-sectional width comparable to helical pitch and diameter) that no longer resembled the form of a spring could be seen for the 6-turn film. Subsequently, only the films containing fewer turns were used for testing, with parameters for the 1-, 2-, and 3-turn films given in Table 3.1..

Measurements of the film height, column diameter, coil radius, and rise angle were taken from SEM images with the area to be measured enlarged as much as possible. A maximum uncertainty of approximately ± 5 percent from the values listed was expected, given the method of measurement. The areal number density of microstructures was expected to have an uncertainty of approximately 10 percent, due to the random distribution of the microsprings. Thin film Young's Modulus values and Poisson's

Table 3.1: Geometrical parameters of a set of microspring films tested.

Thin Film Sample	Film Height (μm) ± 5%	Nominal Column Diameter (nm) ± 5%	Nominal Coil Radius (nm) ± 5%	Young's Modulus (GPa)	Poisson's Ratio	Areal Number Density (#/μm^2) ± 10%	Rise Angle (deg) ± 5%
SiO (1 turn)	1.3	115	280	92	0.3	10	37
SiO (2 turns)	1.9	110	190	92	0.3	10	39
SiO (3 turns)	1.8	110	165	92	0.3	10	30
Ti (3 turns)	2.4	115	200	110	0.34	15	33
Cr (3 turns)	1.8	150	190	140	0.21	3.2	27

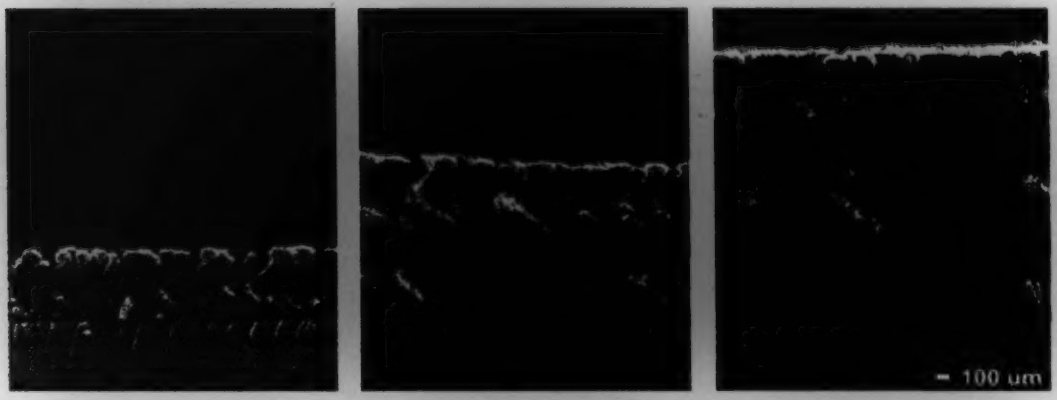

Figure 3.3: Examples of uncapped SiO microspring films with the same pitch and varying numbers of turns.

Ratios for Titanium (Ti) and Chromium (Cr) were taken from published values[12] and the Young's Modulus for SiO thin films was also found in literature[13]. Since no published values for the Poisson's Ratio of SiO could be found, a typical value of 0.3 was chosen, with most materials having a ratio that is close to this number. Other films having the same pitch, but with varying numbers of turns (and therefore having multiple thicknesses of the single turn film) were fabricated. These films had helical pitches of ~500nm and ranged from 1 to 6 turns.

3.3.2 Other Microspring Materials

Titanium and Chromium microsprings films were also fabricated with the 3- turn geometry to compare the effects of different materials on stiffness dependency. Both of these films were grown by electron beam evaporation (with 200-750 mA beam current and 7.06 V voltage) using a similar setup as that for the thermally deposited films. Other materials like Aluminum (Al), Zinc Sulfide (ZnS), Zinc Oxide (ZnO), and Lithium Niobate ($LiNbO_3$) were also employed, but without suitable results or microstructures due to difficult material properties and to the complexity associated with depositing stoichiometric compounds. This is further discussed in the next section regarding piezoelectric materials.

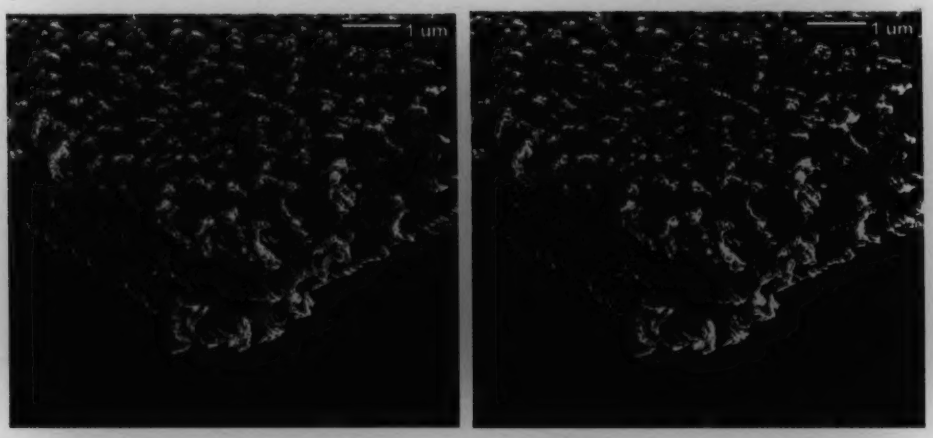

Figure 3.4: Ti and Cr microsprings fabricated with electron beam evaporation.

3.3.3 Capped Microsprings

Dense capping layers are sometimes desired when growing multilayered films. They serve several purposes, from encapsulating and protecting the porous film beneath it, to serving as a foundation upon which further layers, such as electrodes, can be grown. A number of microsprings were fabricated with capping layers surmounting the porous region of the films. These layers were evolved by dynamically reducing the incident flux angle from 85° to 0° at an exponential rate while rapidly rotating the substrate to create a transition from porous, columnar phase to solid phase[14]. An exponential rate of change was found by K. Robbie to produce the best capping layers with low overall stresses and no cracks[15]. The reduction of the flux angle followed the exponential equation below:

$$\alpha(i) = \alpha_o + (90 - \alpha_o) * \frac{(e^{\frac{t(i)-t_c}{tc}*m} - e^{-m})}{1 - e^{-m}} \qquad (3.2)$$

where i is the time starting at zero until the final thickness is achieved, $\alpha(i)$ is the angle at time i, α_o is the incident angle subtracted from 90 degrees, t(i) is the thickness at time i, t_c is the final thickness, and m is a variable exponential parameter typically set to 2 or 3. The rate of rotation was dependent on the deposition rate, as the capping layer portion of the deposition was treated like the growth of a vertical columnar film[16]. Rapid rotation of

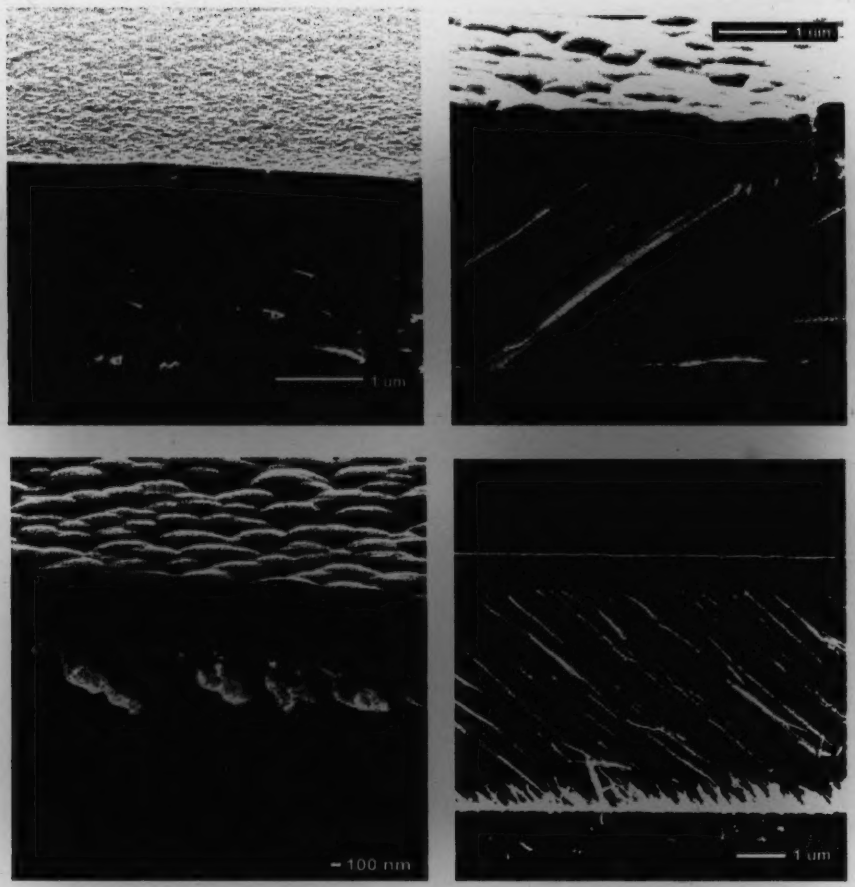

Figure 3.5: Capped SiO microspring and microcantilever films.

the substrate would result in the growth of vertical columnar microstructures. Since the incidence angle was gradually being reduced until it reached normal incidence, the columns began to grow wider and thicker until they eventually joined together to form a continuous film.

3.4 Fabrication of Inclined Microcantilevers

Slanted post films consisting of inclined columns were also fabricated to test for their mechanical properties. As one of the simplest structures, these films were expected to

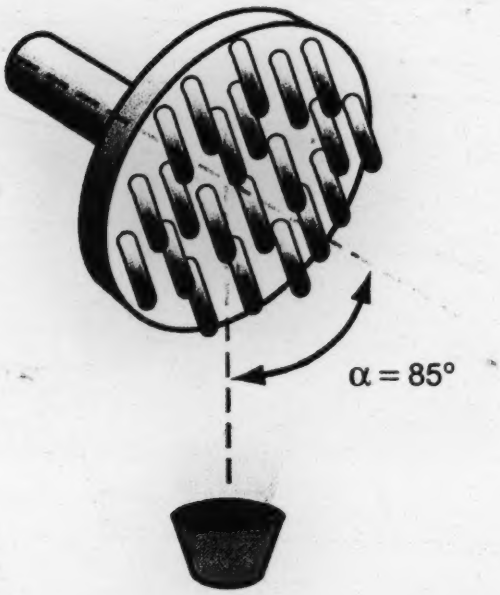

Figure 3.6: Schematic illustration of the growth of slanted posts.

behave like "microcantilevers", and as such, have predictable dependencies on geometry and material. During the fabrication of these films, the substrates were tilted at an incidence angle of 85° and held stationary throughout the depositions. This large alpha value ensured individual, isolated posts that did not join with neighboring columns and whose forms were simpler to compare to theoretical models.

3.4.1 Ordered Arrays Versus Random Films

While some of the post films were grown on plain Si substrates, the addition of a patterned layer to the Si wafers enforced the periodicity of the films and resulted in orderly arrays of inclined microcantilevers. This was a beneficial aspect because the porosity and spacing of the columns could be explicitly controlled and more readily measured. Likewise, the final geometry of the columns was more easily viewed and measured. Conventional films grown on plain substrates resulted in random placements of the columns, so the ability to control the location where each column commenced

growth was an exciting prospect[17]. Several factors had an influence on the films that were grown on the patterned arrays. The size of the seed elements, their spacing, and the deposition conditions (incidence angle, type of substrate motion) all affected the films' structures. Spacing of the seed elements, in particular, required an appropriately chosen separation in order for films to follow the periodicity of the array. Since most GLAD films are dominated by surface shadowing, optimal seed separation could be approximated by:

$$\delta = \frac{t\tan(\alpha)}{\sqrt{2}} \tag{3.3}$$

where δ and t are the seed separation and thickness, respectively[18,19]. The types of pattern layers included embossed polymeric arrays used by B. Dick[20,21] and patterned photoresist used by S. Kennedy[22]. A nanoimprinting[23] technique was used to form the plastic arrays. This process involved the use of silicon calibration gratings as the masters

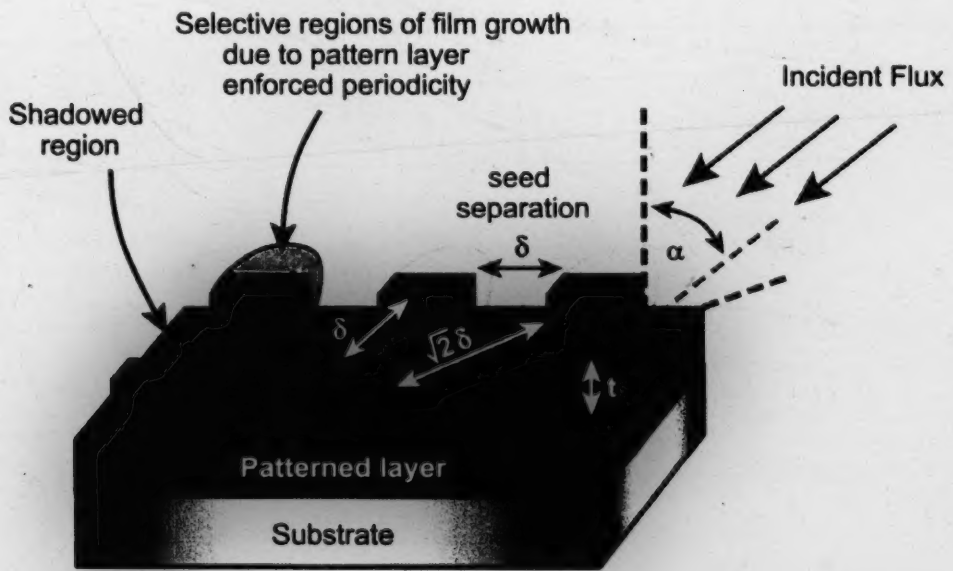

Figure 3.7: Periodicity in the film is imposed by the addition of a patterned layer having seed elements to control where columnar film growth begins.

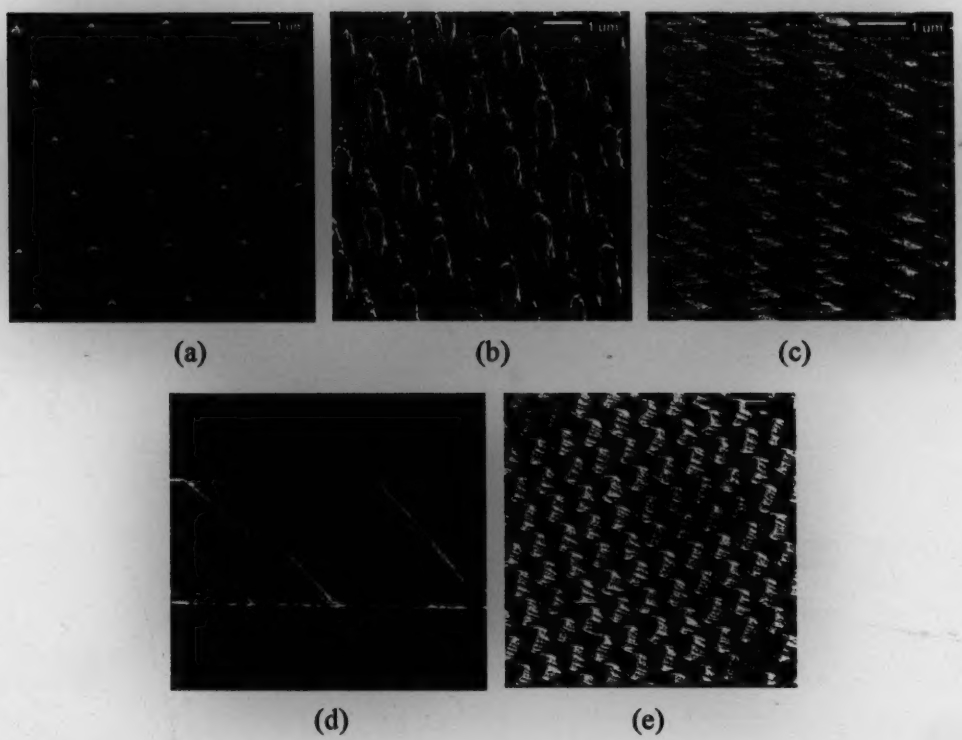

Figure 3.8: Embossed polymeric array in (a) with periodic Ni slanted films in (b) and (c), random SiO slanted post film on plain Si in (d), and an array of SiO posts on patterned photoresist in (e).

to create embossed Teflon films through heated compression molding. The Teflon films were then used as the masters for the embossing of epoxy resins to finally produce the periodic arrays that subsequent films were deposited onto.

The intent for this thesis arising from the use of patterned substrates leads to the growth of helices on these substrates. Although a seemingly straightforward idea, good helical microstructures were difficult to grow on the seed elements. The width of the microstructures was strongly affected by the orientation of the seeds with respect to the incident flux and the seed size (approximately 500 nm in width). This was far too wide for growing the optimal microspring geometries (with regard to the film thickness) that were desired, and resulted in thick, quasi-helical microstructures. The cross-sectional

width of one of these microstructures was quite large in comparison to the helical diameter and was not desirable for the determination of any mechanical properties due to the distorted helical shapes that were produced. Smaller seeds were only recently possible[24], but could only be produced over a very small area, making the location of the patterned area difficult to find and test for nanoindentation experiments.

3.5 Growth of Piezoelectric Films: Dense and Porous

The fabrication of piezoelectric GLAD films was undertaken, as it was anticipated that these films might be easier to actuate. The application of a voltage to a piezoelectric material makes it deform according to the inverse piezoelectric effect, and in contrast, the deformation of a piezoelectric material will then produce a voltage according to the piezoelectric effect[25]. However, difficulty with achieving stoichiometric films was a problem that ultimately affected how strongly piezoelectric (if at all) the films were. In order to successfully grow the more complex compounds like perovskites (piezoelectric ceramics), intricate deposition procedures would have had to involve the management of several factors such as temperature, introduction of specific gases at particular flow rates during the deposition, and a technique that would adequately allow these types of materials to be processed[26]. There would also be a strong likelihood that the films would

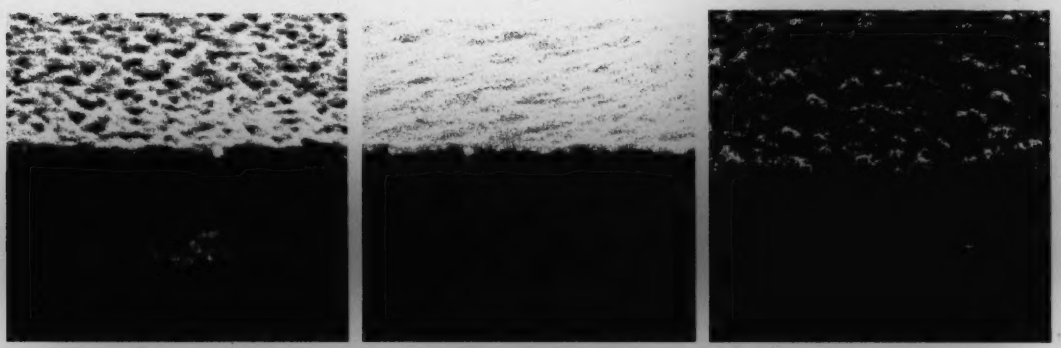

(a) (b) (c)

Figure 3.9: Sputtered ZnO films with (a) dense microstructure, (b) attempted "helical" microstructure, and (c) pulsed laser deposited ZnO.

require poling[27,28] in order to orient the piezoelectric domains. If the films did not have the proper proportion of materials to begin with, this would not be a beneficial step for a material that was not piezoelectric. Dense Zinc Oxide (ZnO) films could be reactively sputtered[29,30] and were found to be piezoelectric to some extent, but growing *porous*, microstructured, piezoelectric ZnO films was highly problematic. Elevated ambient pressures inside the sputtering chamber (due to the introduction of oxygen gas for reactive sputtering) scattered the Zn atoms, and was likely to have prevented the formation of porous microstructures. Since chamber pressures were close to 7×10^{-3} Torr, using Equation 3.1 yields a mean free path that is under a centimetre. This would mean that particles traversing the distance between target and substrate (approximately 0.16 m) would undergo several collisions and not arrive in a collimated fashion at the substrate. Porous, sputtered GLAD films have been achieved with other materials[31], but were not reactively sputtered, allowing chamber pressures to be lower. Pulsed laser deposition[32] of ZnO was also attempted, but resulted in inconsistent films that did not contain the correct c-axis orientation[33].

Other materials including Aluminum Nitride (AlN), Zinc Sulfide (ZnS), and Lithium Niobate ($LiNbO_3$) were used to grow additional films, but did not appear to be piezoelectric. Most were probably not piezoelectric, due to the difficulty with obtaining accurate stoichiometric ratios. Dense AlN films were extremely difficult to deposit since a biased sputtering technique[34] was required, and produced extremely low deposition rates of approximately 1 Å/s. Combined with the high ambient Nitrogen gas pressure (7 mTorr) needed to reactively sputter the Al target, it was also unlikely that columnar films could be formed. For the ZnS films, a strong sulfur smell could be detected in the chamber after depositing this compound, and indicated that the deposition chamber was likely becoming contaminated with the sulfur. Therefore, further depositions using this material were discontinued. The main issue with depositing the $LiNbO_3$ films was with achieving the proper stoichiometric ratios of each material ($LiNbO_3$ is a difficult perovskite to deposit), even though acceptable microstructures could be achieved. In summary, it was determined that no advantage existed in using piezoelectric materials,

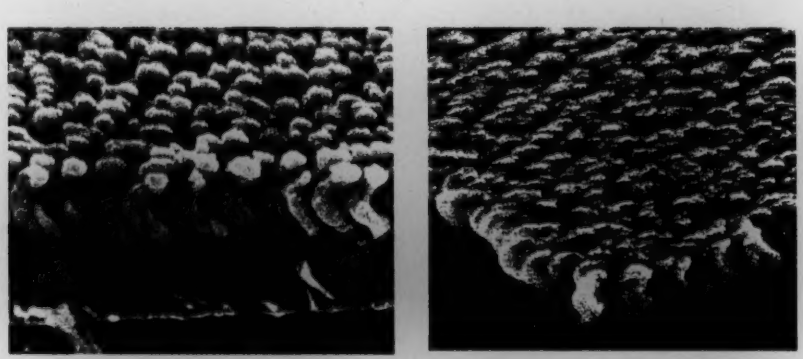

Figure 3.10: Porous helical $LiNbO_3$ (at left) and ZnS (at right) films.

due to the complexities and difficulties involved with their fabrication. SiO was used for any further film fabrications since it has demonstrated good microstructural properties.

3.6 Other Characterization

3.6.1 Metallization Layers

Some film and device structures reported later required metallization layers bounding the helical film. The type of substrate metallization layer was revealed to have a significant effect on subsequent films fabricated on them. Thermally evaporated

Figure 3.11: An approximately 75 nm thick Al metallization layer showing a high degree of roughness in comparison to an Au layer of similar thickness.

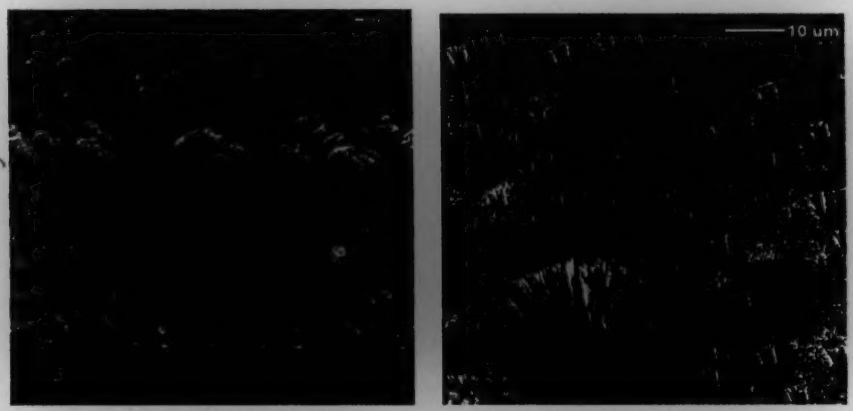

Figure 3.12: Nodular growths in SiO films that were subsequently formed on the Al coated substrates.

aluminum (Al) tended to produce rougher surfaces that created nodular growths in the films[35,36,37], making them unusable for testing, as shown in Figures 3.11 and 3.12. A thin sputtered layer of gold (Au) was found to produce a smoother surface that minimized and eliminated any further nodular growths. Subsequent electrode layers were then fabricated with Au layers having thicknesses of approximately 50 nm.

3.6.2 X-Ray Diffraction and Transmission Electron Microscopy

Some general characterization of these films included X-ray diffraction (XRD) and Transmission Electron Microscopy (TEM) as a means to examine the internal structure of GLAD-fabricated thin films. XRD spectra can determine if the sample is crystalline or not, and if there is any preferred orientation. XRD spectra of these films usually contain relatively broad peaks, indicative of a fine-grain polycrystalline nature[38]. Most films display a preferred orientation of polycrystals, but interpretation of XRD spectra is difficult for films having microstructured features. The Ti and Cr films were expected to show a polycrystalline nature, which was confirmed by the diffraction spectra. Transmission Electron Microscopy can provide the same information as XRD, but will also additionally enable the grain size and structure to be imaged. Unfortunately, the grain size has been found to depend on the deposition technique, so different methods of

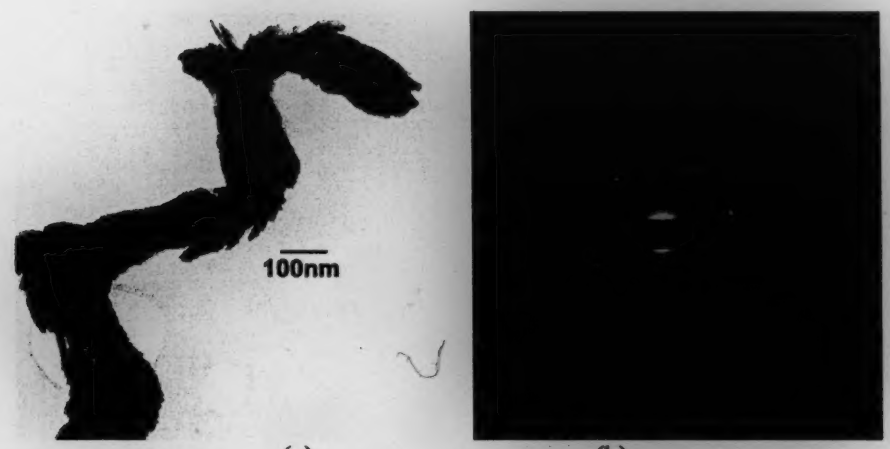

Figure 3.13: Bright field TEM image (a) and diffraction pattern (b) of a Cr microspring from the film pictured in Figure 3.4.

growing a film of the same material can produce varying grain sizes. Generally, zigzag films have been observed by B. Djurfors to have the largest grain size, followed by helices and then posts. Other TEM observations by M. Malac have shown that for Si helices, a large number of individual fiber-like grains growing tightly together make up a single microspring[39,40].

3.6.3 Humidity Sensing

An interesting effect was observed when measuring the capacitance across the microspring films using the deposited electrode layers to investigate the effects of a change in electrode spacing (due to deflection of the microsprings). A change in capacitance was observed when the film was breathed on, leading to the discovery that relative humidity (RH) sensing could be achieved with these films. This led the way to further research with A. Huizinga and A. Wu on the development of a capacitive humidity sensor[41,42]. It was revealed that the porous nature of the microspring films enabled water moisture to penetrate the pores between the microstructures due to the capillary effect[43]. Response times of less than three seconds were obtained, with changes

in capacitance observed over five orders of magnitude. Further exploration into the optimization of the microstructures and deposition parameters was recently performed by K. Harris who was able to reduce the response time approximately 100 ms[44]. This was significantly better than what can be achieved with current commercial humidity sensing devices, and work in this are continues to be studied by other research groups[45,46,47].

3.6.4 Substrate Temperature Considerations

The deposition process itself can often have a big impact on the substrate and the film growing on it. A considerable amount of energy impinges on the substrate surface, and depending on the coating process used, different sources of energy work on the substrate[48]. These include sources of radiative energy, such as heat radiation from evaporator boats or crucibles, electron radiation from reflected electrons during e-beam evaporation, and electron-, ion- and UV-radiation from plasma during sputtering or plasma enhanced processes. The heat of condensation and fusion are other sources of energy that affect substrate properties. Kinetic energy of the material impacting the surface, specifically during sputtering, can also result in considerable changes to the film.

Columnar thickening in the microstructures can be observed in most GLAD films. This can be seen in SEM images where columns begin as slender rods near the substrate, and eventually broaden as the film thickness increases.

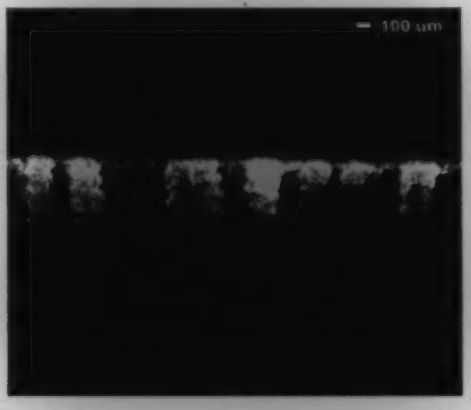

Figure 3.14: A SiO film showing significant columnar broadening.

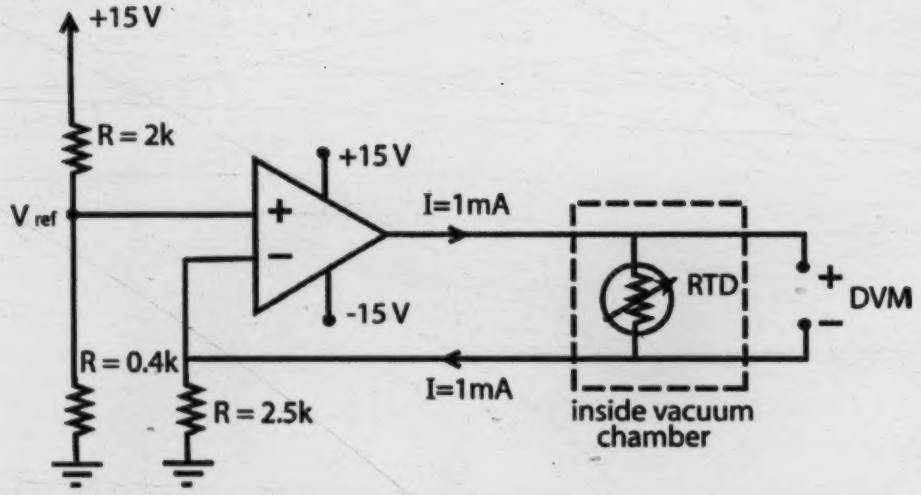

Figure 3.15: An RTD circuit employing a 4 wire configuration utilizing a current source to allow the voltage across the device to be measured and converted to temperature.

A reduction of this broadening would yield more uniform microstructures, and therefore stemmed a study into temperature increases at the substrate. It was speculated that increased substrate temperatures could be caused by the energetics of the impinging flux and result in increased adatom mobility, therefore causing features to expand and broaden[49].

A set of experiments to study the amount of heating that a substrate undergoes during a typical deposition was carried out. Resistance temperature devices[50] (RTD's) were bonded to Si substrates with Tra-Bond 2151 thermally conductive epoxy[51] to monitor the temperature at the substrate during a deposition. The RTD's contained a temperature sensitive Platinum (Pt) layer whose resistance changed with temperature. The Tra-Bond epoxy had a thermal conductivity of 0.95 W/m/K and complied with the requirements of NASA's Outgassing Specification (necessary to achieve the required pressures inside a vacuum chamber). Once the epoxy was cured, a substrate bonded with a RTD was placed inside the chamber onto the substrate chuck and inclined at 85°. It was held

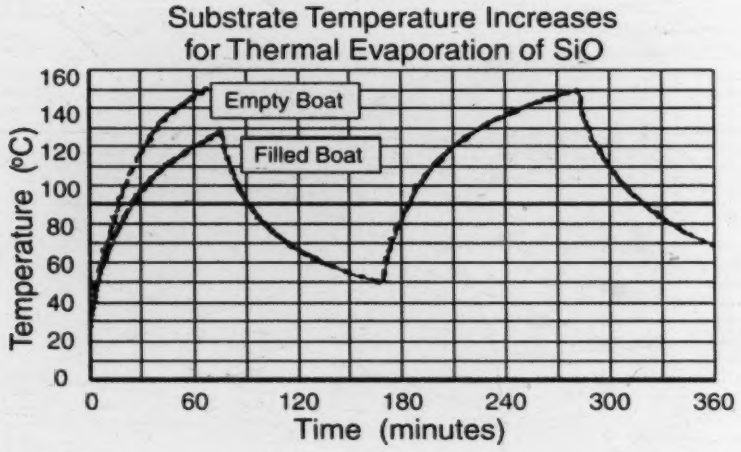

Figure 3.16: Temperature vs. time plot for an 85° deposition of SiO inside a thermal evaporation chamber.

stationary during the deposition to keep the leads from the RTD (in a 4 wire configuration) to the exterior of the chamber from winding around the chuck and becoming detached. The following circuit was built to provide a current source that provided a small current of 1 mA across two of the leads while measuring the voltage across the other 2 wires with a voltmeter. This voltage could then be converted to a temperature according to the conversion factor from the RTD specification sheets.

Depositions were performed with heating from an empty boat, and also with a boat filled with SiO that deposited onto the RTD/substrate combination. The RTD was also allowed to cool inside the chamber before heating the boat again, and allowed temperature versus time plots to be taken.

The substrate temperature did not increase significantly, only reaching a temperature of approximately 150 °C after a 90 minute deposition. This amount of temperature increase is relatively small for the materials used in these experiments, having melting points of 1702 to 1975 °C (for SiO and ZnO, respectively), and as such, it is not believed that unintentional substrate heating plays a major role in microstructure evolution. Equation (2.1) from Chapter 2 shows that the diffusion coefficient is dependent on

temperature, but an increase in temperature will not increase the rates of processes with different activation energies by the same amount. Local variations in surface features (such as defects, steps, and pits) cause variations in the activation barriers that the adatoms must overcome, and hence a simple temperature increase will not preserve the system dynamics at the base temperature or allow for interactions between the adatoms themselves to be accounted for[52,53]. Instead, aspects of the incident distribution, shadowing, and columnar competition are more likely suspects for the cause of column broadening.

To confirm that the heating at the substrate was a minor issue, a thermal analysis of the heating in a 1D approximation gave a sense of the temperature increase for the evaporation of SiO onto a 3-inch Si wafer. For the deposition of any film, a minimum thermal input is given to the substrate, namely, the heat of condensation of the adatoms and any kinetic energy that they may have. As a result, the substrate temperature will increase, but be limited by its ability to transfer heat to other surfaces. Unless special efforts are made to facilitate heat transfer by some means other than radiation, increased substrate temperatures can result, even in the complete absence of intentional heating.

According to the heat power balance equation given below, the net thermal energy per unit area per unit time (in W/cm^2) retained by a substrate is dependent on the incident power flux and the heat loss to other surfaces inside the chamber[48].

$$\rho c d\left(\frac{dT}{dt}\right) = P - L \qquad (3.4)$$

where ρ, c, d and dT/dt are the substrate density (2.3 g/cm^3 for Si), heat capacity (0.7 J/g°C), thickness (0.050 cm) and rate of temperature increase. The incident power flux (P) includes the heat of condensation ΔH_c (eV/atom), the average kinetic energy of the incident atoms, and the plasma heating (E_p) from bombarding neutral atoms and electrons. The flux P has little or no effect on substrate temperature increase for evaporation, since the kinetic energy of the evaporated atoms is extremely low at ~0.1 eV. If sputtering was the deposition method, one would have to consider the elements in P listed above to give:

$$P = \frac{r(\Delta H_c + E_k + E_p)}{\Omega} \qquad (3.5)$$

where r is the deposition rate and Ω is the condensate atomic volume in cm^3/atom.

In this case however, radiant energy from the evaporation boat (which climbs to at least the melting temperature of SiO, 1702 °C) would instead account for substrate temperature increases. The amount of energy emitted is dependent on the temperature of the matter and can be determined from the Stefan-Boltzmann equation[54].

$$E = \varepsilon\sigma T^4 \qquad (3.6)$$

where E is the total energy emitted from a unit area of a surface per second (radiative

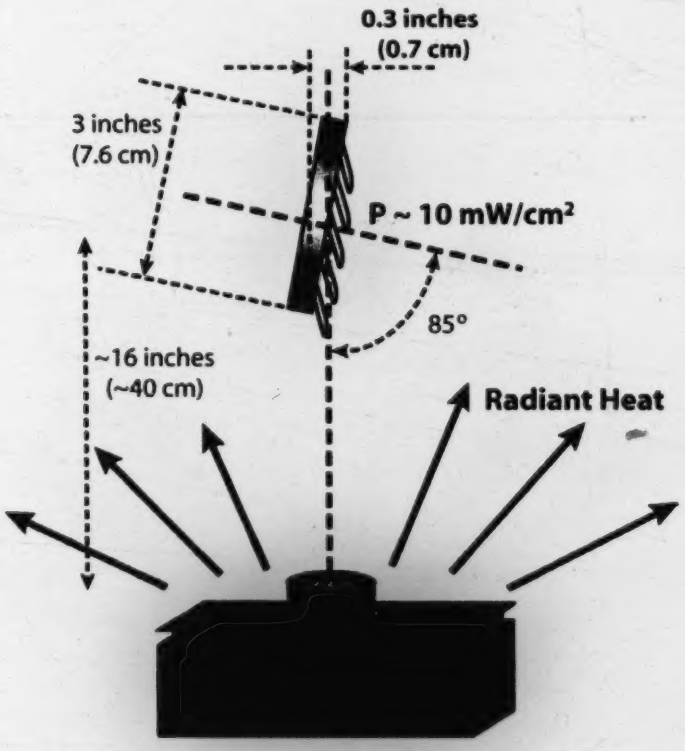

Figure 3.17: For evaporated films, radiative heat transfer can be a cause of increased substrate temperatures.

heat flux), ε is the emissivity, σ is the Stefan-Boltzmann constant = 5.67×10^{-12} W/cm^2/K, and T is the absolute temperature of the surface. For a blackbody, the emissivity of the energy is unity (making it a perfect emitter), but in reality, most objects will only absorb and emit a fraction of radiation. An evaporation boat at 1975 K (1702 °C) would radiate approximately E~65 W/cm^2, assuming an emissivity of 0.8. Only a small portion of this energy will actually be absorbed by the substrate, since it is positioned at a highly oblique angle, giving a lateral spread of only about a centimetre as seen by the boat. A typical heat flux input is more in the range of tens of mW/cm^2 for evaporated films.

The substrate is not isolated however, and it also undergoes heat loss due to conduction with the substrate chuck. For simplicity in the equations to follow, only the radiant energy loss will be considered here, giving:

$$L=\sigma\varepsilon(T^4-T_o^4) \tag{3.7}$$

The emissivity (ε) has been included to take into account the fraction of energy emitted, and T_o is the starting temperature assumed to be room temperature (25°C).

Equation (3.4) can then be written as the following, after separation of variables.

$$\frac{dT}{dt}=\frac{1}{\rho cd}\left[(P+\sigma\varepsilon T_o^4-\sigma\varepsilon T^4\right]\Rightarrow\frac{\rho cd/\sigma\varepsilon}{\left[P/\sigma\varepsilon+T_o^4-T^4\right]}dT=dt \tag{3.8}$$

Integration of the above equation yields:

$$\begin{aligned}t=&\frac{\rho cd(P/\sigma\varepsilon+T_o^4)^{1/4}\sqrt{2}}{8\sigma\varepsilon(P/\sigma\varepsilon+T_o^4)}\ln\left[\frac{T^2+(P/\sigma\varepsilon+T_o^4)^{1/4}T\sqrt{2}+(P/\sigma\varepsilon+T_o^4)^{1/2}}{T^2-(P/\sigma\varepsilon+T_o^4)^{1/4}T\sqrt{2}+(P/\sigma\varepsilon+T_o^4)^{1/2}}\right]+\\&\frac{\rho cd(P/\sigma\varepsilon+T_o^4)^{1/4}\sqrt{2}}{4(P/\sigma\varepsilon+T_o^4)}\arctan\left[\frac{\sqrt{2}T}{(P/\sigma\varepsilon+T_o^4)^{1/4}}+1\right]+\\&\frac{\rho cd(P/\sigma\varepsilon+T_o^4)^{1/4}\sqrt{2}}{4(P/\sigma\varepsilon+T_o^4)}\arctan\left[\frac{\sqrt{2}T}{(P/\sigma\varepsilon+T_o^4)^{1/4}}-1\right]\end{aligned} \tag{3.9}$$

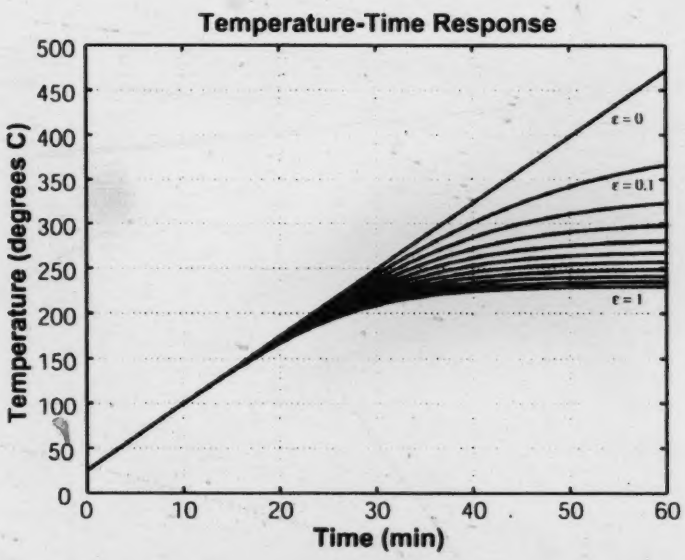

Figure 3.18: Predicted temperature-time response for a substrate under a power flux of 10 mW/cm^2 and neglecting heat loss due to conduction.

which expresses the time it will take for a substrate to reach temperature T starting at T_o. Since the energy flux at the substrate is fairly low for evaporation, a substrate power flux of P ~10 mW/cm^2 was assumed (from a solid angle fraction of 65 W/cm^2), giving the predicted rate of film heating below.

A maximum steady state temperature of approximately 240°C is predicted, which is higher than what was indicated in Figure 3.14. However, the graph above omits heat loss due to conduction, and hence these temperatures would likely be lower and require a longer amount of time to reach a steady state if this were factored into the equations above. Regardless, a good estimate of the maximum substrate temperature was determined, and confirmed that the amount of thermal increase during a deposition is small relative to the melting temperatures of the thin film materials used.

3.7 References

[1] D. L. Smith, Thin Film Deposition: Principles and Practice, New York: McGraw-Hill Inc., 1995.

[2] J. Venables, Introduction to Surface and Thin Film Processes, New York: Cambridge University Press, 2000.

[3] D. Halliday, R. Resnick and J.Walker, Fundamentals of Physics, 4th Ed., New York: John-Wiley and Sons Inc., 1993.

[4] K. Wasa and S. Hayakawa, Handbook of Sputter Deposition Technology, New Jersey: Noyes Publications, 1992.

[5] J. L. Vossen and W. Kern, Thin Film Processes, New York: Academic Press, 1978.

[6] B. N. Chapman, Glow Discharch Processes: Sputtering and Plasma Etching, New York: Wiley and Sons Inc., 1980.

[7] G. N. Jackson, Thin Solid Films **5**, 209 (1970)

[8] K. K. Schuegraf, Handbook of Thin-Film Deposition Processes and Techniques, New Jersey: Noyes Publications, 1988.

[9] J. C. Sit, D. Vick, K. Robbie and M. J. Brett, Journal of Materials Research **14**(4), 1197 (1999).

[10] W. D. Westwood, Progress in Surface Science **7**, 71 (1976).

[11] R. D. Mathis Company technical publication, Silicon Monoxide: Properties and Evaporation Techniques.

[12] B. Halg, IEEE Micro Electro Mechanical Systems Workshop, Napa Valley, CA, 1990.

[13] A. Wolfenden, Dynamic Elastic Modulus Measurements in Materials, Philadelphia: American Society of Testing Materials, 1990.

[14] K. Robbie, J. C. Sit and M. J. Brett, J. Vac. Sci. Technol. B **16**(3), 1115 (1998).

[15] K. Robbie and M. J. Brett, J. Vac. Sci. Technol. A **15**(3), 1460 (1997).

[16] K. Robbie, C. Shafai and M. J. Brett, Journal of Materials Research **14**(7), 3158 (1999).

[17] M. Malac, R. F. Egerton, M. J. Brett, and B. Dick, J. Vac. Sci. Technol. B **17**, 2671, (1999).

[18] B. Dick and M. J. Brett, J. Vac. Sci. Tech. B, **19**, no. 5, 1813, (2001).

[19] K. Robbie and M. J. Brett, U.S. Patent No. 5,866,204.

[20] B. Dick, J. C. Sit, M. J. Brett, I. M. N. Votte and C. W. M Bastiaansen, NanoLetters, **1**(2), 71 (2001).

[21] B. Dick, M. J. Brett, T. J. Smy, M. R. Freeman, M. Malac and R. F. Egerton, J. Vac. Sci. Technol. A, **18**(4), 1838 (2000).

[22] S. R. Kennedy, M. J. Brett, O. Toader and S. John, NanoLetters, **2**(1), 59 (2002).

[23] S. Zankovych, T. Hoffmann, J. Seekamp, J. U. Bruch and C. M. Sotomayor Torres, Nanotechnology, **12**, 91 (2001).

[24] M. O. Jensen, S. R. Kennedy and M. J. Brett, MRS Proceedings: Functional Nanostructured Materials Through Multiscale Assembly and Novel Patterning Techniques, **728**, S9.10 (2002).

[25] W. G. Cady, Piezoelectricity: An Introduction to the Theory and Application of Electromechanical Phenomena in Crystals, 2nd Ed., New York: Dover Publications, 1964.

[26] R. E. Setterington, Piezoelectric Ceramics, 2nd Ed., London: Mullard, 1974.

[27] J. W. Waanders, Piezoelectric Ceramics: Properties and Applications, Eindhoven, NE: APC International Ltd., 1991.

[28] W. P. Mason, Piezoelectric Crystals and their Application to Ultrasonics, New York: Van Nostrand, 1950.

[29] S. Tuzemen, G. Xiong, J. Wilkinson, B. Mischuck, K. B. Ucer and R. T. Williams, Physica B Condensed Matter, **308-310**, 1197 (2001).

[30] M. List, U. Krause, T. Wunsche, Proceedings of the Annual Technical Conference of Vacuum Coaters, 44th Proceeding, Philadelphia, PA, 246 (2001).

[31] B. Dick, M. J. Brett, T. Smy, M. Belov and M. R. Freeman, J. Vac. Sci. Technol. B **19**(5), 1813 (2001).

[32] L. Chen, D. B. Chisley, G. K. Hubler, Pulsed Laser Deposition of Thin Films, New York: Wiley, 1994.

[33] C. S. Yuan, C. T. Yi and W. Walter, Journal of Crystal Growth, **257**(3-4), 280 (2003).

[34] A. K. Chu, C. H. Chao, F. Z. Lee and H. L. Huang, Thin Solid Films, **429**(1-2), 1 (2003).

[35] K. H. Guenther, Appl. Opt., **20**, 1034 (1984).

[36] J. W. Patten, Thin Silid Films, **63**, 121 (1979).

[37] M. J. Brett, R. N. Tait, S. K. Dew, S. Kamasz and A. H. Labun, J. Mater. Sci.: Mater. Electron, **3**, 64 (1992).

[38] B. D. Cullity, Elements of X-Ray Diffraction, 3rd Ed., Upper Saddle River: Prentice Hall, 2001.

[39] M. Malac and R. F. Egerton, J. Vac. Sci. Technol. A, **19**, 158 (2001).

[40] M. Malac and R. F. Egerton, Nanotechnology, **12**, 11 (2001).

[41] A. T. Wu, M. Seto and M. J. Brett, Sensors and Materials, **11**(8), 493 (1999).

[42] A. T. Wu and M. J. Brett, Sens. Mater. **13**, 399 (2001).

[43] L. H. Cohan, J. Amer. Chem. Soc., **60**, 433 (1938).

[44] K. D. Harris, A. Huizinga and M. J. Brett, Electrochem. Solid-State Lett., **5**(11), P. H27 (2002).

[45] W. Qu, J.-U, Sensors and Actuators B, **32**, 57 (1996).

[46] S. C. Thomas, X. Ren, P. Zelenay and S. Gottesfed, Proc. F the 2nd Int'l Symp. On Proton Conducting Membrane Fuel Cells II, Electrochemical Society, Pennington, NJ), 327 (1999).

[47] G. Q. Li, P. T. Lai, M. Q. Huang, S. H. Zeng, B. Li and Y. C. Cheng, J. App. Phys., **87**, 8716 (2000).

[48] M. Ohring, The Materials Science of Thin Films, Boston: Academic Press, 1992.

[49] F. Liu, M. T. Umlor, L. Shen, J. Weston, W. Eads, J. A. Barnard and G. J. Mankey, J. Appl. Phys., **85**, 5486 (1999).

[50] Thin Film RTD Element and Thin Film Detector Flat RTD Element (F Series, and WS81), Omega Engineering Inc.

[51] Tra-Bond 2151 Thermally conductive epoxy, Tra-Con Inc., http://www.tra-con.com.

[52] H. Yang, V. P. LaBella, D. W. Bullock, Z. Ding, J. B. Smathers and P. M. Thibado, Journal of Crystal Growth, **201, 202**, 88 (1999).

[53] Y. W. Mo, J. Kleiner, M. B. Webb and M. G. Lagally, Physical Review Letters, **66**(15), 1998 (1991).

[54] D.R. Linde (Editor), CRC Handbook of Chemistry and Physics, 77th Edition, CRC Press, 1996.

CHAPTER 4
MAIN RESULTS – MECHANICAL CHARACTERIZATION OF MICROSPRINGS AND MICROCANTILEVERS

4.1 Introduction

Micromachined cantilevers and resonators are standard elements in many microelectromechanical system (MEMS) sensors and devices. The study of their properties and methods of construction is a subject of interest, as increasing usage of these components continues. Therefore, theoretical examinations of spring behavior in structurally chiral media[1,2] and cantilever principles[3,4] have been performed and provide motivation for work in numerous MEMS domains[5,6,7]. Using a nanoindentation[8,9] procedure, the mechanical behavior of the unique microspring and microcantilever structures produced by the GLAD technique was studied to better pilot the future possibility of developing devices utilizing these films in potential resonator and MEMS applications. The theory for macroscopic spring and cantilever analysis is introduced and experimental results of the nanoindentation experiments are given, evaluating their agreement with theoretical principles.

4.2 Theoretical Springs

4.2.1 Spring Constants

The axial force constant of helical compression springs is dependent on many geometrical properties. By either varying the dimensions of the spring or by changing the material that it is fabricated from, the resulting mechanical properties of the spring can be altered. For a spring with circular cross section, Equation (4.1) describes its axial spring constant[10,11,12], for compression in a direction parallel to its axis. This formula was first developed by Ancker and Goodier in 1958 when studying tension and torsion in helical springs[13,14,15].

$$k = \frac{P}{f} = \frac{Gd^4}{64R^3 n}\left[\frac{3d^2}{64R^2} + \frac{(3+\nu)}{2(1+\nu)}\tan^2(\alpha)\right]^{-1} \quad (4.1)$$

where: k = axial spring constant (N/m)
f = total shortening (m)
P = load (N)
R = coil radius (m)
d = wire diameter (m)
n = number of turns
G = Shear Modulus (Pa) = Young's Modulus/[2(1+ν)]
ν = Poisson's Ratio
α = pitch angle of spring = $\tan^{-1}$[h/(n 2 π R)] where h = height of the spring

It should be noted that the measurement of R and d are determined from SEM images of the microsprings. Through the form of Equation (4.1), a slight uncertainty in R and d can lead to substantial uncertainty in calculating k and related parameters.

When the entire film is envisioned, it can be seen as a collection of springs standing on end in close proximity on the wafer. Therefore when considering an area of the film, it needs to be understood that a large number of the microsprings are affected, necessitating the consideration of the effect of all the microsprings acting together. They would be alike springs connected in parallel, where the sum of the spring constants for each individual spring is added together to obtain the overall spring constant for the system[16]. For *i* springs, the total spring constant would be:

$$k_{tot} = k_1 + k_2 + \ldots k_3 = \sum_{n=1}^{i} k_n \quad (4.2)$$

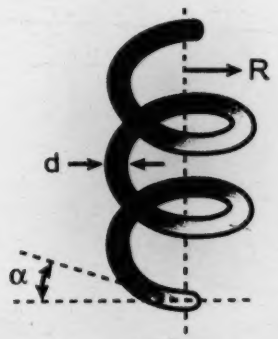

Figure 4.1: Schematic diagram of a spring illustrating geometrical parameters.

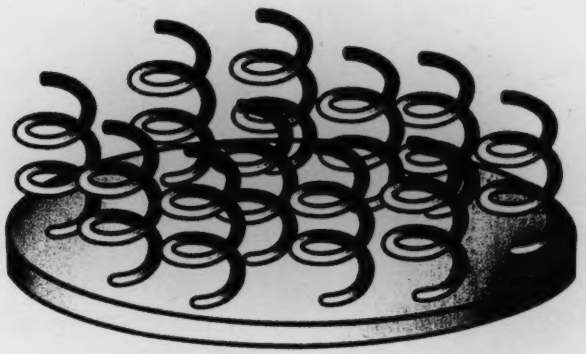

Figure 4.2: Schematic illustration of a microspring thin film.

Assuming that the spring constant of each individual spring was the same (i.e. $k = k_n$), then $k_{tot} = i\,k$, where i is the total number of springs connected in parallel. The total force required to squeeze the system of springs can then be considered by Equation (4.3), noting that the amount of force required to squeeze the springs increases with the number of springs affected.

$$F = i\,k\,\Delta x \tag{4.3}$$

Springs, however, are not constrained to being squeezed only in an axial direction, and can move in a lateral direction as well. For springs bending laterally, a lateral spring constant is instead considered, which involves the determination of the spring's bending moment[17,18]. Lateral bending of a spring can be visualized as if the spring was swinging from side to side while being held at its base.

$$k_L = \frac{M}{\phi} = \frac{2}{2+\nu}\left[\frac{Gd^4}{128nR}\right] \tag{4.4}$$

where: k_L = lateral spring constant
M = Moment
ϕ = bending angle (degrees)
G = Shear Modulus (Pa), and the rest of the parameters are as given previously.

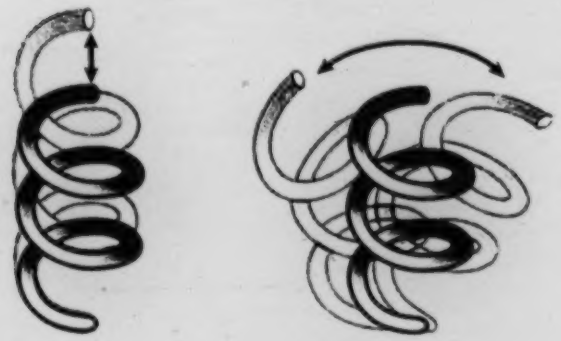

Figure 4.3: Axial compression for the spring at left and lateral bending for the spring at right.

4.2.2 Vibrational Frequencies

When considering elastic springs, it becomes natural to contemplate their actuation, and the frequencies that they vibrate at. More on thin film microspring frequencies is discussed in the following chapter. The axial vibrational frequency of a spring can be determined if the axial spring constant, k, is known[19].

$$f = \frac{1}{2\pi} * \sqrt{\frac{k}{M + m/3}} \qquad (4.5)$$

where M = mass of an attached weight (kg) (equals zero for uncapped films) and m = mass of the spring (kg).

Similarly, the lateral vibration frequency of a spring can be determined from its lateral spring constant, and requires a determination of the spring's mass moment of inertia[17].

$$f_L = \frac{1}{2\pi} * \sqrt{\frac{k_L}{I}} \qquad (4.6)$$

where I is the mass moment of inertia calculated by integrating the volume of the spring such that $I = r^2 \rho V$, where ρ is the density of the spring. Since the resonant frequencies of a spring are dependent on their spring constants, it should be noted that the frequency is likewise affected by geometrical and materials properties.

4.3 Cantilever Theory

For an inclined cantilever beam with rectangular cross section, the displacement, Δx, in the vertical direction is determined by adding a $\cos^2(\alpha)$ factor to the typical cantilever displacement formula[20]. This added factor is necessary since the applied force and displacement are perpendicular to the plane of the substrate, and not perpendicular to the cantilever plane. A simple rectangular cross-section best approximated the cross-section of actual microcantilever beams that were grown.

$$\Delta x = \frac{FL^3 \cos^2(\alpha)}{3EI} \tag{4.7}$$

where: Δx is the displacement perpendicular to the substrate plane
F is the applied force
L is the cantilever length
α is the rise angle
E is Young's modulus
I is the moment of inertia (for a rectangular cross-section, $I = wt^3/12$, where w is the width and t is the thickness).

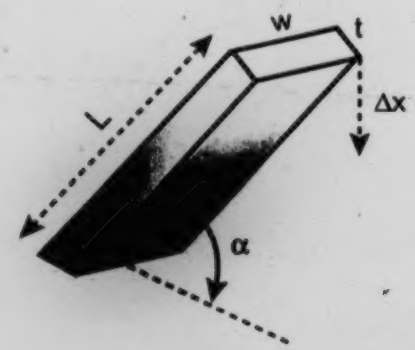

Figure 4.4: Schematic diagram of a cantilever illustrating geometrical parameters.

4.4 Nanoindentation

A nanoindentation technique[21] was used to demonstrate the mechanical response of the microstructured thin films. Hysitron's Triboscope[22] was used in conjunction with

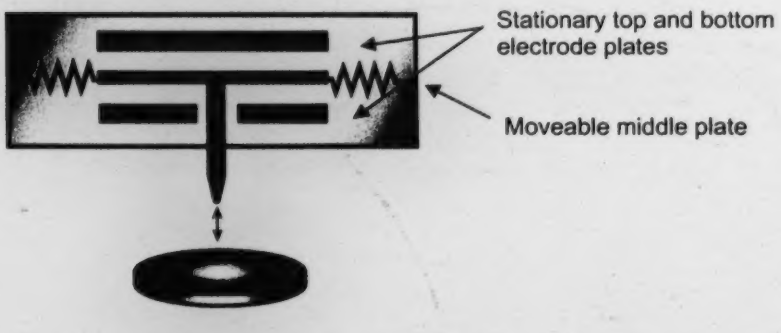

Figure 4.5: Internal schematic of the Hysitron Trioboscope transducer.

Digital Instrument's Dimension 3100 Atomic Force Microscope[23], which allowed quantitative depth sensing and *in-situ* imaging of indentation sites. This testing approach provided a method to study the materials characteristics and nanomechanical properties of the films, and enabled the motion of the nanoindenter tip to be accurately monitored while applying desired amounts of force to the specimens. This produced force versus displacement plots that revealed the unique nature of the films being tested. In order to apply a controlled, variable force to a sample, a parallel plate geometry sandwiching a plate held by leaf springs between two rigid, parallel plates is used in the Triboscope transducer. A diamond indenter tip attached to a shaft is mounted to the middle plate and goes through a small hole in the centre of the lowest plate as shown in the figure below. A force can then be generated by applying a voltage between the middle and bottom plates through electrostatic actuation. The displacement is measured by a change in capacitance between the middle and the outer plates.

After an indentation was performed, an image of the surface (or deformation, if there was one) resulting from the test could be obtained immediately by scanning the surface using the AFM. This eliminated the need to reposition the imaging instrument over the testing site. The force and displacement results that were acquired during the tests, in conjunction with the *in-situ* images, offered a great deal of information concerning the mechanical properties of the samples tested, and allowed the repeatability necessary for meaningful results in nanoscale testing.

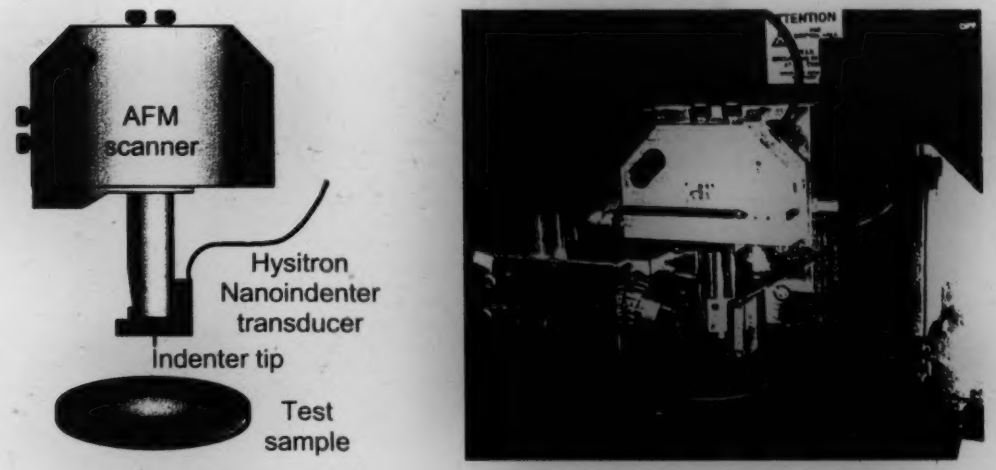

Figure 4.6: Images of the Triboscope Nanoindenter and Atomic Force Microscope.

During a continuous depth measuring nanoindentation test, a probe is pushed into a sample with a known force. As the probe is pushed in, the depth is monitored, and plotting the force as a function of depth results in a curve similar to that shown in Figure 4.7. This curve exhibits nonlinear loading and unloading curves, and has characteristics that depend on the shape of the indenter tip. Various types of indenter tip shapes exist

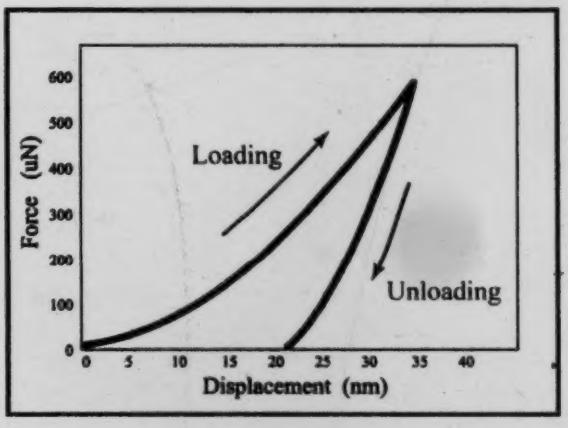

Figure 4.7: A typical force displacement curve for a spherical indenter.

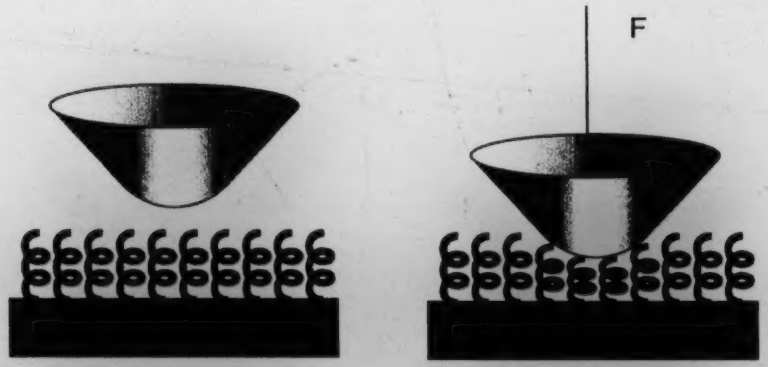

Figure 4.8: Schematic illustration of a cono-spherical nanoindentation tip displacing a microspring film.

and this plot shows a curve typical for a cono-spherical indenter (a cone whose apex is a sphere with a desired radius of curvature). The nonlinearity arises from the increasing area of contact that the tip makes with the surface as it is pushed deeper into the sample. Unless the sample deformation is purely elastic, the unloading curve will not follow the exact path of the loading curve and will instead cross the x-axis at some point. These force-displacement curves are an indication of the sample's unique materials characteristics since the response to an applied force will cause different types of reactions that can be seen in the curves.

Force displacement curves represent a mechanical "fingerprint" of the sample being tested, and are unique to each material. Information on the maximum depth, residual depth, and contact stiffness can be extrapolated from these curves. The maximum depth is the deepest that the indenter is pressed into the samples, and contains elastic and plastic components[24]. Residual depth is the amount of impression that is left when the indenter is withdrawn from the sample, and the contact stiffness of the sample is obtained from the initial slope of the unloading curve[25]. This is a commonly employed method to determine sample stiffness (S) when the indenter first begins to unload[26].

$$S = \frac{E_r}{2}\sqrt{\frac{A}{\pi}} \tag{4.8}$$

Figure 4.9: A SEM image of a cono-spherical nanoindenter tip with 1 micron radius of curvature[27].

where E_r = reduced Young's Modulus of the contact (in Pa) and A = contact area of indenter tip (m^2). The reduced Young's Modulus is important when indenting extremely hard samples (where the Modulus of the indenter and sample are comparable), but can simply be taken to be the Young's Modulus when indenting soft samples, which will be the case for the films tested here.

Various sizes and types of indenter tips are readily available such as three-sided pyramidal tips, 90 degree cube corner tips, Berkovich tips, and cono-spherical tips[28]. The latter type was used for the nanoindentation experiments in this dissertation, because they were the most suitable for indentations of soft materials and porous film samples. An indenter tip with a spherical apex would also be unaffected by small angular variations in tilt due to its shape. If the tip became angled slightly during the indentation, the spherically shaped head would prevent any uneven compression of the sample from occurring. This helped to ensure that the same tip contour displaced the films each time. These tips could be chosen with a range of values for the radius of curvature at the tip. One μm and 100 μm radius sizes were selected for the nanoindentations to examine the effect of small and large contact areas.

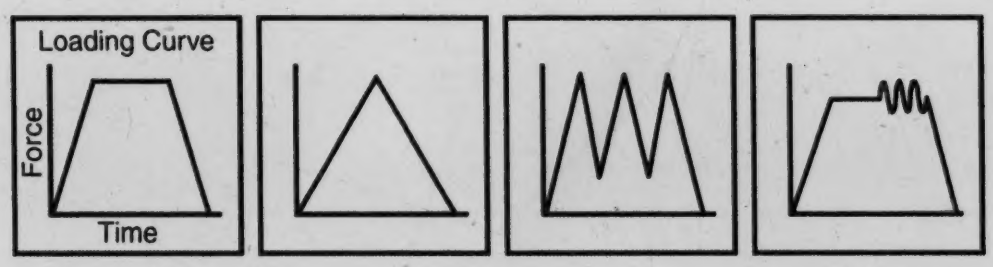

Figure 4.10: Typical force loading curves with (a) load-hold-unload, (b) load-unload, (c), load-partial unload-load-partial unload-load-unload, and (d) load-hold-sinusoidal loading-unload sequences.

4.4.1 Effect of Force Loading Curves

Different types of loading curves can be used to remove certain undesirable effects like creep, drift, or viscoelasticity[29-33]. Creep and drift are indicated when a constant force is applied to the sample and movement of the tip depth is detected, since creep can be defined as a long term change in deformation under a constant load. In some extreme cases, the unloading portion of the displacement curve can show a slight bowing with an initially negative slope, indicating that viscoelastic effects are dominant during the unloading[34-37]. By varying the loading and unloading velocities, or by applying "hold" or constant forces for a period of time, these effects can be minimized or removed[38,39]. Other kinds of force approaches include partial loading and unloading stages and sinusoidally applied forces.

4.5 Nanoindentation of Standard Films and Substrates

Nanoindentations of some standard films were performed to observe displacement curve characteristics. The materials that were tested included fused quartz, polished Al, silicon and glass substrates, dense SiO films, and a polymeric material that was used for seeding layers in periodic films. The indentations of these materials showed some typical

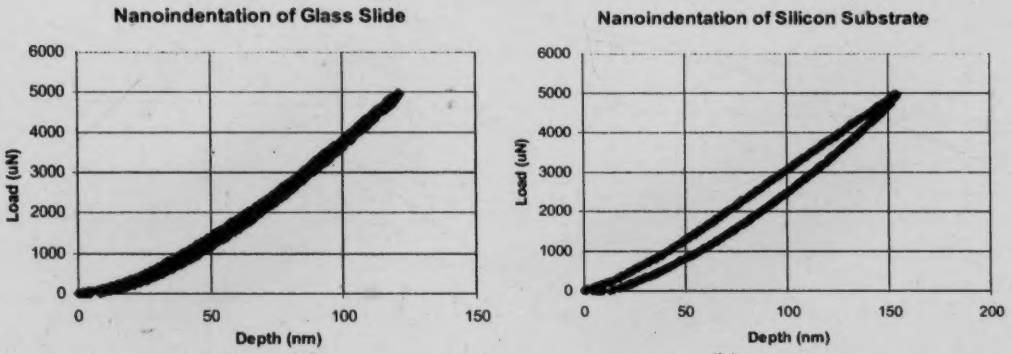

(a) (b)

Figure 4.11: Nanoindentation curves of a glass slide in (a), a silicon substrate in (b).

types of responses expected for these materials, and indicated that their stiffnesses (with the exception of the polymeric film) were all much higher than that which could be expected from the microstructured films. This ensured that microstructure properties of the films were being measured instead of that of the substrates. The effects that the pressed plastic material could have had on nanoindentations of films grown onto these substrates is discussed further in Section 4.8.2.

4.6 Nanoindentation of Capped Films

The films that were initially tested were comprised of porous layers surmounted by dense capping layers and resembled "spring bed" structures[40]. The dense capping layer served to prevent the nanoindenter tip from penetrating into the microstructured film and potentially bending springs in a lateral direction. Results of AFM images and force displacement curves indicated that there was an elastic regime to the displacements in the films when low forces were applied[41]. The loading behavior of the porous films was compared to that of dense, unstructured films and revealed a marked difference between the two.

4.6.1 Film Details

The initial films reported here were constructed of SiO and included "springs" of 2600 nm, 1250 nm, and 600 nm helical pitch, with 1, 2, and 4 turns, respectively

(samples 1, 2, and 3). Each of these films were approximately equal in height (~3 μm) and column thickness (~70 nm), but differed in coil radii (R = 400 nm, 250 nm, and 125 nm for samples 1, 2, and 3 respectively). Cross-sectional images of these films showed a spacing of approximately 100 nm between helices. Capping layers of SiO (~400 nm in thickness) ensured that after the nanoindenter came into contact with the film, the application of further force would not cause the tip to slip between the columnar microstructures, but rather compress the film.

4.6.2 Nanoindentation Details

A cono-spherical indenter with a diamond tip having a rounded spherical apex with a 1 μm radius of curvature was utilized for these nanoindentations. A larger tip with a 100 μm radius of curvature was later used on some of the films to provide a larger area of contact. Before each indentation was made, the area of interest was imaged to ensure that the surface was free of any defects or debris. Several indentations were then made in the films, with some performed successively at the same site to observe how the film would respond to such a manner of treatment.

Using various loading curves and amounts of force ranging from 30 μN to 1000 μN, the tip was pushed into the sample while recording the depth it entered to generate a set of force versus displacement curves. A typical loading cycle involved the force being gradually ramped up, held at the desired maximum force, and then released. In addition to these simple load-hold-unload sequences, a number of more complicated cycles were used, including several loading and partial unloading sequences and sinusoidally applied force at several frequencies up to 50 Hz. Since this was the maximum frequency that the instrument was capable of, the tip could not be coupled with the film and oscillated at the higher frequencies where mechanical resonance was expected[35].

4.6.3 Force Displacement Results For Capped Film Nanoindentations

Displacement curves from the SiO film containing helices with single turns of 2600 nm pitch are shown in Figure 4.12, along with the loading curves applied to generate them. A simple load-hold-unload loading curve with a maximum applied force of 30 μN

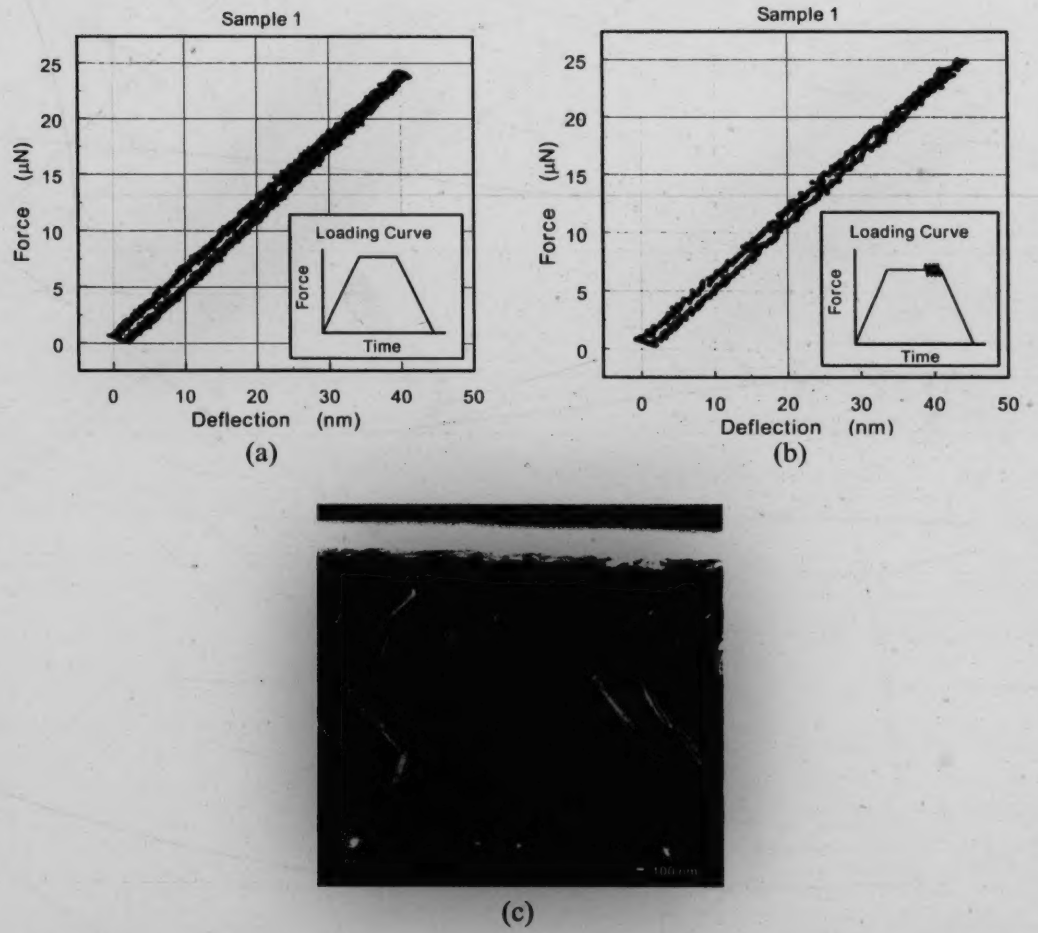

Figure 4.12: Force versus displacement nanoindentation results for capped microspring films. For the SiO film pictured in (c), two different loading curves (shown inset) were used to generate the displacement curves in (a) and (b).

was first employed. Approximately 5 μN of force was absorbed by the compliant spring attached to the base of the indenter tip, leaving the remaining amount of force to be applied to the film. The same loading curve was applied again at the same site, this time with the addition of the sinusoid shown in the loading curve. The frequency of the sinusoid was 10 Hz with a peak-to-peak amplitude that was 10% (3 μN) of the maximum applied force (30 μN). Both of the resulting displacement curves are very linear and

strikingly similar, despite the slight variation in the loading curves and the fact that both displacement curves were obtained from indentations made by consecutive measurements at the same location on the film. The curves appear to be fairly linear, and indicate that the film structures were likely compressing the film uniformly due to the capping layer. Since there is not much hysteresis in the curves (unloading curve closely follows the loading curve), the films' behavior was elastic in this regime. Other force versus displacement curves obtained from the testing of other films produced similar data that illustrated this same type of film behavior and demonstrated the repeatability of displacements made in these films.

4.6.4 Effect of High and Low forces

When larger forces in the hundreds of μN were applied, the indentations were no longer purely elastic; the films suffered plastic deformation and AFM scans showed that they retained impressions of the nanoindenter tip. The tension produced in the capping layers at these higher forces would have also affected the displacement curves when the cap itself began to displace and conform around the shape of the tip. Extremely high forces near 1 mN were also applied, invariably breaking and damaging the films. SEM pictures of these indentation sites revealed the interesting manner in which the capping layer fractured in two circular breaks. The first (inner) fracture took place when the tip had become displaced approximately 520 nm, as indicated by the first plateau in the displacement curve of Figure 4.13. The circular piece that broke away had conformed around the tip of the indenter making it concave in shape. As the indenter continued to push deeper into the film, evidence that the film was becoming stiffer was apparent with the steeper gradient in the slope of the displacement curve. When the film became deflected approximately 915 nm, the capping layer fractured a second time to create the annulus shaped segment, and this produced the second plateau in the displacement curve, after which the slope became steeper yet. The slope would have likely begun to resemble that of dense SiO (shown by the dashed line) if the tip had been allowed to continue compressing the film further. A scaled representation of the nanoindenter tip and the depths it penetrated when each of the fractures occurred is shown in Figure 4.13

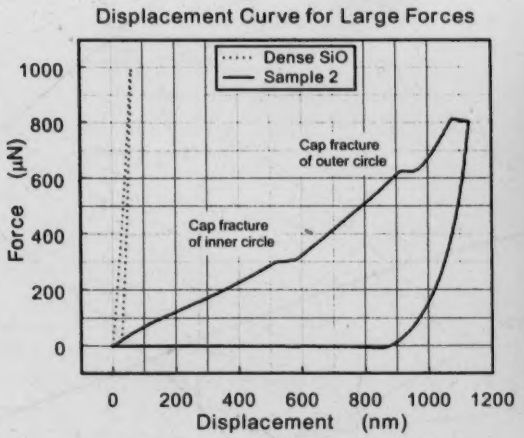

(a)

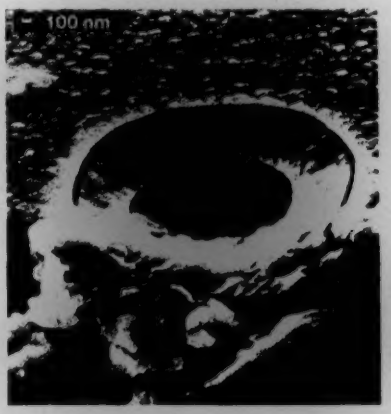

(b)

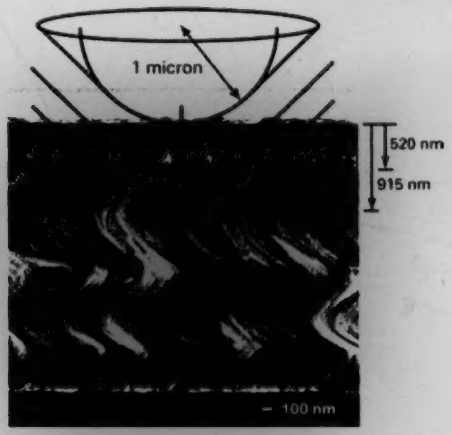

(c)

Figure 4.13: Effects of indentations made with large forces. The displacement curve in (a) was generated from indentations made in the SiO film shown below in the two SEM pictures. High force indentations caused the capping layer to fracture twice as shown in (b), and an overlay of the nanoindenter tip in (c) shows the depth it penetrated into film when each of the fractures occurred.

A standard, dense, 5 μm thick SiO film (without any helical structure) was tested as a control. Several indentations made in this film revealed that the forces required for very small displacements were much greater than those required for the same amount of

deflection in the microspring films. The application of 50 μN of force to the dense SiO film caused a displacement of only 4 nm, whereas the application of 50 μN of force to a microspring film caused a deflection of approximately 80 nm. These results further confirm that the structured films were more compliant than a dense film, due to compression of the microsprings. The Young's modulus for the dense SiO was provided by the Triboscope® and matched a published value of 92 GPa for SiO thin films[19].

4.6.5 Comparison Between Experimental and Theoretical Data

Results from indentations taken with the 100 μm radius of curvature tip were used to calculate spring constant values. The larger tip provided a more even and planar surface with which the films were compressed. In estimating the spring constants, it was assumed that the nanoindenter tip was a flat circular area which pressed into the film. The observed linearity of the displacement curves suggests that this is a reasonable approximation. Nominal contact areas were provided by the nanoindenter, which made use of the radius of the probe tip and the displacement to calculate the contact areas at the point of maximum compression[42,43]. The values obtained in this manner differed from the true, effective tip area due to the presence of the stiff capping layer, which likely redistributed the load laterally, thus compressing more springs than anticipated. This would make experimental contact stiffnesses higher than those predicted theoretically. The results of these calculations are summarized in Table 4.1 where corresponding values from the dense SiO films are included for comparison.

Table 4.1: Comparison of experimental and theoretical results for helical and dense SiO films with capping layers taken from a spherical 100 μm radius of curvature tip.

Thin Film Sample (# turns)	*Contact Stiffness* (μN/nm)	*Contact Area* (μm^2)	*Experimental Contact Stiffness per Area* (μN/nm)/(μm^2)	*Nominal Theoretical Spring Constant per Area* (μN/nm)/(μm^2)
1 turn	0.59	3.5	0.17	0.01 ± 55%
2 turns	0.88	2.8	0.32	0.03 ± 55%
4 turns	1.1	1.1	1.10	0.07 ± 55%
Dense film	16	0.023	680	n/a

4.6.6 Discussion of Results

According to the spring constant equation given earlier, the calculated theoretical spring force constants indicated that the helically structured film which would deflect with the most ease was the film with 1-turn helices, followed by the film with 2 turns and finally the film with 4 turns. Experimental spring constant values collected for samples 1, 2, and 3 followed the trend dictated by Equation (4.1), but deviated from theoretical values due to several possible reasons. Since the capping layer had a certain degree of stiffness as mentioned above, it was likely deflecting in such a way to include microsprings extending beyond the determined contact area. More springs were probably being compressed than estimated, making the calculated theoretical values smaller. Interactions between adjacent springs would affect the results obtained for displacement depths that penetrated a considerable percentage of the total film thickness.

The stiffness of the capping layer would also contribute to the mechanical response of the film, having a tension that would act against the force of the indenter, especially at higher forces (akin to a concentrated force applied to a trampoline). The response of this condition is complex however, since unlike a layer simply bound only at the edges, the capping layer rests on a bed of springs, much like a Winkler foundation[44-47], with continual contact between the cap and elastic foundation. Solutions to the governing equation for this situation are not trivial, and hence further test samples excluded the growth of the capping layers.

Another factor responsible for the discrepancy in the spring constant values was the error associated with estimating the dimensions of the microsprings. In particular, the fourth and third order power terms of Equation (4.1) would generate inaccuracies in the results according to standard error propagation formulas[48]. When the spring constant per area was determined, it was necessary to estimate the number of springs that were present per unit area from SEM images, and this would have introduced some statistical variations as well. One consideration needing comprehension regards microscopic materials, and how a disparity between their properties and that of their macroscopic counterparts can exist. The expected behavior of micromechanical devices can differ

from actual behavior, for instance, in the achievement of a certain stiffness or resonant frequency[49].

4.7 Nanoindentation of Uncapped Films

Capping layers were not grown on top of the set of porous films tested next, as it was suspected that these solid layers altered the system response and effective contact area by spreading the nanoindenter tip's load over some unknown extended region.

4.7.1 Experimental Details

A number of SiO thin films were grown onto 3 inch diameter silicon wafers. Each film was approximately 2 μm thick and homogeneous over the entire wafer, with a variation in thickness no greater than 5% between the centre and edge of the wafer, which was confirmed by SEM images. One, two and three turn microsprings with pitches of 1300 nm, 950 nm, and 600 nm, respectively, were grown. Other 3-turn microspring thin films of titanium (Ti) and chromium (Cr) were grown by electron beam evaporation (thickness ~2 μm). A preliminary deposition was performed for the Ti films with shutters (positioned between the source and substrate) closed in order to getter pump the system prior to film growth.

The high porosity of the films suggested that the microsprings acted independently for the amount of deflection that was made by the nanoindenter into the films (typically 60-70 nm). Cross-sectional and plan view SEM images confirmed that the spacing between neighboring springs was large enough to allow low force nanoindentations to be made and ensured that no interaction occurred between adjacent springs. A series of indentations with forces ranging from 20 μN to 1000 μN was then performed using the 100 μm spherical tip, with the low force indentations displacing the film less than 5% of total film thickness.

4.7.2 Nanoindentation Tip Selection

A cylindrical flat punch tip with a foot area of 0.785 mm^2 was used in additional nanoindentations of the films, but due to inhomogeneities in the films at the larger scales

Figure 4.14: SEM image of a SiO microspring film showing nodular defects.

associated with this particular tip, the effect of surface irregularities thwarted the assessment of microstructure properties. These inhomogeneities were due to debris and large particles ejected from the source material during the depositions, leading to nodular defects in the film[50]. This could result in large features (nodules) that were higher than the height of the rest of the film and which could be observed in SEM images. Consequently, the flat punch tip would encounter the raised features first and compress them instead of the film, causing the properties of the debris to be measured instead of those of the film. In retrospect, a smaller contact area that was more comparable with the dimensions of the spherical tip would have made the flat punch tip more appropriate, but due to cost considerations this was not pursued.

One further issue that arose from the use of the flat punch tip dealt with the degree of perpendicularity that the direction of tip approach had to the surface of the sample. If the surface of the tip was not parallel with the surface of the sample, then the film could have become compressed more on one side than the other, due to the tilt that might have been present in the tip. As a result, the usefulness of any data taken would become questionable if the film was not displaced uniformly. The spherical tips precluded any of these problems as explained previously.

4.7.3 Nanoindentation Results for Uncapped Microsprings

Nanoindentation results for the microspring thin films are shown using a spherical 100 μm curvature tip. Low force indentations performed successively at the same site in the microspring films produced the overlapping curves shown in Figure 4.15(a), and indicated that the indentations were reproducible and not destructive to the films.

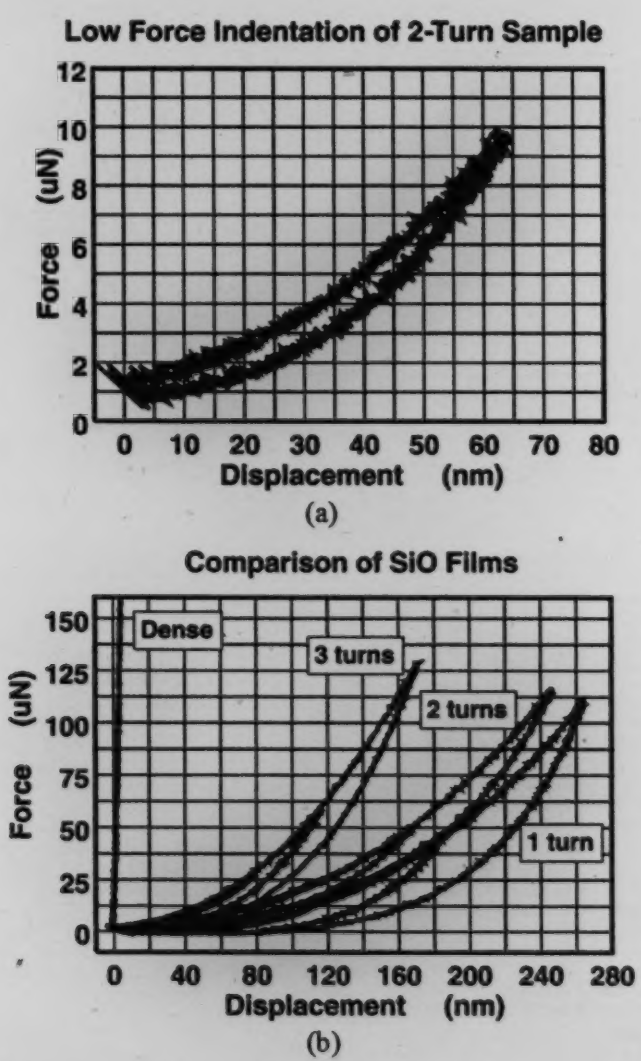

Figure 4.15: Force versus displacement results showing: (a) the results of three low force indentations carried out successively at the same site for a 2-turn microspring and (b) the trend in the curves for various microspring geometries.

The displacement curves in Figure 4.15(b) show a separation between 1-, 2-, and 3-turn microspring films for various applied forces, with film stiffness increasing for higher number of turns. This scaling could be predicted from the macroscopic spring constant given earlier. The reason the plots show some curvature and are not linear is due to the increasing contact area as the tip is displaced deeper in to the sample. These films did not contain capping layers, and hence the effect of the changing contact area can be seen. Detailed SEM images allowed microspring geometries to be evaluated, and an estimated areal number density of approximately 10 microsprings per $(\mu m)^2$ was determined.

The areal number density of microsprings was multiplied by the calculated spring constant to give a theoretical areal stiffness. Experimental contact stiffnesses were determined from the indentations immediately after the point of maximum displacement, when the tip was being withdrawn during the unloading segment of the indentations[26,51,52]. The theoretical areal stiffness was calculated for the same maximum displacement when the contact area was largest. A circular flat contact area was approximated for simplicity, since the large radius of curvature of the indenter tip was significantly greater (~2000X) in comparison to the ~50 nm displacements considered, making this a reasonable assumption. It was originally intended that use of the flat punch tip would eliminate any issues pertaining to spherical contact geometry, but that tip was associated with other experimental difficulties as previously discussed.

4.7.4 Effect of Different Materials

Films of different composition, but with the same microspring geometry, were studied for 3-turn SiO, Ti, and Cr microsprings. These films showed a stiffness that was material dependent and could be resolved from the macroscopic formula. Results in Table 4.2 show that the spring geometry has a definite bearing on the resultant spring constant. The trend given by the numbers is useful for predicting which spring geometries may yield more easily than others, and thus be ultimately useful for assisting in the design of theoretically postulated devices.

Table 4.2: Comparison of experimental and theoretical areal stiffness for various thin film samples.

Thin Film Sample	Experimental Areal Stiffness $(N/m)/(\mu m)^2$	Theoretical Areal Stiffness $(N/m)/(\mu m)^2$
SiO (1 turn)	10.0	27 ± 55%
SiO (2 turns)	11.3	32 ± 55%
SiO (3 turns)	17.8	42 ± 55%
Ti (3 turns)	19.8	47 ± 55%
Cr (3 turns)	21.2	56 ± 55%
SiO (Dense)	18500	N/A

Some discrepancy in the magnitude of the experimental and theoretical areal stiffnesses exists. This was likely due to inaccuracies in determining *exact* microspring dimensions from the SEM images as explained previously and would introduce some error. The axial spring constant relation also assumes a constant column diameter, whereas the actual thin film microsprings exhibit a distinctive shape anisotropy, with the column thickness increasing towards the top of the column[53,54].

Hysteresis could be observed in the nanoindentation results, with the displacement curves resembling nanoindentations done on elastomers or polymeric materials where viscoelastic behavior can be present[55]. This type of relaxation behavior produces a time effect where the material gradually recovers from most or all of the strain after the load is removed. The rate of recovery from the strain can differ from the rate at which the strain was received, and hence the loading and unloading regions in these curves can diverge from each other but still meet back at the origin. Frictional forces or stiction between the nanoindenter tip and the film could also be expected with decreasing scale lengths, making the dominance of surface effects more evident[56]. The hysteresis was unlikely to be due to an artifact resulting from the nanoindentation equipment, since the Triboscope instrument was allowed to run for over an hour to warm up and reach a steady state before testing to prevent any drifting due to thermal effects[57,58]. Drift correction features were also utilized to monitor the z-displacement drift, and enabled the cancellation of any

indentations where a maximum drift rate or drift time was exceeded. Further nanoindentations of other microspring thin films showed this hysteresis, while the dense SiO films did not.

Tip adhesion to the film could also cause this type of hysteresis, as surface humidity of a hydrophilic sample can cause adhesive forces to be greater[59]. This would make the force required to load the film different from that required to unload the tip, making the work of adhesion a visible effect, with the irreversible work shown by the area between the curves[60,61].

4.8 Nanoindentation of Microcantilever Arrays

Nickel (Ni) slanted posts deposited by electron beam evaporation were grown on a polymeric array (see Figure 3.8) that was created using a heated embossing technique[62]. An epoxy resin was imprinted by a master pattern to form an array of raised "seeds" with 2 μm periodicity. These then provided a starting point for individual microstructures to begin their development. The periodic structures were desirable, as films with increased porosity could be fabricated with microstructures that were relatively simple in geometry.

4.8.1 Microcantilever Array Details

Film growth occurred primarily on the raised plastic seeds and not in the areas between them due to shadowing from adjacent seeds when fabricated under oblique incidence angles. An ordered array of microstructures could then be fabricated which followed the periodicity enforced by the seeded substrate[63]. Some material was found in the areas between the artificial nucleation sites, due to the amount of shadowing received from nearby seeds. Depending on how the seeded array was positioned relative to the direction of incoming flux and on what angle of incidence was used for the deposition, the size of shadowed region might not be large enough to prevent small amounts of film growth between the seeds.

The size of the seed elements (approximately 250 nm in diameter) affected the resulting column sizes of the microstructure grown on then, as the typical width of the microcantilevers was found to be approximately 300 to 400 nm. The exact number of

microstructures per $(\mu m)^2$ was easily determined for this film (0.25 posts/$(\mu m)^2$), and allowed theoretical values to be calculated with better accuracy.

4.8.2 Comparison of Experimental and Theoretical Results

Predicted displacements for the microcantilevers corresponded well with experimental displacements. At higher loads, larger calculated displacements were determined in comparison to experimental values. More stress would be placed on the microcantilevers at higher loads, and issues with how it would be distributed along the microcantilever or at the substrate junction (where details of attachment are not well known) were likely.

Indentations on the plastic array itself were performed to determine what effect it had on the indentations of both the film and plastic layer together. The measured stiffness of plastic array was averaged to be 9 N/m per square micron, which was lower than that measured for the film-plastic combination (see table below). Consequently, what occurred during these indentations was a deformation of the plastic first (being less stiff), and then the Ni microcantilevers.

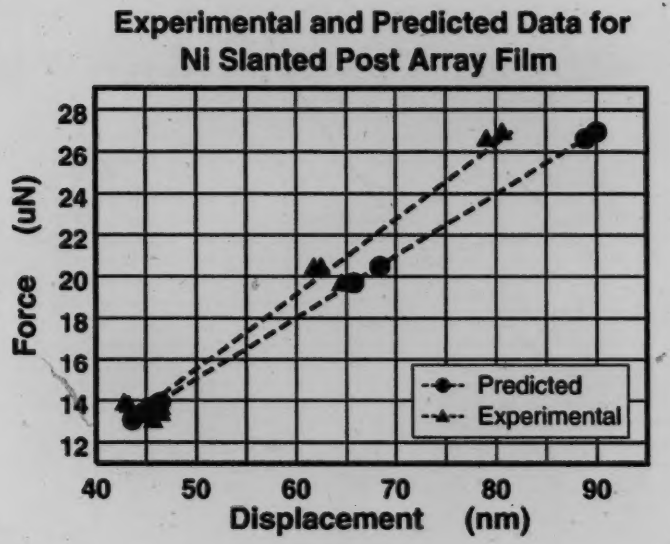

Figure 4.16: Displacements comparisons for the Ni slanted post array.

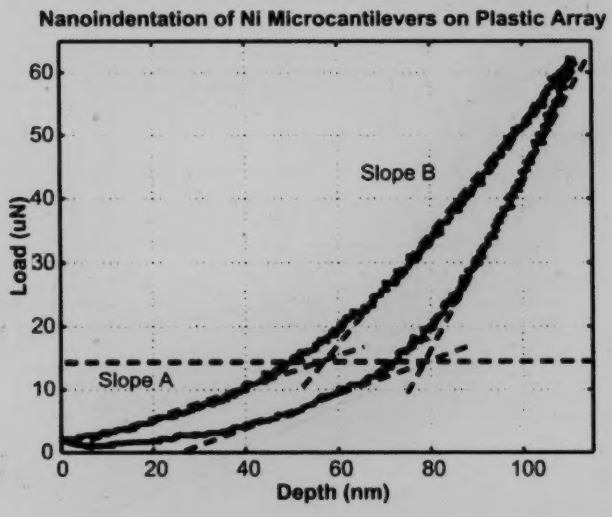

Figure 4.17: Force-displacement curve of Ni microcantilever and plastic seed layer combination.

This was confirmed by the force-displacement curves which showed two distinct slopes in the plot, the first having the lower slope. It should be noted however, that since the stiffness is measured during the unloading portion of the curve, the properties of the Ni were indeed being determined, as can be seen in Figure 4.17.

The displacement for a cantilever is predominantly dependent on the length of the cantilever and as well on other dimensions of the cantilever through the moment of inertia. By growing these films thicker, so that the cantilever lengths were longer, and while maintaining small cantilever cross-sectional area, the deflection of a cantilever

Table 4.3: Geometrical parameters of the microcantilever array tested.

Thin Film Sample	Length (μm)	Width (nm)	Thickness (nm)	Rise Angle (deg)	Young's Modulus (GPa)	Moment of Inertia (μm^4)	Experimental Spring Constant $(N/m)/(\mu m)^2$	Calculated Spring Constant $(N/m)/(\mu m)^2$
Ni Posts on Pressed Plastic	1.2 ± 5%	500 ± 5%	250 ± 5%	27 ± 5%	200	6.5e-4 ± 20%	83	72 ± 55%

could be made much higher than that which could be achieved with springs using the same applied force. With more easily detectable deflections, other methods of measuring these small displacements (optical or interferometric[64,65]) could be implemented and allow resonant frequencies to be determined. Estimated resonances for the microcantilevers and microsprings are in the MHz range, and can be conceivably adjusted to a wide range of frequencies by simple alteration of the microstructure parameters. It should be noted that by growing these films onto periodic arrays, they could not only be made more porous, but with a *known* porosity, thereby allowing for particular mechanical behaviors or responses to be achieved.

4.9 Finite Element Analysis

The finite element method was first introduced in the 1950's and has been continually developed and improved since then. It has become commonplace in recent years, allowing numerical solutions of extremely complicated problems. Finite element analysis (FEA) can enable the determination of stresses and displacements in structures of irregular shapes and cross-section. Although it is a complex technique, the fundamental principles are relatively straightforward, and usually consist of three basic steps in an analysis. A structure of interest is first modeled using simple geometries to create a representation of the structure's construction. FEA involves sub-dividing the geometries into a number of discrete pieces known as elements which are connected together at discrete points called nodes, each of which can be specified to have fixed displacements or prescribed loads, for example. Since the elements are very small, it is possible to accurately determine an element's behavior using a number of simple governing equations. These equations can be linear or nonlinear, depending on the type of problem, and are usually expressed in matrix form. Data from the elements are then put together to give system equations that describe the behavior of the complete structure; the sum of the variable to be determined that is contributed by each element must equal the effect of the variable on the entire structure. The solution can finally be visualized in a graphical display to help understand the results.

4.9.1 ANSYS® Study

Finite element modeling has been applied to nanoindentation measurements, often as a general tool to help with the understanding of the indentation process itself[66-69], but seldom to model the samples themselves. The column broadening effect was taken into account in initial simulations performed using ANSYS® finite element modeling software[70] with P. Ignatiuk. The microsprings were modeled using an initial column thickness that increased linearly to a final column thickness. Values for these thicknesses were obtained from cross-sectional SEM images of the films. The structures were fixed at the bottom face but free to move at the top face, and after applying the appropriate load to the top face, the compression results were based on an average top face motion. Preliminary results revealed that the deflection of a thickening microspring was fairly consistent with experimental deflections obtained for the thin film microsprings and that the maximum stress undergone by a microspring occurred towards the base at the initial turn. The calculated deflections deviated the most from the experimental values for microsprings with fewer turns, diverging by a factor of ~2 to 4 times.

An interesting outcome was obtained from a harmonic analysis of the modeled microsprings. While applying a sinusoidal force at varying frequencies to the modeled structure, the z- axis deflection was determined and plotted against frequency to reveal a spike (where the largest deflection was occurring) that indicated where the resonant frequency was estimated to be. The estimated resonances were in the MHz range, but on

Table 4.4: Comparison of measured deflections from nanoindentation experiments of microsprings with ANSYS modeled microsprings (at right).

Sample	Applied Load (uN)	Nanoindenter measured deflection (nm)	ANSYS determined deflection (nm)	Percent discrepancy (%)
1 turn	19	101	25	75
	47	152	41	73
2 turn	22	75	66	12
	51	123	94	24
3 turn	27	51	72	50
	60	85	97	14

the order of a few MHz compared to tens of MHz as calculated from Equation (4.5).

While the ANSYS software did provide some interesting first round results, to master the full capabilities of the software would have required significant time investments. As such, the results remained at the depth that was explored.

4.9.2 Recent ALGOR® Results

Recent work by Zhang and Zhao of the Nanoscale Science and Engineering Center at the University of Georgia involved the use of the FEA method to analyze nanosprings in greater detail[71]. The commercially available FEA software ALGOR®[72] was used to model the SiO microsprings used for the nanoindentation experiments mentioned earlier in Section 4.7 as well as some SiO square helices. Boundary conditions (BC) were found to have a significant effect on the spring stiffness. It was determined that Ancker's classic spring constant from Equation (4.1) assumed springs under radial symmetry, where both the top and bottom ends of the spring were under identical bounding conditions. The microsprings in the films were obviously not under this circumstance, being attached to the substrate on one end with free ends on top. Both conditions (springs under symmetric and non-symmetric BC's) were modeled and compared to the results calculated by Equation (4.1) and to the nanoindentation results that were obtained. What they discovered, was that Ancker's equation provided predictions in the same bulk range as their FEA results. The highest stiffness was determined from Ancker's equation, followed by the microsprings with symmetric BC's, and finally the microsprings with non-symmetric BC's that most resembled an actual film sample. The results of this final case (non-symmetric BC's) provided the closest agreement with the

Table 4.5: Comparison of microspring stiffness values (N/m) from Ancker's equation, symmetric and non-symmetric BC's and experimental nanoindentation results.

Microspring sample	Ancker's	Symmetric BC	Non-Symmetric BC	Nanoindentation Results
1 turn	2.61	2.15	1.15	1.00
2 turn	3.30	2.60	1.33	1.13
3 turn	4.28	3.27	1.78	1.78

nanoindentation results and indicated that their FEA simulations could be used to provide realistic results. Table 4.5 below shows how all of the methods compared with each other.

The effect of freeing the top end of a spring coil produced a reduction in stiffness of about 50% - 60% of the symmetrically bounded springs, and 60% - 70% less than Ancker's predictions.

With equivalent round and square helical microsprings of the same dimension, the square helices were stiffer than the round helices, being the stiffest at a specific rising angle. This result may prove useful information for work on periodic square helices by S. Kennedy in the area of photonic band gap materials. All things considered, Ancker's equation has been shown to be valid and applicable to predicting relationships between microspring stiffness and geometric dimensions.

4.10 References

[1] A. Lakhtakia, K. Robbie, and M. J. Brett, J. Acoust. Soc. Am. **101**, 2052 (1997).

[2] A. Lakhtakia, W. S. Weiglhofer, Microwave Opt. Technol. Lett. **6**, 804 (1993).

[3] E. H. Mansfield, The Bending and Stretching of Plates, 2nd ed., (Cambridge University Press, Cambridge, 1989), p. 123-125.

[4] H. J. De Los Santos, Introduction to Microelectromechanical (MEM) Microwave Systems, Boston: Artech House, 1999.

[5] T. Yi and C. J. Kim, Meas. Sci. Technol. **10**, 706 (1999).

[6] C. L. Britton, Jr., R. J. Warmack, S. F. Smith, P. I. Oden, R. L. Jones, T. Thundat, G. M. Brown, W. L. Bryan, J. C. DePriest, M. N. Ericson, M. S. Emery, M. R. Moore, G. W. Turner, A. L. Wintenberg, T. D. Threatt, Z. Hu, L. G. Clonts, J. M Rochelle, Proceedings of the 20th Anniversary Conference on Advanced Research in VLSI, 359 (1999).

[7] W. S. Trimmer, Micromechanics and MEMS: Classic and Seminal Papers to 1990, New Jersey: IEEE Press, 1996.

[8] C. M. Cheng and Y. T. Cheng, Phil. Mag. Lett. **77**, 39 (1998)..

[9] M. W. Seto, B. Dick, and M. J. Brett, J. Micromech. Microeng. **11**, 582 (2001).

[10] R. Roark, Roark's Formulas for Stress and Strain, 6th ed., New York: McGraw-Hill, 1989.

[11] A. M. Wahl, Journal of Applied Mechanics, **1**, A35, 1933.

[12] A. M. Wahl, Mechanical Springs, New York: McGraw-Hill, 2nd Ed., 1963.

[13] C. J. Ancker and J. N. Goodier, J. Appl. Mech., **25**, 466 (1958).

[14] C. J. Ancker and J. N. Goodier, J. Appl. Mech., **25**, 471 (1958).

[15] C. J. Ancker and J. N. Goodier, J. Appl. Mech., **25**, 484 (1958).

[16] D. Halliday, R. Resnik and J. Walker, Fundamentals of Physics, New York: John Wiley and Sons Inc., 4th Ed., 1993.

[17] T. G. Hicks, Mechanical Engineering Essentials Reference Guide, New York: McGraw-Hill, 1988.

[18] J. P. Den Hartog, Mechanical Vibrations, 3rd Ed., NewYork: McGraw-Hill, 1947.

[19] D. Pearson, Journal of Mechanical Engineering Science, **24**(4), 163 (1982).

[20] F. Kreith, The CRC Handbook of Mechanical Engineering, Boca Raton: CRC Press Inc., 1998.

[21] M. W. Seto, B. Dick, and M. J. Brett, J. Micromech. Microeng. **11**, 582 (2001).

[22] Triboscope®, Hysitron Inc., Minneapolis, MN.

[23] Dimension 3100 Scanning Probe Microscope, Digital Instruments/Veeco Metrology Group, Santa Barbara, CA, http://www.veeco.com.

[24] Y. T. Cheng and C. M. Cheng, Int. J. Solids Structures, **36**, 1231 (1999).

[25] C. M. Cheng and Y. T. Cheng, Appl. Phys. Lett., **71**, 2623 (1997).

[26] W. C. Oliver and G. M. Pharr, Journal of Materials Research, **7**(6), 1564 (1992).

[27] Hysitron Inc., Application Specific Tip Guide, http://www.hysitron.com/Products/Sellsheets/tip.htm, http://www.hysitron.com/PDF/0312-001%20Tip%20Guide.pdf.

[28] C. W. Shih, M. Yang and J. C. M. Li, Journal of Materials Research, **6**(12), 2623 (1996).

[29] W. N. Findley, J. S. Lai, and K. Onaran, Creep and Relaxation of Nonlinear Viscoelastic Materials, Amsterdam: North-Holland Publishing Co., 1976.

[30] I. R. Herman, Elastic and Inelastic Stress Analysis, New Jersey: Prentice Hall, 1992.

[31] B. Wilshire and R. W. Evans, Creep Behavior of Crystalline Solids, Swansea: Pineridge, 1985.

[32] A. S. Lodge, M. Renardy and J. A. Nohel, Viscoelasticity and Rheology, Florida: Academic Press, 1985.

[33] J. D. Ferry, Viscoelastic Properties of Polymers, 3rd Ed., New York: Wiley, 1980.

[34] G. Feng and A. H. W. Ngan, J. Mater. Res., **17**, 660 (2002).

[35] T. Chudoba and F. Richter, Surf. Coat. Technol., **148**, 191 (2001).

[36] T. Y. Tsui and G. M. Pharr, J. Mater. Res., **14**, 292 (1999).

[37] A. H. W. Ngan and B. Tang, J. Mater. Res., **17**, 2604 (2002).

[38] L. Cheng, L. E. Scriven and W. W. Gerberich, Fundamentals of Nanoindentation and Nanotribology Symposium, Materials Research Society, 193 (1998).

[39] K. B. Yoder, S. Ahuja, K. T. Dihn, D. A. Crowson, S. G. Corcoran, L. Cheng and W. W. Gerberich, Fundamentals of Nanoindentation and Nanotribology Symposium, Materials Research Society, 205 (1998).

[40] M. W. Seto, K. Robbie, D. Vick, and M. J. Brett, J. Vac. Sci. Technol. B, **17**(5), 2172 (1999).

[41] A. C. Fischer-Cripps, Nanoindentation, NewYork: Springer, 2002.

[42] Triboscope® Computer Software, Hysitron Inc., Minneapolis, MN.

[43] M. F. Doerner and W. D. Nix, Journal of Materials Research, **1**(4), 601 (1986).

[44] C. V. G. Vallabhan and Y. C. Das, Journal of Geotechnical Engineering, **117**, 956 (1991).

[45] W. F. Chen and A. D. M. Lewis Recent Advances in Engineering Mechanics and Their Impact on Civil Engineering Practice: Proceedings of the Fourth Engineering Mechanics Division Specialty Conference, New York: ASCE, 439, 1983.

[46] T. W. Lee, W. L. Cleghorn, and B. Tabarrok, Proceedings of the Thirteenth Biennial ASME Conference on Mechanical Vibration and Noise, Miami, FL, 1991.

[47] M. Hetenyi, Beams on Elastic Foundation: Theory with Application in the Fields of Civil and Mechanical Engineering, Ann Arbor: University of Michigan Press, 1974.

[48] J. R. Taylor, An Introduction to Error Analysis, California: University Science Books, 1982.

[49] S. G. Adams, F. M. Bertsch, K. A. Shaw and N. C. MacDonald, J. Microelectromech. Syst., **7**, 172 (1998).

[50] M. J. Brett, R. N. Tait, S. K. Dew, S. Kamasz, and A. H. Labun, J. Mat. Sci.: Materials in Electronics, **3**, 64 (1992).

[51] I. N. Sneddon, International Journal of Engineering Science, **3**, 47 (1965).

[52] G. M. Pharr, W. C. Oliver and F. R. Brotzen, Journal of Materials Research, **7**(3), 613 (1992).

[53] F. Liu, M. T. Umlor, L. Shen, J. Weston, W. Eads, J. A. Barnard, and G. J. Mankey, J. App. Physics, **85**, 5486 (1999).

[54] M. Malac, R. F. Egerton, M. J. Brett, and B. Dick, J. Vac. Sci. Technol. B, **17**, 2671 (1999).

[55] W. N. Findley, J. S. Lai, and K. Onaran, Creep and Relaxation of Nonlinear Viscoelastic Materials, Amsterdam: North-Holland Publishing Co., 1976.

[56] Z. Rymuza, M. Misiak, L. Kuhn, K. Schmidt-Szalowski, Z. Rzanek-Boroch, Microsystem Technologies, **5**, 181 (1999).

[57] INDICOAT final project report, NPL Report MATC (A), 24, 2001.

[58] H. Li and A. H. W. Ngan, Journal of Materials Research, **19**(2), In press (2004).

[59] M. P. de Boer, P. J. Clews, B. K. Smith and T. A. Michalske, Materials Research Society Symposium Proceedings, **518**, 131 (1998).

[60] Y. T. Cheng and C. M. Cheng, Philosophical Magazine A, **82**(10), 1821 (2002).

[61] J. R. Tuck, A. M. Korsunsky, S. J. Bull and R. I. Davidson, Surface and Coatings Technology, **137**(2-3), 217 (2001)

[62] B. Dick, J. C. Sit, M. J. Brett, I. M. N. Votte, and C. W. M. Bastiaansen, Nano Letters, **1**(2), 71 (2001).

[63] M. Malac, R. F. Egerton, M. J. Brett, and B. Dick, J. Vac. Sci. Technol. B, **17**, 2671 (1999).

[64] M. Stark, B. N. Bercu, F. Marchi, J. Chevrier and S. Huant, AIP Confernece Proceedings, **696**(1), 385 (2003).

[65] B. D. Jensen, M. P. de Boer and S. L. Miller, Second International Conference on Modeling and Simulation of Microsystems, San Juan, Puerto Rico, **2**, 1999.

[66] J. A. Knapp, D. M. Follstaedt, S. M. Myers, J. C. Barbour and T. A. Friedmann, Journal of Applied Physics, **85**(3), 1460 (1999).

[67] H. D. Espinosa, Y. Zhu, M. Fischer and J. Hutchinson, Experimental Mechanics, **43**(3), 1 (2003).

[68] A. Muliana, R. Steward, R. M. Haj-Ali and A. Saxena, Metallurgical and Materials Transactions A, **33A**, 1919 (2002).

[69] R. Schwaiger and O. Kraft, Journal of Materials Research, **19**(1), 315 (2004).

[70] ANSYS® Software, Full Version 5.6, ANSYS Inc., Canonsburg, PA, http://www.ansys. com.

[71] G. Zhang and Y. Zhou, Journal of Applied Physics, **95**(1), 267 (2004).

[72] ALGOR® FEA software, Pittsburgh, PA, http://www.algor.com.

CHAPTER 5
POTENTIAL FOR RESONATOR APPLICATION

5.1 Motivation

The structure of GLAD films suggests an application involving resonant spring microstructures[1,2,3]. A great deal of work and research is required before actual microspring resonators can be developed, however. Introductory studies and evaluations of methods that can be used to actuate and measure the deflections occurring in the films have been performed. The results have helped to determine some guidelines for the direction that future research should be focused on.

5.2 Estimated Resonant Frequencies

Estimated resonance frequencies for the microspring and microcantilever films are expected to be in the tens of MHz range. The modes of vibration (axial and shear) do have different resonant frequencies, but emphasis here is placed on axial vibrations since potential actuation mechanisms are more straightforward. Resonant frequencies are dependent on the spring constant, and hence become dependent on spring geometry and materials properties. Therefore, by customizing the material, geometry, and structure density of the films, it is conceivable to create resonators which could oscillate at various desired frequencies. With the use of additional circuitry, these frequencies could theoretically be dynamically controlled and varied.

The measurement of microspring frequencies remains a challenging task which lends no clear cut approach. Several complicating factors make measurements difficult, particularly the fact that the helical spring arrays are quite stiff. To produce successful results will require the enhancement of certain measuring techniques or the amendment of the geometry and material of the films being tested. Several approaches to determining the frequency of the GLAD-fabricated microstructures were tested and are discussed.

5.2.1 Axial Frequency Calculation

The standard frequency formula for the axial vibration of springs (as given earlier in chapter 4) is described by the following formula[4]:

$$f = \frac{1}{2\pi}\sqrt{\frac{k}{m + M/3}} \qquad (5.1)$$

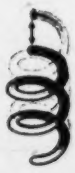

where f = resonant frequency, k = axial spring constant, m = attached mass and M = mass of the spring itself. The formula is applicable for the case where springs are fixed at one end and free to move at the other end (which is the case for the films being tested). A mass (m) can be attached to the free end and incorporated into the system, and in the case here, this attached mass would be the mass of the capping layer above the microsprings. Estimated resonant frequencies are calculated using the spring constant values that were determined in the previous chapter. Since errors from the estimated spring constants would be passed on, the error in the frequencies is expected to be large, but nonetheless provides reasonable ballpark figures in the tens of MHz range.

Microspring volumes were determined by visualizing the springs as unwound from their helix form into straightened out segments. Since columnar thickening was evident in the films, a better representation of the microspring volume was assessed by measuring the column diameters at various thicknesses in SEM images of the films. Thicknesses were determined to be approximately three times greater at the top of the films compared

Table 5.1: Calculations of estimated resonant frequencies for various microspring types.

Film Type	Estimated Axial Frequency (MHz) ± 85%	Microspring Volume (m^3) ± 15%	Microspring Mass (kg) ± 15%	Capping Layer Mass (kg) ± 15%
SiO - 1 turn	30	9.11E-24	1.91E-20	7.56E-17
SiO - 2 turn	33	1.08E-23	2.27E-20	7.56E-17
SiO - 3 turn	38	1.41E-23	2.96E-20	7.56E-17
Ti - 3 turn	27	1.95E-23	8.78E-20	1.13E-16
Cr - 3 turn	20	4.11E-23	2.96E-19	1.44E-15

to the initial diameters, with a relatively linear increase in columnar thickness assumed. The column broadening was previously ignored when determining the spring constants, since the application of a load to the microsprings produced the greatest stress at the initial region of the springs where the diameter was smallest, and hence deflection would have occurred there (making the use of a single column diameter reasonable). Since the frequency takes into consideration the mass of the microsprings, as close a representation of this value was incorporated in these calculations. Integration over the entire length of a helix produced the microspring volume that would be used to determine its mass.

$$V = \int_a^b \pi r^2 L dr = \frac{\pi d}{3}\left[b^3 - a^3\right] = \frac{\pi d 26}{3} a^3 \qquad (5.2)$$

where V is the volume of a microspring, r is the column radius (a = initial radius, b = final radius = 3a) and L is the length of the unwound helix and could be determined with $L = [(2\pi Rn)^2 + (h)^2]^{1/2}$, with R, n, and h as defined earlier. Masses of the microsprings were determined by multiplying their volume with the respective densities (2130 kg/m for SiO, 4500 kg/m for Ti, and 7190 kg/m for Cr)[5].

Volumes of the capping layer portions above the microsprings were determined by assuming a 400 nm thick cap. Using an area of one square micron, the volume was determined and divided by the microspring density (number of springs per unit area) to give the region above a single microstructure. This was multiplied by the appropriate material density to give the mass of the cap.

5.3 Testing Methods: Electrostatic Actuation

Several methods for testing the resonant frequency of the microspring films were conducted. They involved methods of actuating or exciting the film and observing the effect that this had on the film's response.

Initially, it was thought that through electrostatic actuation across electrodes sandwiching a helical spring bed, and by using interferometric detection of deflections off a reflecting top surface, the resonant frequency of the film could be observed when

the applied sinusoidal voltage signal matched that frequency. Measurements were made in collaboration with G. Steeves and M. R. Freeman from the Physics department of the University of Alberta, using a fibre interferometer with a 5V AC signal from a lock in amplifier applied across a microspring film up to a maximum frequency of 100 kHz. Use of the lock-in amplifier significantly improved the signal to noise ratio of the weak signals and allowed phase sensitive detection of the ac signals.

For ease of "squeezing" these films, the optimal geometry consists of microsprings with large coil radii and thin columnar diameters spaced apart from each other as far as possible. An optimal material like a plastic (e.g. parylene) was preferred, as it would yield more readily than other materials having higher values of Young's Modulus[6,7]. Initial depositions of plastics proved to be difficult materials to fabricate with the GLAD technique[8], and did not form the types of microstructures that could be easily obtained

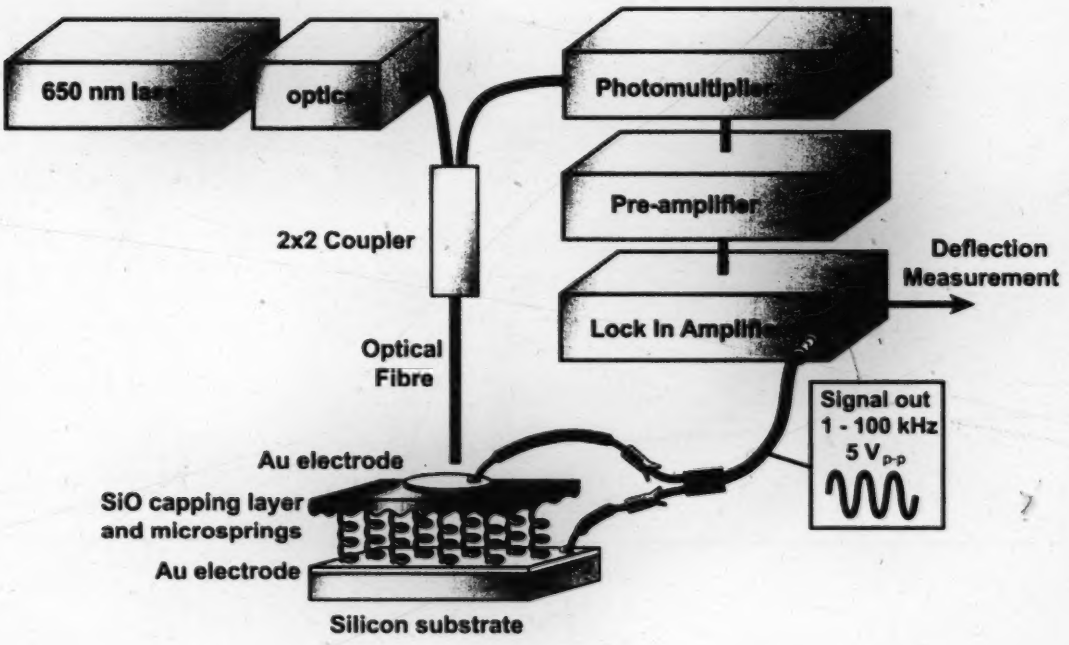

Figure 5.1: Interferometric detection of an electrostatically actuated microspring film.

using typical deposition materials. Therefore, standard materials were used to grow microsprings that were as close as possible to the optimal geometry.

5.3.1 Fabrication of Optimal Microspring Geometries

The fabrication of large coil radius microsprings produced a negative complication, however. Significant bifurcation of the columns took place during the depositions[9,10]. In order to increase the coil radius, the rate of substrate rotation was reduced over the entire course of the deposition. While keeping reasonable deposition rates (~ 15 Å/s) to prevent exceedingly lengthy deposition times, the thickness of the column diameters increased along with the coil radii. The effects of competition and extinction amongst the columns could be responsible, as shown in studies by D. Vick on the fundamental growth of columnar films that suggest growth of these films may obey a scaling law[11,12]. An increasing interface width of the tops of the films was confirmed by experiments with evaporated films on fixed and rotating substrates. Simulations from the ballistic simulator *3D-FILMS*, confirm that bifurcation can occur in these films, but further developments are required to better understand the nature and structure of growing films. Experimental evidence has shown that the column diameter, inclination, and bulk density

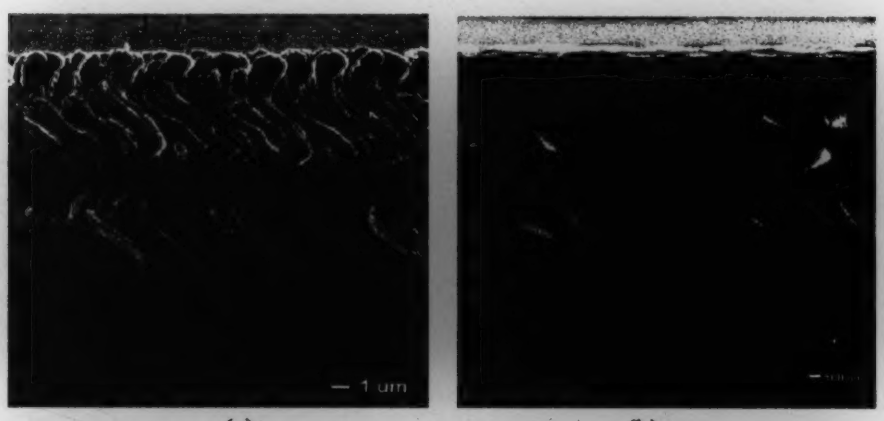

(a) (b)

Figure 5.2: A microspring film showing significant bifurcation in an attempt to increase the coil radius (a), and a film with smaller coil radius and less columnar broadening (b). Note the difference in scale bars between the two images.

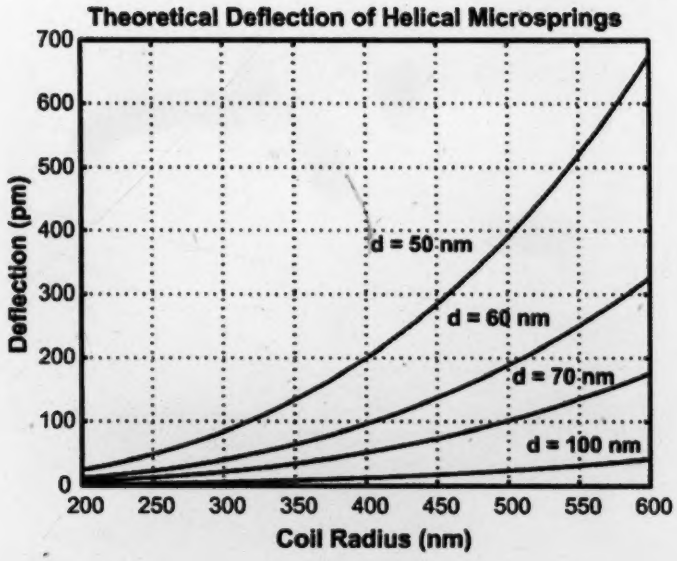

Figure 5.3: Theoretical deflection for a 2 μm thick, 2-turn helical microspring (κ = 4) with varying columnar thickness (d) and varying coil radius (R). The optimal geometry for maximum deflection consists of small d and large R.

of the film are affected by the choice of material, substrate rotation rate, and incident flux angle[13]. Therefore, although larger coil radii could be achieved, the drawback of larger column diameters negated the effect of any increased deflection that might have been achieved. Consequently, the films that were used for testing were comprised of those that were previously grown with reasonable columnar diameters.

5.3.2 Estimated Deflections

The metal electrode layers above and below the microspring film act like the plates of a capacitor and compress the film when a voltage is applied. The plates of a capacitor with dielectric material placed between would attract each other with force[14]:

$$F = \frac{\kappa \varepsilon_o A V^2}{h^2} \qquad (5.3)$$

where F is the force, κ is the dielectric constant, ε_o is the permittivity constant (8.85 e-12 F/m), A is the electrode area, V is the applied voltage, and h is the spacing between the

plates (in this case, h is the height of the film). Combining with Hooke's Law[15] and solving for the deflection gives:

$$\Delta x = \frac{\kappa \varepsilon_o A V_{max}^2}{h^2 ik} \tag{5.4}$$

where i is the number of springs being compressed and k is the spring constant from Equation 4.1.

It should be noted that the voltage cannot be increased arbitrarily to obtain greater deflections. There is a maximum voltage that can be applied to the microsprings, due to the porous nature of the film. Because air fills much of the space between the springs, the dielectric strength (maximum field intensity) will limit the amount of voltage that can be applied. Air has a dielectric strength[16] of 3×10^6 V/m, so given a two micron thick film for example, the maximum voltage that could be applied is nominally $V_{max} = E\ h = (3 \times 10^6 \text{V/m}) \times (2 \times 10^{-6}\ \text{m}) = 6$ V.

The metal electrodes were composed of Au, since it provided a smoother surface than Al. This was especially important for the bottom electrode layer, since any defects in this layer would be propagated to the microspring film. The top electrode layers were

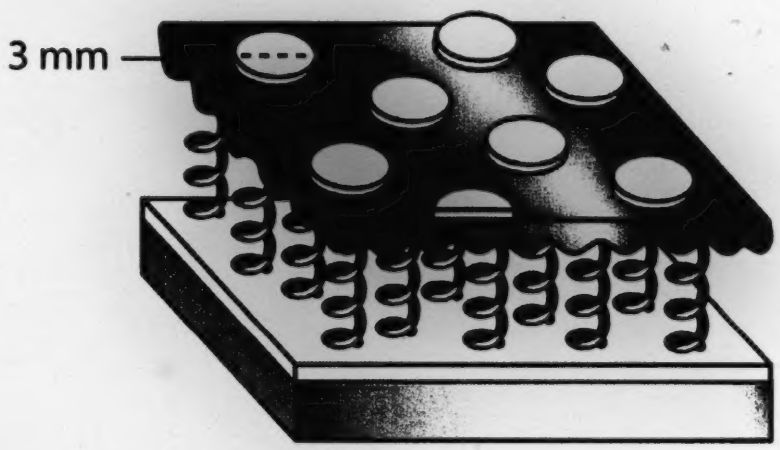

Figure 5.4: Top electrode pattern after masking the capping layer.

Table 5.2: Estimated microspring deflections for electrostatically induced deflection in microsprings with the geometrical parameters as those listed in Table 3.1.

Sample	Deflection (Å)	Maximum Voltage (V)
SiO - 1 turn	0.12	3.9
SiO - 2 turn	0.10	5.7
SiO - 3 turn	0.07	5.4

deposited using a shadow mask over the film which left 3 mm diameter 'patties' of metal over the capped film. The reason for having an array of small electrodes across the top of the film was to reduce the likelihood of any defects being present which could create a short between top and bottom electrodes. If a short was found, another electrode could be easily selected and used.

The estimated amount of deflection expected for electrostatic actuation of the films was quite low. The minimum spatial limitation of the interferometer (approximately 1×10^{-11} m) was discovered to be at the estimated displacement threshold capable for the spring geometries grown. While the growing of films onto patterned arrays could reduce the number of microstructures being compressed and make deflection detection more likely, the capping of such a film (in order for a top electrode to be deposited) remains a complex problem. If the patterned film were filled with another material to allow for a top electrode to be deposited, the task in removing *all* of the fill material would be a difficult undertaking, and would likely interfere with any actuation attempts. The ability to ensure complete removal of fill materials after the subsequent deposition of a capping or electrode layer may make this direction (whose purpose is to reduce the number of microstructures under compression) more feasible. Attempts are underway by A. Elias to fabricate polymer helices that should be approximately 50 times more compliant. This would allow detectable deflections over a range of sinusoidal frequencies to be observed, and if high enough frequencies were reached, resonance of the microsprings could be determined when deflections became the greatest[17].

5.4 Hysitron Acoustic Emission Testing

A newly developed technique and measuring system for *in-situ* Acoustic Emission (AE) monitoring[18-19] of fractures induced by nanoindentation was a method that was thought could provide some frequency information of the microspring films. This technique entails the monitoring of acoustic signals and events (such as high speed elastic and surface acoustic wave propagations) upon cracking capped microspring films with the indenter tip[22]. AE waveforms could then be captured and frequency domain analysis of the event plotted. Studies were made with A. Daugela of Hysitron Inc., but did not yield any comprehensible results, making further exploration into this technique necessary to help in the understanding of the required testing modifications and therefore how to interpret any resulting data.

Another option with the Hysitron nanoindenter would be to use its capability of applying high enough forces to deflect the microspring films. Oscillation of the tip at high frequencies on the film surface could provide a direct measurement of deflections and resonance if encountered. Current tip oscillation frequencies remain in the hundreds of Hz range, which is far too low for exciting the expected resonances of the microsprings. Modifications to the nanoindenter circuitry may make it possible for the tip to oscillate at higher frequencies, but would likely require improved piezoelectric elements and an extensive knowledge of the current circuitry before any changes could be made. As newer nanoindentation models are being developed, the increase to higher oscillation frequencies may continue and eventually reach the ranges that would enable testing of the microsprings.

5.5 Atomic Force Microscopy

A collaborative effort with D. Oliver from the University of Manitoba using an Atomic Force Microscope (AFM) to position an oscillating tip over the top of a single microstructure was performed to try to determine the resonant frequency of a single microspring. In this technique, the AFM tip did not touch the microsprings, but an RF sinusoidal voltage excitation was applied to the conductive tip to obtain an electrostatic

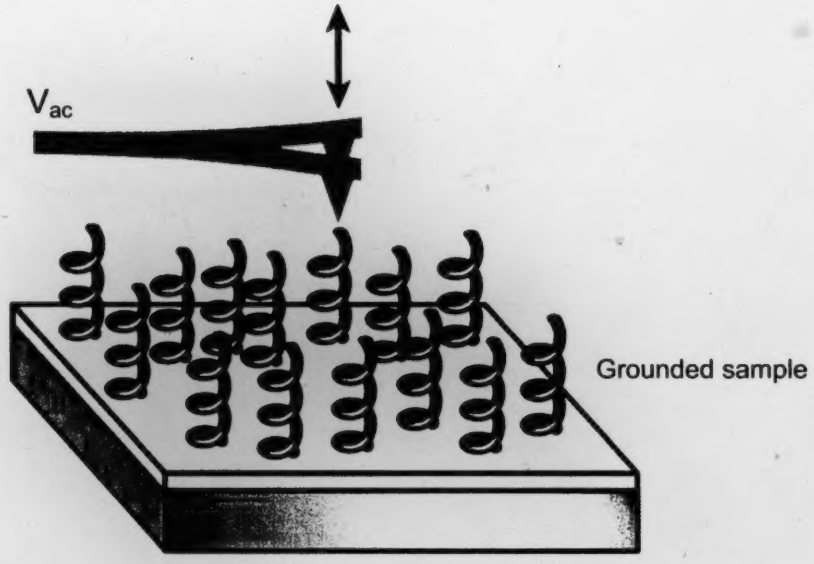

Figure 5.5: Schematic of AFM tip used to oscillate a single microspring.

response from the microspring while the amount of tip deflection was observed (via a laser beam reflected from the upper surface of the AFM cantilever to be detected by a split photodetector)[23]. The set-up of the apparatus was based on an established technique for electrostatic force probing of operating integrated circuits and devices where an electrical signal is applied to a noncontacting scanning probe microscope (SPM) cantilever and probe[24,25]. During each of the frequency sweeps, the tip location was chosen such that it was at a topographic maximum to ensure that the placement of the probe tip would be directly over what might be the top of a microspring. The frequency was swept across a broad range (10 MHz to 90 MHz) in 20 kHz steps with a dwell time of 50 ms to obtain an overall view of the microspring's frequency response. Subsequent scans were narrower in range, with a total bandwidth of 20 MHz centered at the frequency estimate over 0.5 kHz steps with the same dwell time. What was ultimately surmised after several trials was that the electrostatic coupling between the probe and sample was not strong enough for a response to be seen. From testing standard calibrated cantilevers, responses were easily observed, and it might have been due to the higher

stiffnesses of the GLAD microsprings (approximately an order of magnitude higher than standard AFM cantilevers) that made observations difficult. The solution here again would be to fabricate more compliant microsprings. One other possibility that might have made the observation of any resonances difficult could have been due to the high quality factor that a single microspring might have like many other high-frequency mechanical resonances. Thus the frequency scans might not have had to resolution to pick the resonance during the broad sweep ranges.

5.6 Laser Excitation with Piezoelectric Detection

A knife-edge technique done in collaboration with H. Minami utilized a KrF laser to induce SAW waves[26] in a microspring sample that was detected with a piezoelectric polyvinylidene fluoride (PVDF) foil positioned a small distance away (~8-10 mm). In 1969, H. Kawai[27] discovered that PVDF could be poled to a level of piezoelectric activity not previously obtained with any other polymeric materials. The piezoelectric film was flexible enough to be wrapped around a knife edge. As the surface acoustic wave (SAW) traveled through the film towards the PVDF foil after being triggered by the laser pulse, it was anticipated that the microsprings would be activated and would resonate.

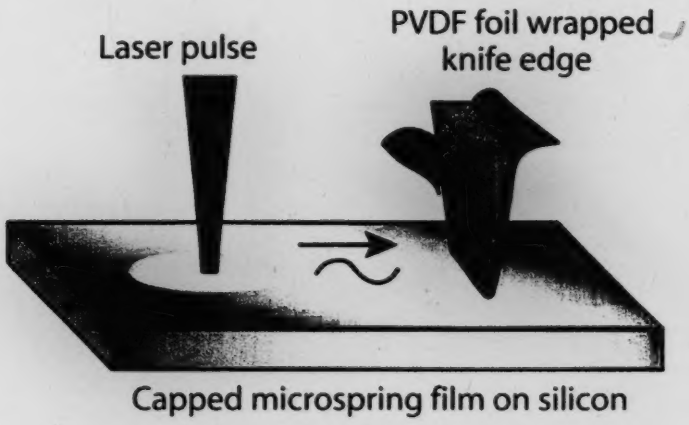

Figure 5.6: Schematic of the knife edge technique.

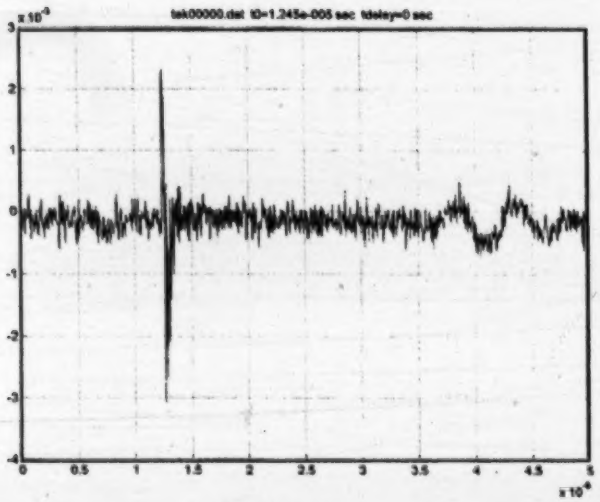

Figure 5.7: Recorded waveform from a PVDF film positioned approximately 8-10 mm away from the point of a laser pulse excitation. The large initial spike seen at the left indicates the moment the laser was triggered, and the smaller sinusoid seen at the right is the recorded sound wave.

A recorded voltage-time response was obtained and showed what might have been a microspring resonance. Testing a blank substrate revealed that the supposed resonance was actually due to the sound wave which traveled from the point of excitation to be detected by the PVDF film. The bottom time scale of Figure 5.7 is in seconds, and calculation of the velocity for the ~2.5 x 10^{-5} seconds (measured between initial trigger and beginning of the sinusoid) it took to travel the ~8 mm distance gives a value that is more or less the speed of sound in air[28].

It was possible that the coupling between the piezoelectric film and capping layer was poor, since the adjustment of the PVDF wrapped knife edge placement against the surface of the film was done by hand using a micrometer. The use of some type of substance like an oil to improve the mechanical boundary conditions might have allowed better coupling between the surfaces[29,30,31]. A similar experiment was subsequently conducted, using an interferometric detection method in place of the PVDF wrapped knife edge.

5.6.1 Laser Excitation with Interferometric Detection

Laser excitation and interferometric detection experiments done in collaboration with J. Gospodyn were evaluated and produced outcomes that remain open for interpretation. A set of experiments on a 4-turn SiO microspring film and a plain Si wafer revealed some clear differences between several recorded displacement-time waves after excitation with the laser.

The plots for the bare Si wafers seemed to contain more oscillations than those with the microspring films. It was possible that some internal reflection was occurring within the Si wafers due to the thinness of the substrates (~0.5 mm). The chance that the reduced oscillations were due to the damping effect of the springs is unclear and does not provide any conclusive evidence of any microspring resonances. Additional investigations with microspring films grown onto thicker substrates may prevent the internal reflections from occurring and provide more clues into why differences in displacement-time data occurred between substrate and substrate/film systems.

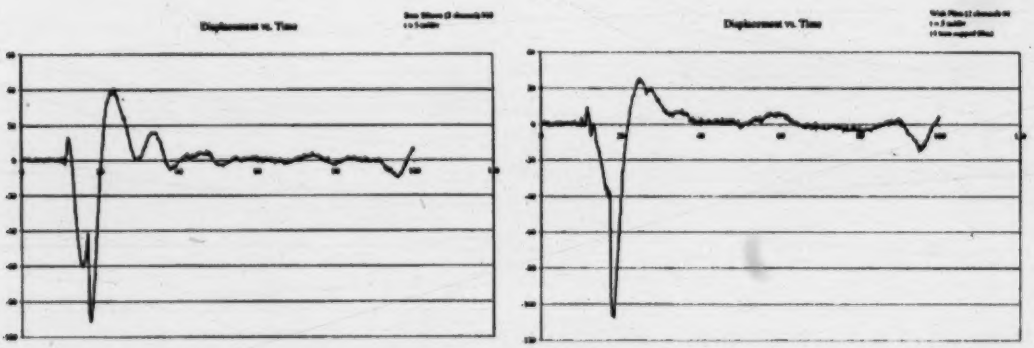

Figure 5.8: Displacement-time waves for plain Si in (a) and for a 4 turn microspring film on Si in (b) after laser excitation.

5.7 Network Analyzer Investigations with Lateral Oscillations

Lateral vibration frequencies of a spring can be determined from its lateral spring constant as given earlier[32,33].

Lateral spring constant: *Lateral resonant frequency:*

$$k_L = \frac{Gd^4}{128nR}\left[\frac{2}{2+\nu}\right] \qquad f_L = \frac{1}{2\pi}\sqrt{\frac{k_L}{I}} \qquad (5.3)$$

Lateral oscillations of a spring (in comparison with axial vibration) generally produce movement more easily than in the axial direction for most geometries, but depending on the dimensions and parameters of the spring, however, lateral spring constants can be made greater than axial stiffnesses too.

A crystal thickness monitor (CTM) device was used in efforts to create lateral oscillations. The mode of oscillation produced by CTM crystals is in the lateral direction and microspring films were grown onto these crystals to explore the detection of any lateral resonances. Use of a network analyzer from the Biomedical Engineering department with K. Wachowicz provided a means to explore the frequency response of the crystals over a range from 100 kHz to 1.2 GHz.

Two hard-baked photoresist layers (of thickness ~1.3 μm) coated on the CTM crystals were found to provide a smooth enough surface to deposit a GLAD film onto, since the Au electrode layer on the crystals was extremely uneven and rough in appearance when viewed with the SEM. Several microspring geometries were deposited with varying thicknesses and pitches. The results of testing these films demonstrated that there was indeed the expected frequency shift when comparing plain CTM crystals and those deposited with microsprings, due to the added mass of material. Peaks at the frequencies where resonances were expected were problematic to detect, since a low

Table 5.3: Estimated lateral spring constants and frequencies.

Microspring Sample	Lateral Spring Constant k_L (N m) x 10^{-13}	Lateral Frequency f_L (MHz)
SiO 1-turn	3.3	49
SiO 2-turn	2.4	52
SiO 3-turn	1.9	49

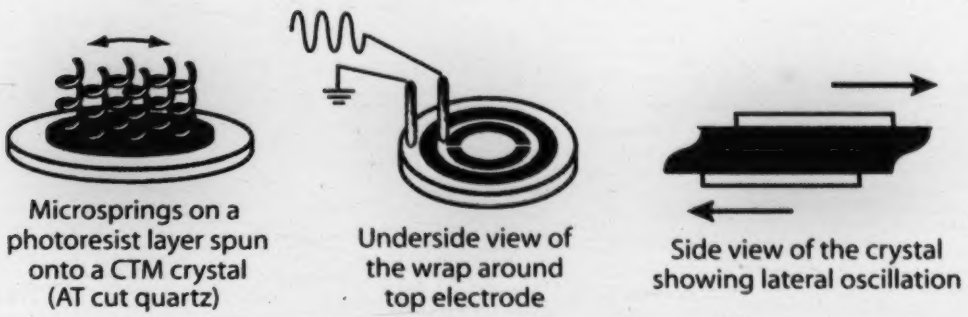
Microsprings on a photoresist layer spun onto a CTM crystal (AT cut quartz)
Underside view of the wrap around top electrode
Side view of the crystal showing lateral oscillation

Figure 5.9: Schematic of the microsprings grown on the CTM crystals and the lateral mode of oscillation they produced.

signal to noise ratio made it extremely difficult to distinguish any resonances from the background noise. Even the meticulous scanning of 1 MHz ranges from 100 kHz to 60 MHz with the subtraction of a saved background for each range did not succeed in the discovery of any distinct peaks that could be positively distinguished from the noisy signal.

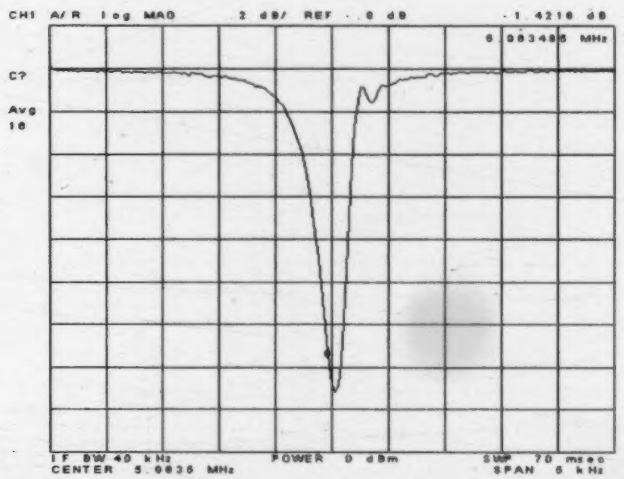

Figure 5.10: A network analyzer plot showing the absorption characteristics (ratio of reflected to transmitted power) of the CTM crystal over a frequency span of 5 kHz. A clear peak is shown at the resonance of the CTM crystal (~5.9 MHz).

It was possible that resonances may have been encountered, but were overlooked or missed due to the poor signal-to-noise ratio. One might also expect that the excitation of all the microsprings on the crystals could have produced a smaller, broad resonance peak due to the disparate geometries of the microspring shapes (each spring would not be exactly identical to the rest). The combined excitation of all the slightly varying springs could then produce a broader frequency response. Although wider frequency spans were also explored, the existence of any gradual crests could not be discerned. Improved predictions of where the expected resonances would occur might make it possible to scan particular regions with more attention and detail.

5.8 References

[1] S. Fujishima, IEEE 1979 Ultrasonics Symposium, 128 (1979).

[2] K. Wang and C. T. C. Nguyen, Journal of Microelectromechanical Systems, **8**(4), 534 (1999).

[3] H. J. de los Santos, Introduction to Microelectromechanical (MEM) Microwave Systems, Boston: Artech House, 1999.

[4] B. Morrill, Mechanical Vibrations, New York: Ronald Press, 1957.

[5] D.R. Linde (Editor), CRC Handbook of Chemistry and Physics, 77th Edition, CRC Press, 1996.

[6] J. Brandrup and E. H. Immergut, Polymer Handbook, 3rd Ed., New York: Wiley, 1989.

[7] N. P. Cheremisinoff, Handbook of Polymer Science and Technology, New York: M. Dekker, 1989.

[8] Ken Harris, personal communication.

[9] R. Messier, V. C. Venugopal, and P. D. Sunal, J. Vac. Sci. Technol. A, **18**, 1538 (2000).

[10] F. Lui, M. T. Umlor, L. Shen, J. Weston, W. Eads, J. A. Barnard, G. J. Mankey, J. *Appl. Phys.*, **85**, 5486 (1999).

[11] D. Vick, B. Dick, S. Kennedy, T. Smy and M. J. Brett, *Mat. Res. Soc. Symp. Proc.*, **648**, P3.43.1 (2000).

[12] D. Le Bellac, G. A. Niklasson, C. G. Granqvist, *Europhys. Lett.*, **32**, 155 (1995).

[13] F. Lui, M. T. Umlor, L. Shen, J. Weston, W. Eads, J. A. Barnard, G. J. Mankey, J. Appl. Phys., **85**, 5486 (1999).

[14] R. A. Serway, Physics for Scientists and Engineers with Modern Physics, 4th Ed., Philadelphia: Saunders College Pub., 1996.

[15] L. H. van Vlack, Elements of Materials Science and Engineering, Massachusetts: Addison-Wesley, 1985.

[16] D. Halliday, R. Resnick and J. Walker, Fundamentals of Physics, 4th Ed., New York: John Wiley and Sons Inc., 1993.

[17] L. Meirovitch, Elements of Vibration Analysis, 2nd ed., New York: McGraw-Hill,1986.

[18] A. Daugela and J. T. Wyrobek, Proc. Intermag 2000, Toronto, Ontario, April 7-13, P. HB04 (2000.)

[19] Daugela, A., J.T. Wyrobek, IEEE Transactions on Magnetics, 581 (2000).

[20] Daugela, A., H. Kutomi and T.J. Wyrobek, Zeitschrift fuer Metallkunde, September, 2001.

[21] Tymiak, N.I., A. Daugela, T.F. Page and W.W. Gerberich, MRS Fall 2000 Proceedings, Boston, MA, 2000.

[22] D. F. Bahr and W. W. Gerberich, J. Mater. Res., 13, 1065 (1998).

[23] D. R. Oliver, A. Pu, D. J. Thomson and G. E. Bridges, Applied Physics Letters, **79**(22), 3729 (2001).

[24] G. E. Bridges, R. A. Said, and D. J. Thomson, Electron. Lett. **29**, 1448 (1993).

[25] R. Said, M. Mittal, G.E. Bridges, and D. J. Thomson, J. Vac. Sci. Technol. A **12**, 2591 (1994).

[26] H. Minami, Y.Y. Tsui and R. Fedosejevs, Annual Congress of the Canadian Association of Physicists, Waterloo, June 14-17, 1998.

[27] H. Kawai, Japan J. Appl. Phys., **8**, 975 (1969).

[28] M. Hirschorn, IAC Noise Control Reference Handbook: Speed of Sound in Engineering Materials, New York: Industrial Acoustics Company, 1989.

[29] G. S. Kino, Acoustic Waves: Devices, Imaging and Analog Signal Processing, New York: Prentice-Hall, Inc, 1987.

[30] R. Kazys, A. Voleisis, R. Sliteris, L. Mazeika, R. Van Nieuwenhove, P. Kupshus and H. Ait Abderrahim, Proceedings of the World Congress on Ultrasonics, Paris, France, 2003.

[31] M. K. Jain, S. Schmidt, C. A. Grimes, Applied Acoustics, **62**, 1000 (2001).

[32] T. G. Hicks, Mechanical Engineering Essentials Reference Guide, New York: McGraw-Hill Book Co., 1988.

[33] J. P. den Hartog, Mechanical Vibrations, 4th Ed., New York: McGraw-Hill, 1956.

CHAPTER 6
Film Growth on Mesas: A Potential New Application

6.1 Introduction

To facilitate the nanoindentations of the microstructured films and to have better accuracy determining the area that was being compressed, GLAD-fabricated films were grown atop raised Si mesas and lines of known dimensions. A rather interesting effect that resulted from this endeavour were the formation of solid walls at the borders of the mesas and lines that enclosed a porous thin film centre of typical GLAD microstructures. These specialized structures were fabricated in a single step, forming both porous and walled regions without any further processing required. The unexpected solid wall growth stymied accurate nanoindentation measurements, but the unusual geometry of the structures is reported as device applications of these structures may be possible.

Advancements in miniaturized systems and lab-on-a-chip testing apparatus have rapidly progressed as the need for fast, inexpensive, and efficient testing methods and analytical tools has increased. In the past two decades, the biological and medical fields have seen great advances in the development of biosensors and biochips capable of performing various tasks.[1] Compared with traditional analytical instruments, chip-sized microsystems offer many advantages, from small dimensions, which give freedom from spatial limitations, to lower consumption of reagents and energy, which mean savings in cost and more efficient usage of resources.[2] The unique structures that have been developed here may offer applications in these areas.

6.2 Mesa and Line Fabrication

Silicon mesas and channels were fabricated using the Bosch Deep Silicon Reactive Ion Etch[3] process in an Oxford PlasmaLab 100 Inductively Coupled Plasma Reactive Ion Etcher (ICP RIE) system. The mesas and channels were masked during the deep Si etch

by a thermal oxide mask which was formed by placing 100 mm diameter silicon wafers into a furnace at 950 ℃. Injecting steam into the furnace during the oxidation formed an oxidizing environment that resulted in a 0.6 μm thick thermal oxide layer. The desired pattern of mesas and lines was then transferred to the oxidized silicon wafers by standard photolithography[4], after which a 10:1 buffered oxide etching (BOE) solution was used to remove the thermal oxide. The remaining photoresist was then removed after this wet etch step using an acetone wash. Finally, the wafer was placed in the ICP RIE, where the Bosch process was used to etch the structures to a depth of 14 μm.

Three different arrays of mesas having square faces measuring approximately 2.5×2.5 μm, 7×7 μm, and 25×25 μm were utilized for subsequent deposition of the microchamber wells (Figure 6.1 shows some of the bare mesas). The scalloped profile of the Si mesas is an artifact of the Bosch etch process.[3] A plan view of the mesas (with film) can be seen in Figure 6.3, and the Si lines, which varied in width ranging from 2.5 to 50 μm can be seen in Figure 6.2.

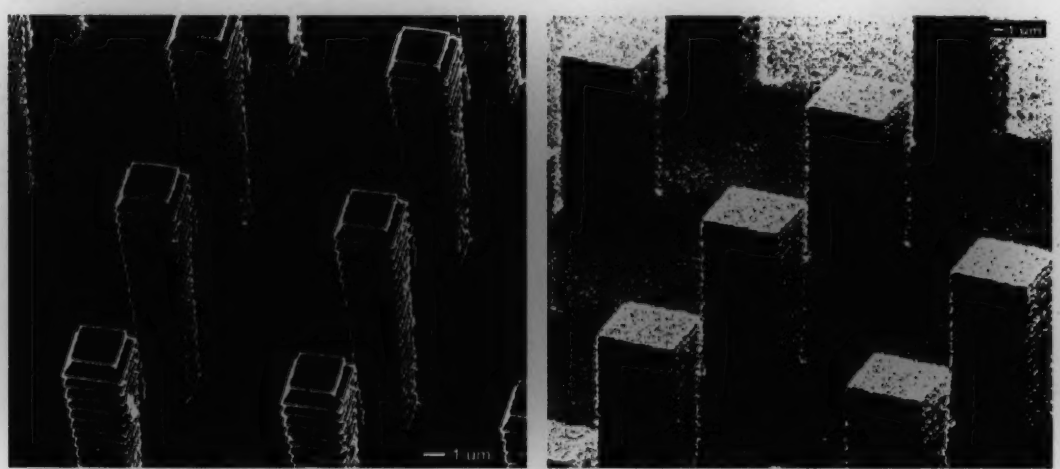

(a) (b)

Figure 6.1: Scanning Electron Microscope (SEM) images of bare silicon mesas (2.5 × 2.5 μm in (a) and 7 × 7 μm faces in (b)) upon which subsequent films were grown.

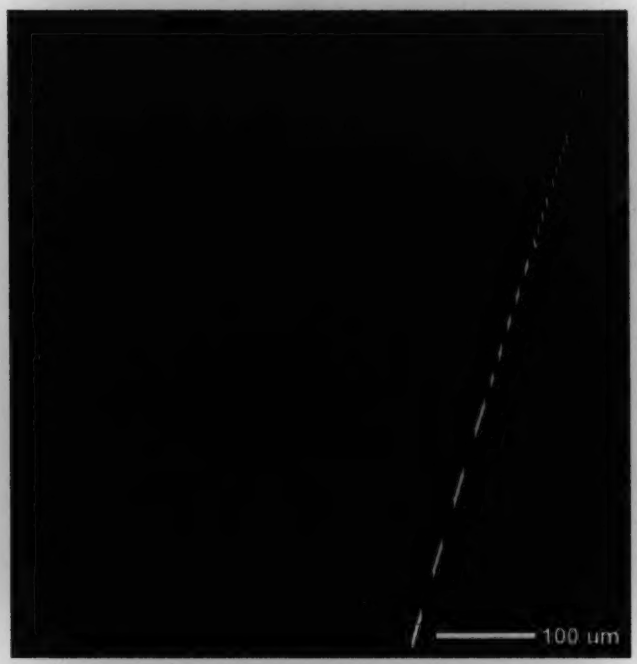

Figure 6.2: Various sizes of bare silicon lines on silicon which were later deposited on to form channels that contained unique structures having sealed side walls and top faces.

6.3 Experiment and Results for Slanted Post Film Growth

Two different thin film microstructure types were grown on the arrays of Si mesas. One included oblique angle depositions that resulted in porous, slanted post films contained by solid walls along two edges of each mesa. The other was a helical film deposition that produced porous helices within sealed walls on all four edges of the mesas. Both film types were fabricated with silicon monoxide as a representative material.

For the oblique angle depositions, the corners of the mesas were aligned diagonal to the direction of incoming flux, which arrived at an incidence angle of 85 degrees with respect to the substrate plane. A close up of one of the Si towers shows the solid border along two edges of the mesa (Figure 6.3(b)). Figures 6.3 and 6.4 clearly show the shadowed regions that formed between the mesas.

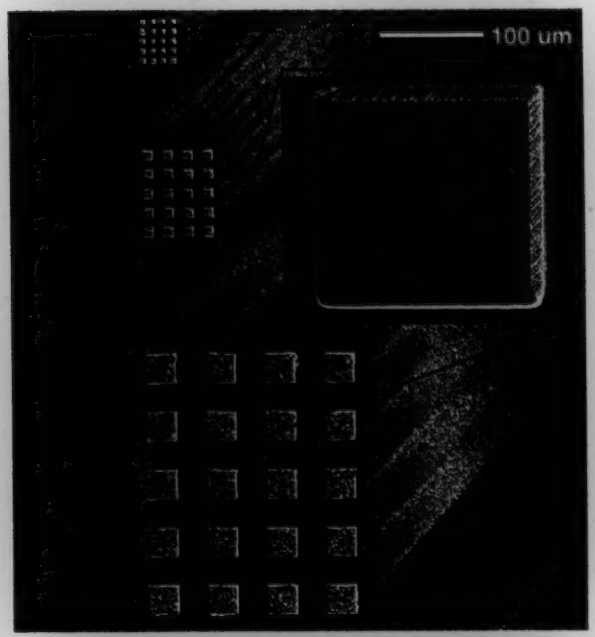

(a)

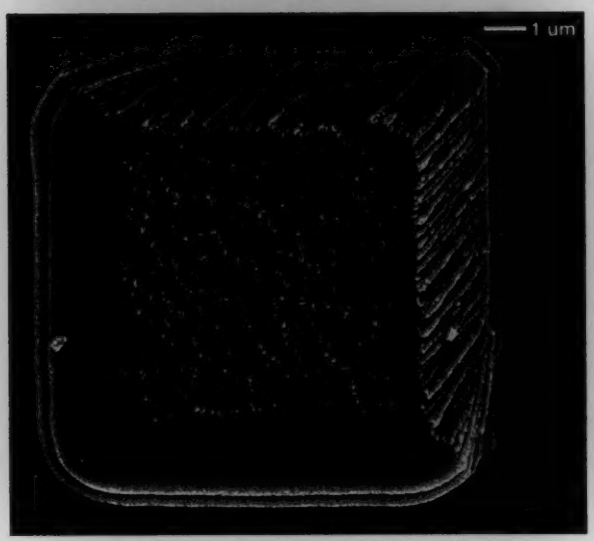

(b)

Figure 6.3: Plan view of three arrays of mesas with GLAD-fabricated porous thin film grown on top (a). The thin film microstructures resembled slanted posts, and were grown by an oblique angle deposition, with the arrow indicating the direction of the vapour flux. One of the largest sized mesas is shown inset. A close up view of the second largest sized mesas is shown in (b).

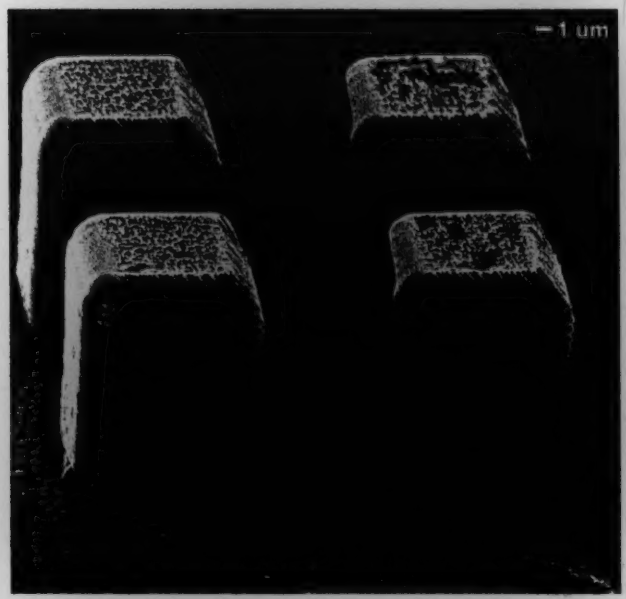

Figure 6.4: Distinct shadowing is evident between the silicon mesas. Dense regions of film growth along the vertical Si sidewalls occurred for those facing the direction of arriving flux, while the top faces contained a porous film.

Solid walls can also be observed extending completely from the base to the top of the silicon up to the thickness of the film before curling slightly onto the top surface to meet with the porous region of the film. This resulted from an edge effect where the apparent incidence angle with respect to the perceived substrate at the corner changed abruptly from a few degrees along the vertical sides to 85 degrees at the top face, thus causing the change from dense to porous film (Figure 6.5). Standard, dense films are typically grown at zero or very low incidence angles, such that the flux arrives nearly perpendicularly to the substrate. Therefore, whenever the flux approached a corner, the film would form a dense layer along the vertical side walls while forming a porous film on the top face, and where the two met, a self-sealed wall would form. Changes in film porosity have been demonstrated in capping layers[7] (discussed previously), where a porous film can be evolved into a dense layer that encapsulates the top surface of the film.

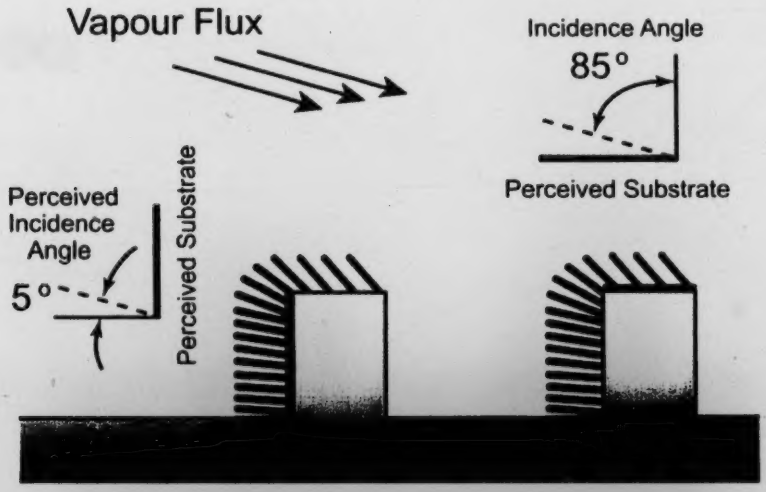

Figure 6.5: Schematic illustration of the perceived substrate and perceived incidence angles as seen by the vapour flux as it encountered the sides and top faces of the mesas.

6.4 Experiment and Results for Helical Film Growth

For the growth of helically structured films, the mesas were not aligned in any particular fashion with respect to the source, as rotation around the azimuthal direction disregarded any prior arrangement of the substrate. Some of the helical films are shown in Figures 6.6 and 6.7. As can be seen, a solid border completely encircles the porous regions for these films. Because the substrate was rotated completely around its axis to create helices with the desired number of turns, "walls" formed on all sides of the mesa, since flux arrived from all directions.

Average wall thicknesses were on the order of a few microns, and as a result, the smallest mesas did not produce a walled well structure containing a porous centre; the surface dimensions of the top face in comparison to the wall thickness were comparable, and therefore left no room for a porous region to form. The other mesas, however, were large enough to avoid this problem. Bifurcation of the structures that formed at the boundaries of the mesas (where the edge effect occurred) created these walls and hence

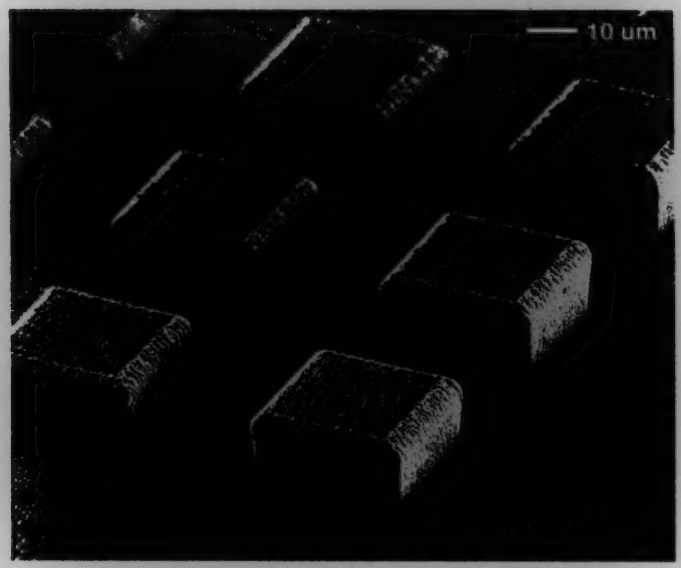

Figure 6.6: The helically microstructured film deposition resulted in solid perimeters encircling each mesa. Surface debris is believed to have caused the irregularities seen on a few of the mesas.

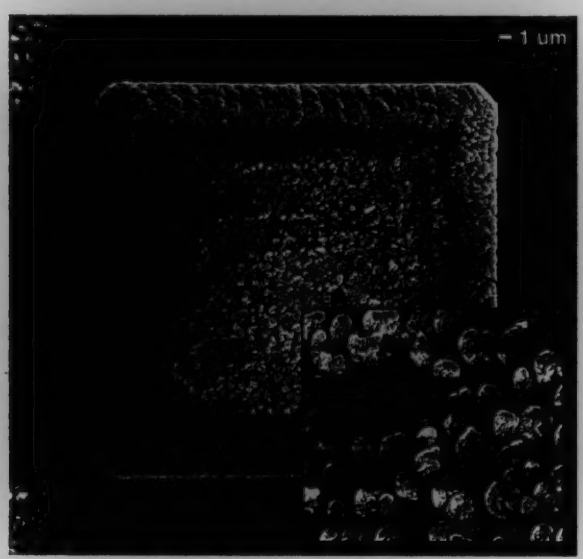

Figure 6.7: Plan view of a microchamber showing the porous centre (with close up shown inset) contained by a solid border.

reduced the area of the porous film region. Nevertheless, the vertical thickness of the film has an effect on the thickness of the surrounding borders, so it would be conceivable to grow thinner films on the smallest mesas while still enabling porous regions to develop in the centres. The inner pore and channel sizes therefore have a dependency on the film thickness, and on the amount of bifurcation of the walls.

6.4.1 Capping Layer Growth over Walled Structures

A capping layer deposition over the helical microstructures allowed dense encapsulation layers to be grown over the films. This produced structures that consisted of porous thin film centres enclosed by solid walls on all sides. Figure 6.8 shows some of the capped mesas, and Figure 6.9 shows a cross section of a Si line surmounted by a capped helical film. The latter figure reveals a microchannel with porous film encased by solid sidewalls and top capping layer that can be grown to any desired thickness to ensure complete encapsulation of the film underneath. Nanoindentation tests[16] have shown that the pressure required to fracture a 200-300 nm thick SiO capping layer is approximately 1.25×10^8 N/m^2 (~18000 psi) which is able to withstand the pressures (typically up to

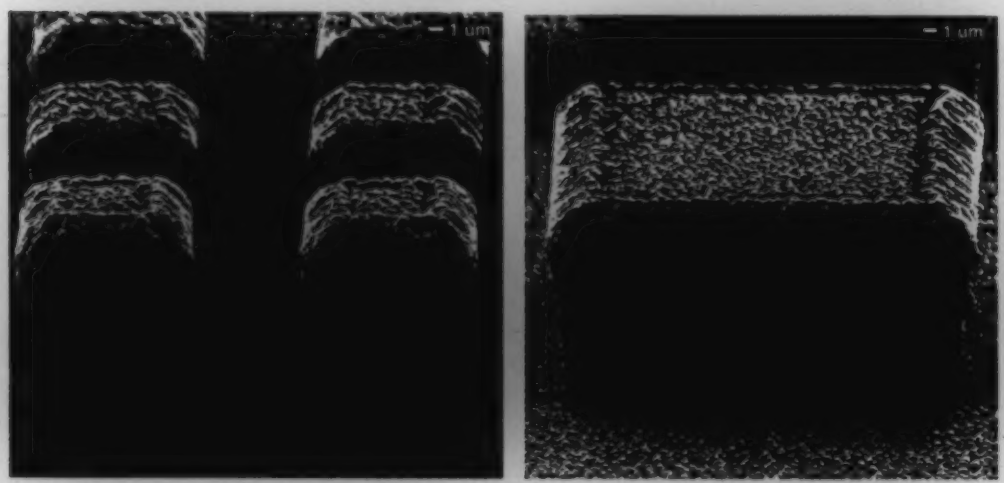

(a) (b)

Figure 6.8: Capped microchambers completely enclosed by encapsulation walls along all side and top faces.

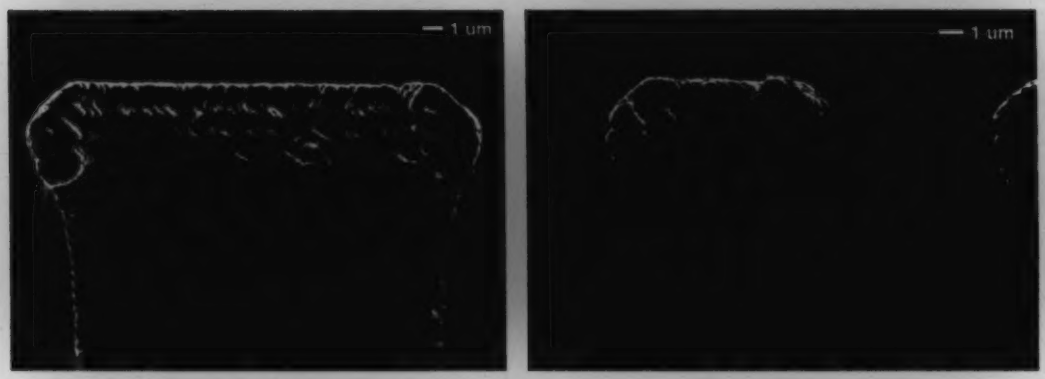

(a) (b)

Figure 6.9: Cross sectional images of capped helical films grown on silicon lines to form enclosed microchannels.

thousands of psi) found in some microfluidic systems[17] and high pressure chromatographic systems.[18]

6.5 Discussion of Applications

The porous thin film centre within the solid walls of the microchamber compartments can be seen more closely in Figure 6.8. The helical microstructures resemble a forest of "microsprings" whose geometry, thickness, and structure density can be modified during the deposition process. The unique nature of these highly porous films (~25% bulk density)[19] is attractive for several reasons. Their extremely high surface area (tens to hundreds of times the spatial area of the sample substrate[20]) may make them suitable for reactive or catalytic applications if fabricated with the appropriate materials. Small pore sizes between the columnar structures can result in strong capillary effects, which could have potential applications for various types of sensors.

A humidity sensor that was developed using these films possesses extremely rapid response times due to easy accessibility of the pores, which were anisotropic in nature.[21] The physical characteristics of these films suggest possibilities for filtering, chromatographic, electrophoretic, or sensing applications. Other potential uses of these

mesas may be in nano-assay applications where several arrays of these chambers could be employed, requiring only a miniscule amount of reagent. Individual chambers could be utilized to carry out separate reactions, or an array of chemical sensors could be formed. Each reaction chamber or cell could also be individually addressed,[22] scanned, and used with fluorescence detection systems if grown on transparent glass substrates.[23]

The ability to fabricate structures containing continuous walls sealing an interior of porous film could be applied to other shapes beyond the mesas and lines shown here. A raised pattern having edges where the vapour flux could encounter an abrupt change in substrate angle would result in the self-sealing edge effect. This attribute could be exploited with more complex shapes, such as T-junctions, so that a solid wall sealing a porous interior could be fabricated with almost any conceivable pattern.

Miniaturized reaction chambers are currently under development for lab-on-a-chip technology, which will bring the capabilities of larger and more expensive instruments to economical pocket-sized devices. The structures that have been fabricated here offer many possibilities that may lead to further developments in this field and many others.

6.6 References

[1] T. Vo-Dinh and B. Cullum, Fresnius Journal of Analytical Chemistry, **366**, 540 (2000).

[2] H. J. Lee, T. T. Goodrich and R. M. Corn, Analytical Chemistry, **73**, 5525 (2001).

[3] N. Maluf, An Introduction to Microelectromechanical Systems, Boston: Artech House, 2000.

[4] R. K. Watts, VSLI Technology, 2nd Ed., New York: McGraw-Hill, 1988.

[5] K. Robbie, M. J. Brett, Method of depositing shadow sculpted thin films, U. S. Patent Number 5866204, 1999.

[6] K. Robbie, L. J. Friedrich, S. K. Dew, T. Smy, M. J. Brett, Journal of Vacuum Science and Technology A, **13**, 1032 (1995).

[7] K. Robbie, M. J. Brett, Journal of Vacuum Science and Technology A, **15**, 1460 (1997).

[8] K. Robbie, M. J. Brett, A. Lakhtakia, Journal of Vacuum Science and Technology A, **13**, 2991 (1995).

[9] K. Robbie, C. Shafai, M. J. Brett, Journal of Materials Research, **14**, 3158 (1999).

[10] A. Lakhtakia, R. Messier, M. J. Brett, K. Robbie, Innovations in Materials Research, **1**, 165 (1996).

[11] D. Vick, Y. Y. Tsui, M. J. Brett, R. Fedosejevs, Thin Solid Films, **350**, 49 (1999).

[12] R. Messier, T. Gehrke, C. Frankel, V. C. Venugopal, W. Otano, A. Lahktakia, Journal of Vacuum Science and Technology A, **15**, 2148 (1997).

[13] S. R. Kennedy, M. J. Brett, O. Toader, S. John, Nano Letters, **2**, 59 (2002).

[14] J. C. Sit, D. Vick, K. Robbie, M. J. Brett, Journal of Materials Research, **14**, 1197 (1999).

[15] B. Dick, M. J. Brett, T. J. Smy, M. R. Freeman, M. Malac, R. F. Egerton, Journal of Vacuum Science and Technology A, **18**, 1838 (2000).

[16] M.W. Seto, K. Robbie, D. Vick, M. J. Brett, L. Kuhn, Journal of Vacuum Science and Technology B, **17**, 2172 (1999).

[17] B. A. Buchholz, E. A. S. Doherty, M. N. Albarghouthi, F. M. Bogdan, J. M. Zahn, A. E. Barron, Analytical Chemistry, **73**, 157 (2001).

[18] H. Ahren, The Scientist, **10**(5), 17 (1996).

[19] K. D. Harris, J. R. BcBride, K.E. Nietering, M. J. Brett, Sensors and Materials, **13**, 225 (2001).

[20] K. D. Harris, M. J. Brett, T. Smy, C. Backhouse, Journal of the Electrochemical Society, **147**, 2002 (2000).

[21] A. T. Wu, M. Seto, M. J. Brett, Sensors and Materials, **11**, 493 (1999).

[22] P. Swanson, R. Gelbart, E. Atlas, L. Yang, T. Grogan, W. F. Butler, D. E. Ackley, E. Sheldon, Sensors and Actuators, **64**, 22 (2000).

[23] R. J. Lipshutz, S. P. A. Fodor, T. R. Gingeras, D. J. Lockhart, Nature Genetics Supplement, **21**, 20 (1999).

CHAPTER 7
CONCLUSIONS AND SUGGESTIONS FOR FUTURE RESEARCH

7.1 Main Conclusions: Mechanical Response of GLAD films

The mechanical characterization of microspring and microcantilever thin films produced some fascinating and valuable results that will be of great use for further research in this area. Changes in the microstructures of GLAD-fabricated thin films greatly influenced the mechanical properties of the entire film. By varying either geometry, morphology, material, porosity or combinations of these parameters, the range of film stiffness could be readily modified to cover several orders of magnitude. Nanoindentation testing confirmed the differing degrees of compliancy in the films that were fabricated for testing these effects. Theoretical formulae for macroscopic structures were used to determine the stiffness of the respective film microstructures, and were shown to be applicable for use in the microscopic domain, giving correct predictions in trends for film stiffness.

7.1.1 Electrode Metallization Layer Development

It was also discovered that the type of electrode material used in the initial metallization layer prior to the growth of the GLAD microstructures was significant for the reduction of unwanted defects like nodular film growths. While most GLAD films already contain a number of these types of defects, they could be greatly reduced by the switch to a different electrode material. Defects in thin films strongly affect the ability to obtain accurate mechanical measurements, and cause electrical failures between electrode layers that could impede the ability to perform other measurements. A thin sputtered Au layer of ~50 nm was found to produce an improved, smoother surface that drastically reduced the occurrence of nodular defects when compared to films previously grown on evaporated or sputtered Al metallization layers.

7.1.2 Frequency Determination

Several experiments were performed to establish the groundwork for resonance frequency determination. These included interferometric detection of electrostatically actuated films, investigation of frequency data generated with acoustic emission testing, single microspring actuation using atomic force microscopy, laser induced surface acoustic waves in microspring films with piezoelectric and interferometric detection, and frequency studies of lateral resonances in films grown on piezoelectric crystals. The outcome of these experiments helped to identify the problematic issues and designs, improvements that could be made to sample fabrication and preparation, and limitations in both the testing methods and the films.

7.1.3 Key Areas for Improvement

Improvements to the thin film microstructures are crucial to producing films with more uniformity and more easily detectable deflections. These enhancements, which can be divided into three main areas, could then greatly improve the ability to determine the resonant frequencies of the films. The first issue involves the ability to fabricate structures having the desired geometries without complications like bifurcation and columnar broadening. A second matter deals with utilizing materials whose properties may make the deflection of the microstructures easier. The third area for improvement would involve the possibility of using pre-patterned substrates to further reduce the overall stiffness of the films. If accomplishment of these suggestions could be made, then the next step of producing actuating resonant structures with these films is closer.

7.2 Suggestions for Future Research: Materials Optimization

Since the key goal behind the finding of resonance frequencies is based on increasing the compliancy of the films, it is natural to consider fabricating these films with softer materials. Polymer films that could be grown with good microstructure control would be ideal, but extensive experimentation to determine the ideal deposition conditions and processing steps would be required. Pursuit of the fabrication of polymer helices has

become part of the research of A. Elias. The fabrication process involves a complicated double templating technique which entails the formation of a polystyrene perforated thin film to be vacuum filled with pentaacrylate (a monomer with good wetting characteristics). Removal of the polystyrene film should then leave behind a polymer film which would be greatly reduced in stiffness when compared to conventional GLAD microstructures. Although lower film stiffnesses would mean lower resonant frequencies, the reduction in frequency could make resonance detection easier, since standard pieces of laboratory equipment are usually limited to the low MHz range.

7.2.1 Microstructure Parameter Optimization

Improvements to the uniformity of the column diameter in the microstructure could involve the use of thin film simulators like *3D-FILMS*. Since temperature studies excluded the broadening as result of thermal increases at the substrate, the effects of various geometrical and deposition parameters could be integrated into the simulator to explore the possible influences that these factors could have in improving the modeled microstructure formations. These parameters could then be incorporated into actual depositions to see if improvements could be made to the thin film microstructures. By fabricating microstructures that more closely resemble the ideal shapes assumed in the macroscopic theory for springs and cantilevers, the use of these formulae could yield better estimates of resonances, and provide closer starting points when searching a range of frequencies.

7.2.2 Measurement Improvements of Parameters for Theoretical Predictions

As there would always be local variations in the microstructures and capping layers, the determination of more accurate masses (for use in the frequency equations) could further improve the estimates of resonant frequency locations. Although mass measurements of GLAD films have been attempted in the past, they have produced inconsistent results. An improvement to the measuring procedure could be developed, perhaps with the utilization of a measuring chamber where environmental effects like humidity could be controlled.

7.2.3 Porosity Enhancement with Patterened Substrates

Progress in the formation of the seed elements in pre-patterned substrates could make the fabrication of highly porous GLAD structures possible. By increasing the spacing between microstructures, the areal stiffness of the microstructures could be decreased, enabling easier deflection measurements. The ability to control the microstructure spacing (and hence stiffness), would also be extremely useful when designing films with specific frequencies in mind. Reductions in the size of the seed element could promote the growth of microstructures with lower stiffnesses as well, and the optimization of both seed spacing and size may be achieved by M. Jensen's work with creating periodic arrays.

7.2.4 Future Prognosis

The method described in Chapter 5 involving the use of a fibre interferometer to determine potential resonances would then be expected to yield a successful direct measurement of the resonance frequency, if a reduction in film stiffness could be achieved. The implementation of the above suggestions could reduce the film stiffness from those of the previously tested films, and allow the observation of deflections within the detection limits of the interferometric set up.

It is highly probable that these microspring films could function as mechanical resonators or actuators. Already, the discovery of humidity sensing with these films has been a benefit from this research and has initiated the development of a new sensing device. If implemented into frequency dependent devices, the characteristics of the microspring films could be easily modified by varying the microstructure parameters. Dynamic variation of frequencies could even be possible by using electrostatic actuation to modify microstructure geometries as needed, creating an exciting, new class of devices capable of performing over a range of frequencies.

When combined in various multilayer conceptions, the types of microstructure configurations that could be produced from the GLAD technique are virtually endless, as are the kind of mechanical responses that could be elicited from innovative, new structures.